Optical properties and carrier dynamics in anisotropic two-dimensional transition metal dichalcogenides ReS_2

Xiaofan Wang

Optical properties and carrier dynamics of quasi-particles in anisotropic transition metal dichalcogenides ReS_2

Xiaofan Wang

Graduate School of Energy Science

Kyoto University

2021

Abstract

Optical properties and carrier dynamics in anisotropic two-dimensional transition metal dichalcogenides ReS_2

By

Xiaofan Wang

Advisor: Professor Hideaki Ohgaki

Since graphene (a two-dimensional (2D) semiconducting material with an atomic layer structure) was discovered in 2004, a new field of semiconducting two-dimensional (2D) materials has emerged. From the perspectives of basic physics and applications, transition metal dichalcogenides MX_2 (M = Mo, W, X = S, Se and Te) with monolayer isotropic structure have been a hot study area. The significant change in electronic structures from an indirect bandgap above the bilayer to the direct bandgap when thinning down to the monolayer limit, which could extend the potential uses of transistors, photodetectors and light emitters in MX_2. Following the discovery of atomically thin black phosphorous (black phosphorene), atomically thin 2D materials with anisotropic crystal structures have been actively researched as a new 2D material research direction. Owing to the anisotropic electronic structures, such anisotropic atomically thin 2D materials would display the characteristic carrier transport and optical properties. In contrast to isotropic structure MX_2, ReS_2 is a layered material with a reduced symmetry because of the weak interlayer coupling from the distorted crystal structure, which provides a new platform for highly anisotropic optical physics in 2D materials Furthermore, compared to the well-studied anisotropic black phosphorene, the ReS_2 exhibits higher stability in the ambient state.

Strong Coulomb interaction in optically excited bound electron-hole pairs (neutral excitons) plays a major role in the optical response of low-dimensional materials like 1D carbon nanotubes and atomically thin 2D MX_2. The optical responses of carrier doped 1D carbon nanotubes and atomically thin 2D MX_2 are dominated by the three-particle bound states of charged excitons (trions). Extensive research has been conducted on the experimentally reported stable trions with significant binding energies in the atomically thin monolayer 2D transition metal dichalcogenides MX_2 with anisotropic crystal structure. However, the trions in atomically thin 2D materials with an anisotropic crystal structure are a new platform for many-body physics in the quasi-1D systems and in practical optoelectronic applications, is still poorly known, especially in ReS_2. Furthermore, the transient dynamics of photogenerated electron–hole pairs (excitons) and their whole relaxation processes have not been fully understood by comprehensive studies in the time scale range of subpicoseconds to subnanoseconds.

In this thesis, I investigated optical physics in new residents of transition metal dichalcogenides MX_2 materials, rhenium dichalcogenides (ReS_2) with distorted anisotropic crystal structures, providing new insights into atomically thin materials and an additional degree of freedom in optoelectronics applications. Transient photoluminescence and ultrafast pump-probe spectroscopy were used to study the ultrafast photogenerated carrier and exciton dynamics of three-layered ReS_2, monitoring the populations of electron-hole pairs and electrons/or holes in the excited states, respectively. By exploiting two different transient spectroscopies, I revealed ultrafast relaxation of direct and indirect exciton assisted by the one-phonon emission process in the indirect-bandgap ReS_2. Then, I have demonstrated experimental observations of the negatively charged exciton (negative trion) with large binding energy through comprehensive studies of photoluminescence spectra by tuning the carrier density. The exciton and trion dynamics are revealed in experimental results of photoluminescence spectroscopy and the phenomenological rate equation model. Moreover, I found that the radiative lifetime of the negative trion of ReS_2 increases linearly with increasing temperature, reaching a few nanoseconds at high temperatures. I believe that this observation could promote understanding of many-body physics in the optically excited states of such anisotropic atomically thin 2D (quasi-1D) systems and provide a bright future for the optical devices in a new element of atomically thin-layered ReS_2.

Acknowledgments

I want to thank the committee members of Ph. D thesis, Professor Dr. Hideaki Ohgaki and Professor Dr. Yuhei Miyauchi. I want to express my deepest gratitude to my advisor, Professor Dr. Kazunari Matsuda. I recall him accepting me as a student at the beginning of 2016 when I wanted to return to Japan. I could undertake doctoral research for over six years at Kyoto University, thanks to his kind advice and unwavering support. I did not know much about physics. However, he encouraged me to pursue the Ph. D program. Even when I made technical errors for optical measurements, he constantly assisted me and graciously informed me how to collect the experimental results when I had problems. I would not have been able to complete the study and research for the Ph. D course without his exceptional guidance.

I would also like to express my gratitude to Professor Dr. Keisuke Shinokita. He began teaching me how to use the pump-probe measurement in my second year. Most importantly, he gave me uncountable knowledge of physics, assisting me in completing my papers and daily life counsel. I could not accomplish everything well without his assistance. I also want to thank Professor Dr. Yuhei Miyauchi for his kindly guidance and for sharing my necessary physics ability. I also want to thank former and current group members: Dr. Wenjin Zhang taught me how to fabricate the device; Dr. Hong En Lim assisted me with the time-resolved photoluminescence measurement; Dr. Dezhi Tan, Dr. Sandhaya Koirala and Dr. Nur Baizura Mohamed provide the opportunities to share their precious experiences in research. Mr. Shohei Yanagawa, Mr. Yusuke Hasegawa, Mr. Takao Yamaoka, Ms. Saki Okudaira, Dr. Fengju Yang, Dr. Takashi Someya, Mr. Masafumi Shimasaki, Ms. Kengo Hachiya, Ms. Ken Kiyama, Mr. Kenya Tanaka, Mr.

Shotaro Yano, Ms. Zhang Yan have all been helpful. Thank all the interns, Dr. Amr Hessein Hassan, Mr. Alex Hwang, Mr. Sahil Patel and Mr. Kiran Kumar Krishna Murthy. I would like to thanks also to Ms. Shiori Fujiwara and Ms. Kaori Hashimoto, who kindly took care of all the administrative procedures. I want to thank Dr. Nguyen Thanh Cuong and Professor Dr. Susumu Okada from Tsukuba University, who provided us with the DFT calculation of the ReS_2 band structure.

Finally, I want to thank my family. I have been in Japan for almost ten years, but your support and love have never stopped. I appreciate everything you all give to me. Thank you.

Xiaofan Wang

王　暁凡

June 2021

Table of Contents

List of Figures

Chapter 1. Introduction

1.1. Background

Although nanotechnology has only been acknowledged as a field of natural sciences for about two decades, the discovery of nanomaterials has ushered in a new era in human history [1–3]. Nanomaterials, which have unique properties and can be used in medicine, engineering, catalysis and environmental remediation due to their small sizes exist both in human life and in nature [4]. The mechanical, electrical and magnetic properties of nanoparticles differ from those of bulk materials generated from the same chemical elements. These novel characteristics have been applied in various fields that are currently developing rapidly [5,6].

Nanoparticles are often much smaller than 100 nm in size, which necessitates the use of quantum mechanics rather than classical mechanics to characterize electronic states on this scale of materials [7,8]. Furthermore, the ratio of surface area to volume in materials is greatly increased. In comparison to bulk materials, their physical and chemical properties will be substantially altered. This “small size effect” has got much attention in science since the 21st century [9].

A single-carbon atomic sheet of graphene, discovered in 2004, is one of the most famous nanomaterials. Graphene is a new carbon material with various outstanding properties, including ultrathin, light, hard, soft, transparent, excellent electrical and thermal conductivity, excellent photoelectric performance and excellent surface adsorption performance [10,11]. Scientists perceive graphene as an ideal material, which might bring revolutionary changes in many research fields, such as optics [12], sensors [13] and bio-devices [14]. There have been about 10,000 studies published on graphene. This ultrathin nanomaterial of graphene can be easily obtained from graphite by mechanical exfoliation. Furthermore, as the next-generation material, graphene has demonstrated exceptional physical and optical properties [15].

Atomically thin two-dimensional (2D) layered materials have been thoroughly investigated during the past decade due to their intriguing physical properties and potential applications since intensive studies of graphene [16]. Transition metal dichalcogenides (TMDs) [17,18], black phosphorous (BP) [19] and hexagonal boron nitride (h-BN) [20] have all been reported in atomically thin materials. These atomically thin nanomaterials could be fabricated using mechanical exfoliation of bulk thinning down in atomically thin level [21] due to weak interlayer van der Waals (vdW) force. It can also be grown by chemical vapor deposition (CVD) [22]. Especially, MX_2 type materials (M = W, Mo, Ta, Ti, Nb, Re; X = Se, S, Te), belonging to the class of TMDs, have also attracted much attention because of superior electronic and optical properties [23,24].

TMDs are formed via laterally strong covalent bonds, providing great mechanical stability. Moreover, they can change the material properties from semiconducting to metallic and even superconducting depending on the combination of M and X [25,26]. They could be easily exfoliated and restacked as a new heterostructure by different kinds of monolayer materials due to the weak vdW interlayer force [15,27]. Therefore, 2D TMDs have emerged as a new material system.

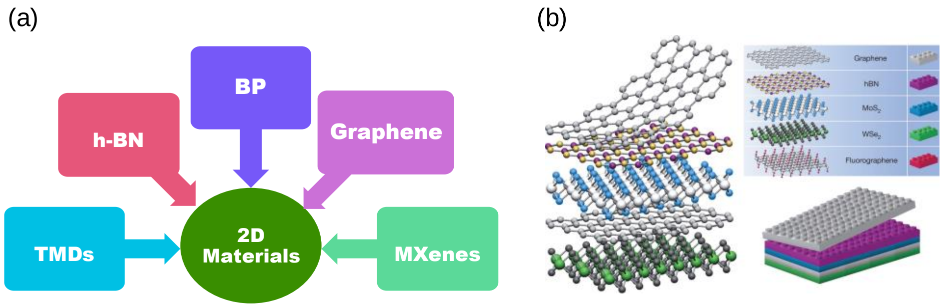

Figure 1.1 (a) Schematic of various 2D nanomaterials with their (b) atomic crystal and van der Waals heterostructures (Taken from Ref. [28]).

Compared with typical group IV TMDs materials (MX_2:M = Mo, W, X = S, Se, Te), group VII TMDs, such as rhenium dichalcogenides, ReX_2 (X = S, Se) [29] exhibit an anisotropic in-plane crystal structures. Such as new family of group IV TMDs with reduced crystal symmetries would give rise to intrinsically anisotropic electrical [30], thermal [31], mechanical [32] and optical responses [33]. Thus, the reduced symmetry in anisotropic group IV TMDs materials holds promises for developing novel devices with enhanced functionality, such as digital inverters [34], polarization-sensitive photodetectors [35], photodetector [36], and so on.

1.2. Motivation

Graphene-based applications in mechanics, chemistry and electronics have exploded with the development of atomic-level thin graphene. Various application prototypes have been introduced over the last decade [37–40]. Graphene has a large limitation in device applications because of the absence of an inherent bandgap. However, graphene has many outstanding physical properties, such as extremely high mobility or excellent flexibility. Its application in the development of new 2D electronics has been hindered [41,42].

Engineering semiconducting TMDs materials with adequate bandgaps, which may be used as an indispensable component of electronic devices, is another way to resolve the issue [43]. Semiconducting TMDs materials have opened up scalding research domains in the last decade [44]. Similar to graphene from graphite, the TMD is a layered material with weak out-of-plane interaction that can be mechanically exfoliated into multiple layers or monolayers [45,46]. TMDs have extraordinary optical features due to their unique electrical structure [47]. They are also a class of developing semiconductor materials with exceptional optoelectronic characteristics when thinned to a few layers [48].

TMDs materials with reduced symmetries, such as ReX_2, also feature anisotropic electronic structures and strong anisotropic (quasi-1D) optical characteristics [49], as discussed in the previous section. It also differs significantly from those seen in perfect 1D carbon nanotubes. This means that, compared to those using 1D materials (nanowire and carbon nanotube) with large inhomogeneities such as alignment, position and chirality [50,51], it not only fascinates from the perspective of fundamental physics, but also provides more opportunity and platform in controllable optical devices for next-generation applications.

1.3. Thesis outline

This thesis will introduce and discuss the new optical properties of anisotropic TMDs materials of ReS_2, including their carrier (excitonic) dynamics. The fundamental optical and electronic properties in semiconductor and 2D materials, especially for TMDs, will be introduced in Chapter 2. Chapter 3 will describe the experimental procedure for this research, with methods and optical setups. The transient and dynamical optical responses of a few-layered ReS_2, including the optically stimulated carrier and exciton relaxation process in the ultrafast time region, will be investigated in Chapter 4. In Chapter 5, using a phenomenological rate equation model, experimental observations of negative trion by tuning the carrier density and dynamics of optically excited trion in a few-layered ReS_2 will be discussed. In Chapter 6, more details of trion in ReS_2, such as binding energy and its polarization property, will be described. Finally, the thesis summary and outlook for the future will be described in last Chapter 7.

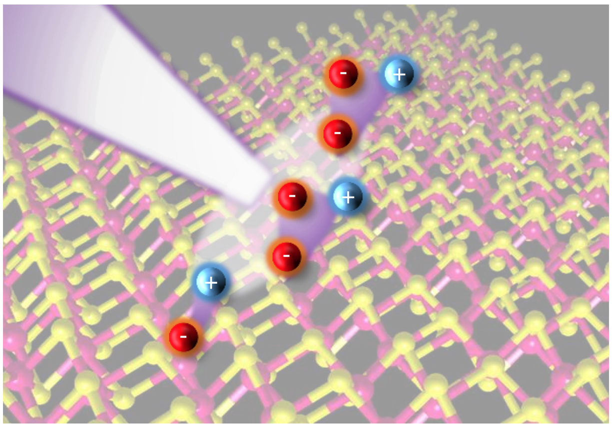

Figure 1.2 Thesis outline: Image of optically generated excitonic states in ReS_2.

Chapter 2. Introduction of electronic and optical properties of carrier 2D materials

This chapter will provide an overview of 2D atomically thin layer materials of TMDs materials, including their carrier (excitonic) dynamics, as well as fundamental physical understanding of optical properties on semiconductors. These can help us better understanding of the basic physics of this thesis.

2.1. Fundamental optical properties

To give a brief overview of 2D materials, fundamental knowledge of semiconductors and their optical properties will be introduced in this section.

2.1.1. Einstein coefficients

Following Pauli's exclusion principle [52], I will briefly discuss the fundamental optical transition of absorption and emission in the smallest atomic systems. All of the aforementioned transitions may be proved as three probability coefficients known as Einstein coefficients, as shown below:

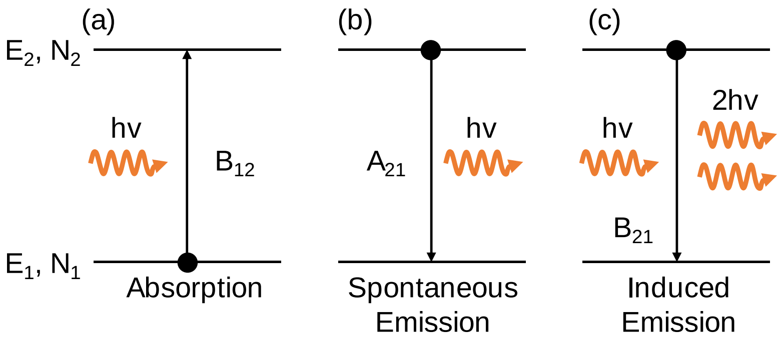

Figure 2.1 Schematic of optical transition process of (a) absorption, (b) spontaneous emission and (c) induced emission associated with Einstein coefficients.

Figure 2.1 shows three processes occurring in an atomic two-level system interacting with the light. The three processes are (a) absorption, (b) spontaneous emission and (c) induced emission of light. Each process can be regulated by Einstein coefficients, which measure their probabilities. In the absorption process, one photon is absorbed, and an electron in the grand state is excited to a higher excited state in the two-level system, where B_{12} is a coefficient of the absorption rate. In the spontaneous emission process, an electron in a higher excited state relaxes to the grand state, and spontaneously radiation of a photon occurs, where A_{21} is the coefficient of spontaneous emission rate. In the induced emission process, the incident photon induces the emission of light via the relaxation process of an electron to the ground state, where B_{21} is the coefficient of induced emission rate.

2.1.2. Fundamentals of semiconductor

A semiconductor is a material with electrical properties between conductors and insulators. Semiconducting materials' resistance decreases with increasing temperature, which is the opposite of metal's behavior (i.e., the resistance of metals increases with increasing temperature). The electrical properties of semiconducting materials can be easily controlled by introducing impurities (carrier doping) into the lattice structure and forming semiconductor junction structures based on modern and common electronic devices [53].

2.1.2.1. Electronic band structure

The fundamentals of electronic band structures in insulators, semiconductors and metals and their physical properties, will be described. Figure 2.2 demonstrates the electronic band structure on the insulator, semiconductor and conductor (metal). No energy gap between the occupied electronic band and the unoccupied band corresponding to half-filling of band exists, which causes the free conduction electrons in the metal. In a semiconductor, the finite energy gap, i.e., the bandgap, is opened between the highest energy of electron occupied band (conduction band) and the lowest unoccupied band (valence band). The electrons in the semiconductor (insulator) are strongly bound without gaining additional external energy by thermally and light, which causes a much lower conductivity than metal. If the higher energy is applied to the semiconductor across the band energy, bound electrons at the valence band are excited to the unoccupied conduction band. Then, free conduction electrons are generated in the semiconductor (insulator). The semiconductor and insulator are generally classified by the bandgap range, germanium (Ge) with a small bandgap at 0.67 eV and diamond with large energy at 5.47 eV, respectively [54].

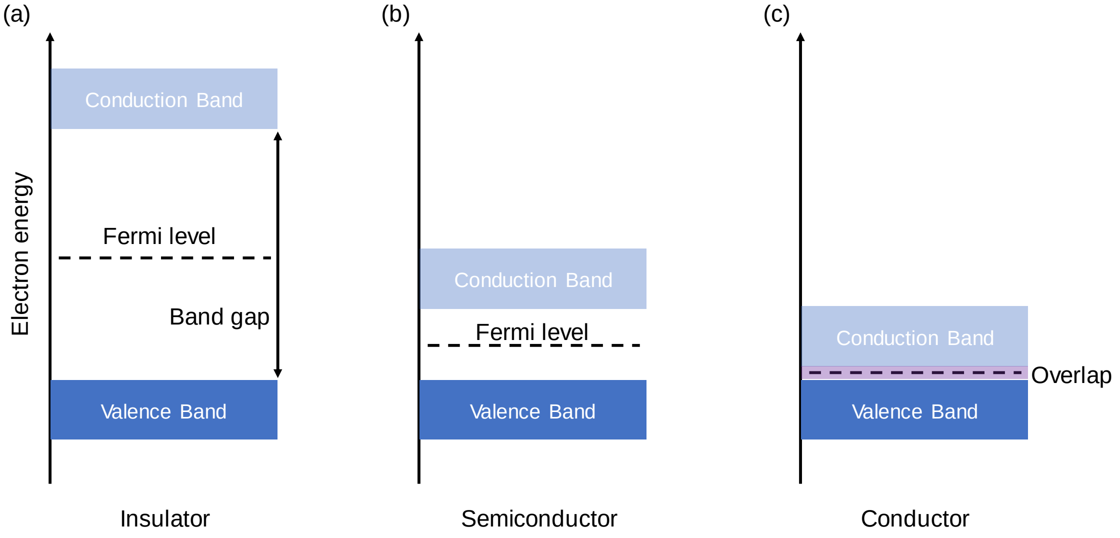

Figure 2.2 Band diagram in material for insulator, semiconductor and metal.

2.1.2.2. Carrier doping for semiconductor

The electrical conductivity of semiconductors could be controlled through the density of free carriers (electrons or holes) by substituting atoms with different valences, which is also the essential reason to be employed in electronic and optical devices. Figure 2.3 shows a schematic of the electronic band structure in the most typical semiconductor of Si with and without doping. The substitution of Si atoms into phosphorus (P) or arsenic (As) induces the impurity energy level of the donor located close to the conduction band. Then, free electrons are excited to the conduction band, which enhances electrical conductivity for *n*-type semiconductors. In contrast, the substitution of Si atoms into trivalent boron (B) also induced the acceptor level located close to the valence band. Consequently, free holes are excited to valence band for p-type semiconductors [55].

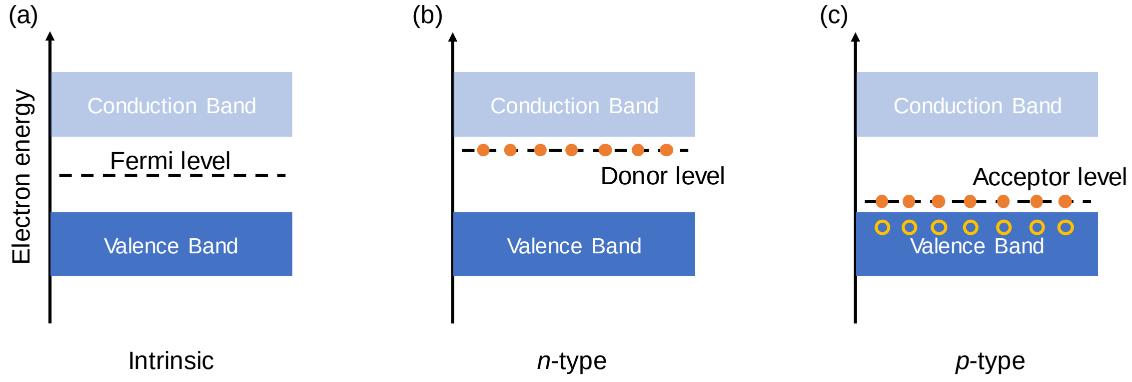

Figure 2.3 Energy bands in intrinsic, *n*-type and *p*-type semiconductors.

2.1.3. Quasi-particles

Quasi-particle is an essential concept in optical physics in the semiconductor (insulator). A quasi-particle is an excitation of a multi-particle system with a relationship between energy and momentum (dispersion relation), and is usually the collective state of many particles. As the name indicates, a quasi-particle is not a particle but a physical phenomenon (like collective matter excitation), which has at least some particle properties. For instance, in a semiconductor the negatively charged valence electrons collectively move in one direction as if a positively charged particle was moving in the opposite direction. Well-known examples are phonons, magnons, cooper pairs, exciton and trion. I will introduce these two kinds of quasi-particles, exciton and trion in semiconductors because the optical properties of low-dimensional semiconducting materials are dominated by exciton and trion.

2.1.3.1. Exciton

Excitons are bound electron-hole pairs generated by optical excitation in semiconducting materials. The electrons in the valence band are excited to the conduction band under the excitation of light. Simultaneously, residual electrons (hole) are generated at the valence band. Then, an electron with a negative charge and holes with an appositive charge are bound together by the Coulomb force to form bound electron-hole pairs as an exciton. These excitons as bound electron-hole pairs are similar to hydrogen atoms, so the exciton energy structures are similar to those of the hydrogen atom, which the hydrogen-like Rydberg model can describe. Note that the Coulomb force in the exciton is weakened by dielectric screening compared with that of the hydrogen atom in the vacuum. The optical transition of excitons will be discussed in the next section.

Wannier-Mott excitons, charge-transfer excitons and Frenkel excitons are the most common types of excitons (Figure 2.4). The Coulomb interactions between electrons and holes are weak, resulting in a weakly bound state known as a Wannier-mott exciton, which is found mostly in semiconductors. The Frenkel exciton in the insulator, on the other hand, is a highly bonded state of electron-hole pair with a binding radius comparable to the crystal cell range. The charge-transfer exciton is observed in the organic semiconductor between these two excitons [56].

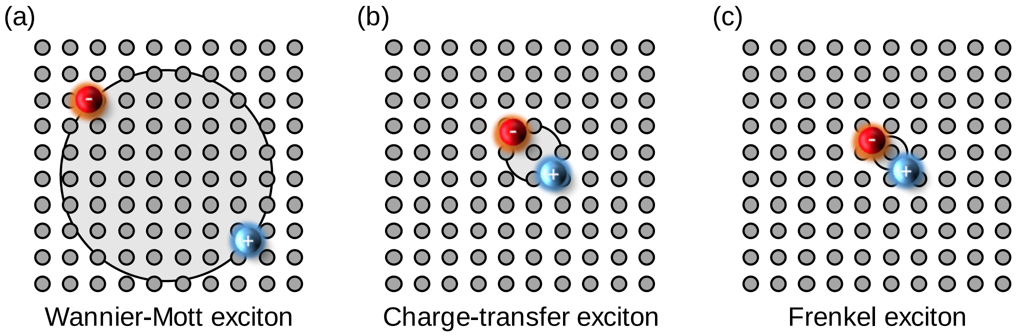

Figure 2.4 Schematic of Wannier-Mott, Charge-transfer and Frenkel exciton in the solid.

2.1.3.2. Trion (Charged exciton)

In the doped semiconductors, the optically generated excitons (bound electron-hole pair) will interact and eventually bind with the surrounding free charges. The Coulomb bound states consist of two electrons and one hole, as negatively charged exciton (negative trion). Alternatively, two holes and one electron, as positively charged exciton (positive trion), are schematically shown in Figure 2.5. Trion states have been theoretically predicted and observed experimentally in low-dimensional semiconductors, such as carbon nanotubes or 2D nanomaterials [57].

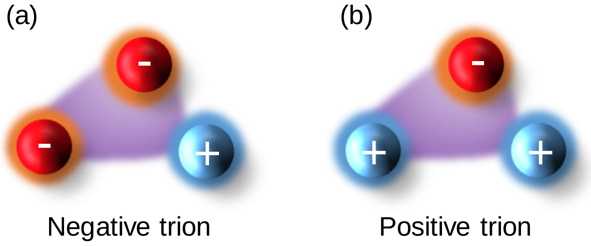

Figure 2.5 Schematic of positive and negative trion (charged exciton).

2.1.4. Carrier dynamics

In this section, I will introduce the fundamental optical processes of light absorption and luminescence in semiconductors. Additionally, the dynamics of optically generated electron-hole pairs (excitons) will be explained.

2.1.4.1. Optical transition

The optical transition by light absorption is a basic physical phenomenon in the materials. Energy-momentum (*E*-*k*) relationship obtained by solving Schrödinger equation is always used in describing semiconductor band structure as follows:

$$\left[-\frac{\hbar^2}{2m^*}\nabla^2 + V(r)\right]\Psi_{\mathrm{k}}(r) = E\Psi_{\mathrm{k}}(r) \ , \tag{2.1}$$

If the electrons move freely without a potential barrier ($V(\boldsymbol{r}) = 0$), the electron wave function is described as plane-wave. Thus, Eq.2.1 will become:

$$-\frac{\hbar^2 k^2}{2m}\Psi_{\mathrm{k}}(r) + E\Psi_{\mathrm{k}}(r) = 0 \ , \tag{2.2}$$

$$E = \frac{\hbar^2 k^2}{2m} \ , \tag{2.3}$$

where $\boldsymbol{r}$ is known as the eigenvector and E is the eigenvalue. The momentum of this wave is described as $\boldsymbol{p} = \hbar\boldsymbol{k}$, where $\boldsymbol{k}$ represents the electron momentum with a factor of $\hbar$ and the electron energy has a parabolic dispersion with respect to $\boldsymbol{k}$ [58].

Here, I want to give an actual example of the typical electronic band structure of semiconductors. Figure 2.6 displays Si and Ge band structure. In Figure 2.6, the horizontal axis is the electron wave vector k and the vertical axis is energy E. The Γ point is Brillouin zone center and X/L points correspond to zone edges. Γ→X and Γ→L are two dispersions of bands. The bandgap (E_g) of Si or Ge is indirect due to the minimum of the conduction band (CB) located near L or X point but not Γ point of the Brillouin zone [56].

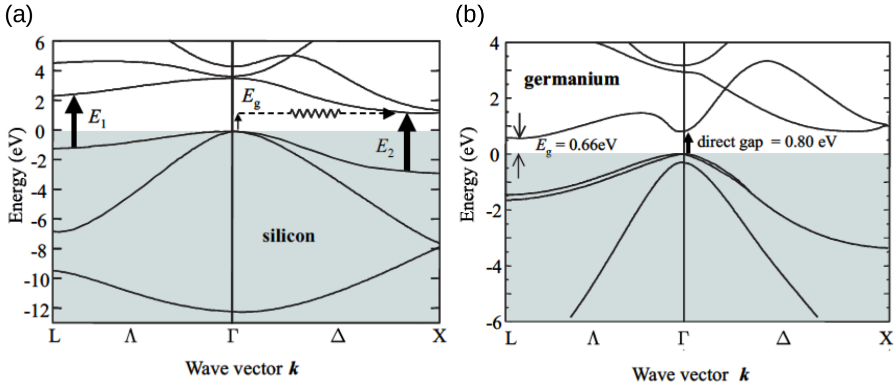

Figure 2.6 Band structure of (a) Si and (b) Ge (Taken from Ref. [56]).

Figure 2.7 depicts a simplified schematic of optical absorption to understand the optical transition. The CB is shown on the upper parabolic band, while the valence band (VB) is shown on the lower parabolic band (VB). The minimum difference of separated energy defines the bandgap (E_g). Here I consider the situation where the semiconductor is excited by light. The incident light has larger photon energy than band energy ($h\nu \geq E_g$), causing light absorption in the semiconductor. Under light excitation the electrons are transferred from the valence to the CB, increasing conductivity in the semiconductor due to the generation of free electrons. The generation of a residual hole with a positive charge in the VB occurs in this optical absorption process, and the formation of bound electron-hole pairs in the same momentum space generates the excitonic bound state as an exciton, as described in the previous section.

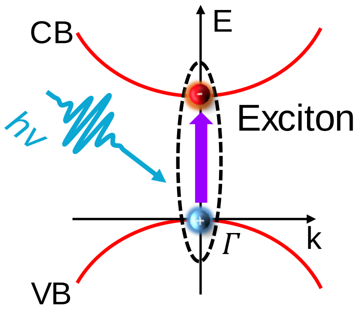

Figure 2.7 Schematic of optical absorption in the semiconductor and exciton (a bound electron-hole pair) generated by the incident light.

Many-state transitions happen if the electron and hole have the same velocities, which means the CB and VB at the same space of Brillouin zone. The single-particle transition energy from the initial to a final state, corresponding to the fundamental band energy, is higher than the exciton transition energy. This energy difference between the free-electron-hole pair states corresponding to bandgap energy, and exciton states corresponds to exciton binding energy. Electrons and holes have the same moving speed in the crystal due to their Coulomb interaction [56].

The semiconductor can be divided from the optical transitions into direct and indirect bandgap. The direct band transition will be realized as the conduction band minimum (CBM), and the valence band maximum (VBM) is located at the same momentum in the Brillouin zone center ($\boldsymbol{k}$ = 0), which is shown in Figure 2.8(a). In contrast, VBM and CBM are in different momentum spaces, and they will be realized as indirect-bandgap semiconductors, as shown in Figure 2.8(b). The optical transition occurs across the indirect-bandgap transition accompanied using a phonon-assisted process [56].

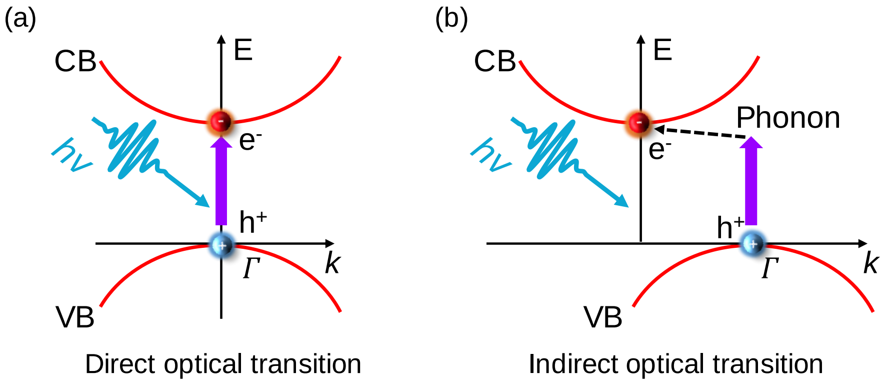

Figure 2.8 (a) Direct and (b) indirect-bandgap optical transition.

2.1.4.2. Luminescence

Photoluminescence (PL) is a frequently observed optical phenomenon in semiconductors and other materials with electronic gaps. As shown in Figure 2.9, after excitation an electron at the CB, the higher energy photoexcited electrons relax and spontaneously recombine with holes. It is possible to measure a material's optical properties by analyzing the PL spectrum because it provides insightful information about the semiconducting material: bandgap, light emission efficiency, quality of the material. Then, PL spectroscopy is one of the important probes to study semiconductors [56].

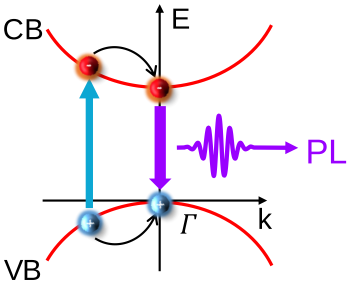

Figure 2.9 Schematic of photoluminescence (PL) process in a direct bandgap semiconductor.

2.1.4.3. Carrier lifetime

To understand the dynamics of optically excited states, the lifetime of excited states associated with energy relaxation of photogenerated carriers will be described. The following equation could express the energy conservation law:

$$\hbar v = E_2 - E_1 \ , \tag{2.4}$$

where E_1 and E_2 are the initial and final energy states. The time evolution of excited states N_2 using Einstein coefficients is as following:

$$N_2(t) = N_2(0)\exp(-A_{21}t) = N_2(0)\exp(-t/\tau) \ , \tag{2.5}$$

where t is time and τ is a lifetime of excited state [56]. The time-dependent population of excited state $N(t)$ obeying the exponential decay curve is shown in Figure 2.10 [58]:

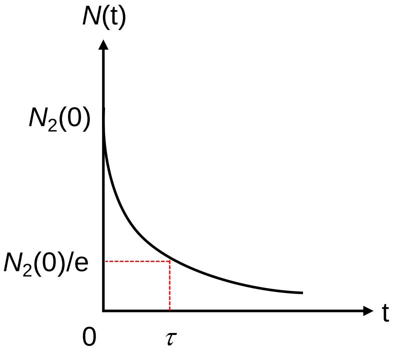

Figure 2.10 Time-dependent population of excited state $N(t)$.

Optically excited electrons relax from the higher excitation state to the ground state. During the relaxation, there are intrinsic radiative (emission) and non-radiative (non-emission) decay processes. The luminescence quantum efficiency is determined as follows:

$$\eta_{\mathrm{PL}} = k_{\mathrm{rad}}/(k_{\mathrm{rad}} + k_{\mathrm{nonrad}}) \ , \tag{2.6}$$

where the decay rates of the radiative and non-radiative processes are k_{rad} and k_{nonrad}, respectively. The non-radiative decay occurs in the absence of photon emission, where the corresponding energy is released through the phonon emission process. The non-radiative phonon emission process is much faster than the radiative process. Due to most materials' thermally activated non-radiative recombination process, the PL intensity (quantum efficiency) will drop sharply as the temperature increases [59]. The discussion on the radiative lifetime of ReS_2 will be described in Chapter 5.

2.2. 2D materials

The atomically thin 2D materials are emerging nanostructured low-dimensional materials with potential applications in advanced electronics and optoelectronic devices in the future. From this section, I will introduce the fundamentals and applications of atomically thin 2D materials.

2.2.1. Quantum confinement in a low-dimensional system

As mentioned above, if the size of a material is reduced down to a nanometer level, the material will become nanomaterials. The semiconductor nanoscale structures show unique optical properties strongly depending on their sizes, while the bulks do not. Due to the quantum confinement effect of electronic systems. According to the Heisenberg uncertainty principle, the momentum Δp_x of a particle confined in length Δx is given by:

$$\Delta p_x \sim \frac{\hbar}{\Delta x} \ , \tag{2.7}$$

where $\hbar$ is reduced Planck's constant. The confinement energy in the x-direction can be described as below:

$$E_{\text{confinement}} = \frac{(\Delta p_x)^2}{2m} \ \sim \ \frac{\hbar^2}{2m(\Delta x)^2} \ , \tag{2.8}$$

where m is the particle mass. If the confinement energy is larger than the kinetic energy [60], it will become notable as described below:

$$E_{\text{confinement}} = \frac{\hbar^2}{2m(\Delta x)^2} > \frac{1}{2} k_{\mathrm{B}} T \ , \tag{2.9}$$

where k_{B} indicates the Boltzmann constant and T indicates temperature. Quantum size effects with confined particles will be significant in the structure with its size of Δx as follows:

$$\Delta \mathrm{x} < \sqrt{\frac{\hbar^2}{m k_{\mathrm{B}} T}} \ , \tag{2.10}$$

according to eq. (2.7), the quantum confinement effect appears in the electron confined in the semiconductor nanostructure with Δx less than 5 nm at room temperature (300 K), where electron masses m_e* is ~ 0.1 m_0 (m_0 is free electrons mass). The electronic systems exhibit a strong quantum confinement effect in the atomically thin sheet thickness of 1 nm, studied in this thesis.

Figure 2.11 shows the quantum confinement of 3D–0D structures. In the case of 3D bulk, the density of state (DOS) is proportional to $E^{1/2}$ as a function of energy E. DOS in two-dimensional (2D) quantum wells exhibits a step-like function, while the DOS of one-dimensional (1D) quantum wire is proportional to $E^{-1/2}$. An increment function represents the DOS of a quantum dot (0D). The divergence of DOS at low-dimensional semiconductors causes strong light-matter interactions in resonance energy. The characteristic was experimentally measured using scanning tunneling spectroscopy by differential conductance dI/dV [61].

The quantum wells are usually used in the application of semiconductor lasers because the quantum confinement effect makes DOS have a steep edge, makes electrons gather in the energy state of edge, thereby forming a specific transition, which contributes to the low threshold current laser operation. The laser emission efficiency can be further improved in further low-dimensional systems of 1D quantum wires or 0D quantum dots due to the sharpening of DOS [60].

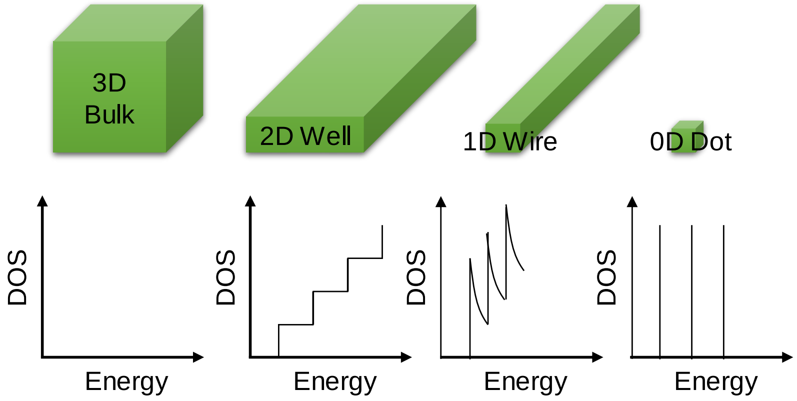

Figure 2.11 Reduction of dimensionality from 3D (bulk) to 0D (quantum dot) of semiconductor systems, with the relation of the density of states (DOS) to the confinement energy.

2.2.2. Variety of 2D materials

2D materials, also known as monolayer forms, are atomically thin materials made up of a single atomic layer and a few layers of atoms. Electrons can only move freely in a 2D plane and are limited in the out-of-plane direction in a 2D material. In the monolayer form of 2D materials, its adjustable bandgap properties and controllability of spin freedom have been extensively studied. Furthermore, many applications of 2D materials are currently under investigation in fundamental research and toward industrial levels. There are already prototypes for electronic chips, lasers, photodetectors, transparent conductors, energy storage and -conversion devices and various sensors from mechanical to biological devices [62–66]. Some of these prototypes are now maturing and available as commercial products. In this section, I will briefly introduce the various 2D materials.

2.2.2.1. Characteristic and benefit for 2D materials

From the discovery of graphene in 2004, studies in atomically thin 2D materials have made fast progress in various research fields since 2010 [10]. It has been found that there are many types of 2D materials, such as hexagonal boron nitride (*h*-BN) as an insulator, TMD as a semiconductor, and graphene as a semi-metal. The mechanical exfoliation from bulk material has been widely used to prepare atomically thin 2D materials, which accelerates research on 2D materials. Many new viewpoints still need to be excavated due to their outstanding advantages of 2D materials even past decade.

In layered bulk materials, each layer stacks by weak van der Waals interaction. If an external force is added to layered bulk material, the material becomes simply exfoliated because of relatively weak van der Waals force. Consequently, the monolayer material only has covalent bonds in the plane and becomes mechanically much stronger than the bulk by removing the weak links. For instance, monolayer graphene has 100 times stronger tensile strength than graphite. So, even graphene is stronger than steel, while the graphite pencil is fragile. Another significance in a monolayer material is the addition of a significantly higher surface area-to-volume ratio, which strongly affects and accelerates the chemical reactions than bulk forms, with the potential application of high sensitivity sensors [67–74].

The strong quantum confinement of electrons in the atomically thin 2D plane causes novel electronic and optical properties [75,76]. Once the material is thinning down to the 2D limit, the perpendicular periodicity of electronic systems is removed, which causes the confinement of electrons into the 2D plane and modifies its electronic band structure. Another important aspect of 2D materials is reduced dielectric screening among carriers in Coulomb interaction, making the excitons more stable than those in bulk, as shown in Figure 2.12. In the 3D materials, the electric field lines interacting between electron and hole will be shielded by the material with a high dielectric constant. In electron and holes in quantum wells (quasi-2D systems), the parts of electric field lines are spread in the low dielectric materials and vacuum, i.e., the screening is reduced compared to the 3D bulk. In the atomically thin 2D materials, most electric field lines are spread in the vacuum, making Coulomb interactions between electron and hole stronger.

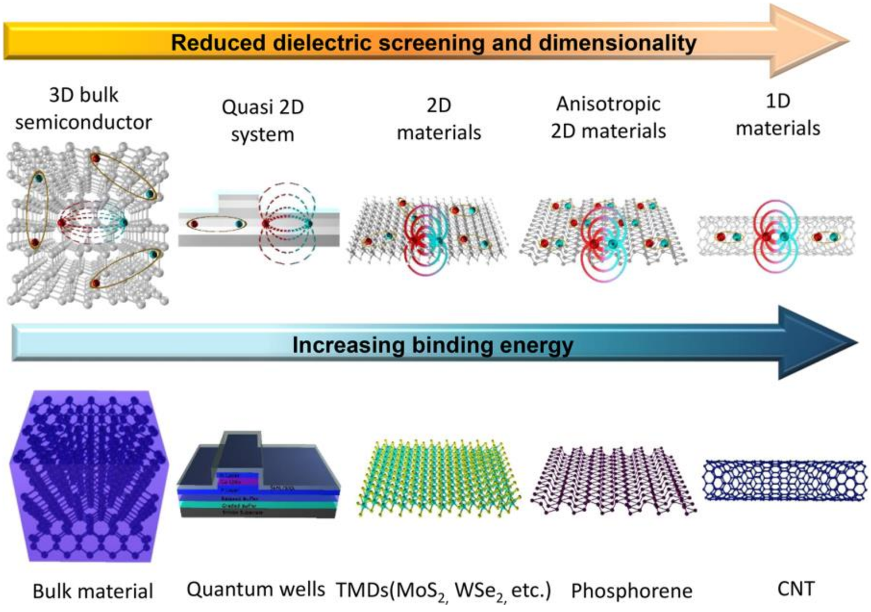

Figure 2.12 Schematic of dielectric screening and binding energy of exciton confined in each dimension. The binding energy is enhanced by reducing the dimensionality (Taken from Ref. [50])

According to the analogy of hydrogen atom picture, the binding energy of exciton E_n could be described as,

$$E_n = -\frac{\mu}{m_0}\frac{1}{\varepsilon_{\mathrm{r}}^2}R_{\mathrm{y}} = -R_{\mathrm{y}}^* \ , \tag{2.11}$$

where μ is exciton reduced mass ($1/m = 1/m_e^* + 1/m_h^*$, m_e^* and m_h^* are an effective mass of electron and hole, respectively), m_0 is free electrons mass and R_{y} is Rydberg energy of the hydrogen atom. The $R_{\mathrm{y}}^*(=\frac{\mu}{m_0}\frac{1}{\varepsilon_{\mathrm{r}}^2}R_{\mathrm{y}})$ is the effective exciton Rydberg energy. n is the principal quantum number and ε_{r} indicates the dielectric constant (relative permittivity). If the bandgap is large, the binding energy becomes large because the material is insensitive to polarization. As mentioned above, the exciton (bound electron-hole pair by Coulomb interaction) is modeled by the hydrogen-like Rydberg model. However, the physical values of the mass of particles and dielectric constant differ between exciton in the solid and hydrogen atom in the vacuum. The effective Rydberg's energy R_{y}^{*} is used to characterize the exciton binding energy in the solid.

The strongly bound excitons have a larger optical transition rate due to the closer distance of electron and hole. The scale of exciton size defined as Bohr radius α_{B} is expressed by the following formula:

$$\alpha_{\mathrm{B}} = \alpha_{\mathrm{H}} \frac{m_0 \varepsilon_{\mathrm{r}}}{\mu} = \alpha_{\mathrm{H}} \frac{m_0 \varepsilon_{\mathrm{b}}}{\mu \varepsilon_0} \ , \tag{2.12}$$

where a_{H} is the Bohr radius of a hydrogen atom. ε_{b} as static background dielectric constant and ε_0 as permittivity of vacuum. The energy of light absorption (emission) energy in the monolayer form will be changed from bulk due to quantum confinement with reduced dielectric screening, as described above. Moreover, the energies might also be changed depending on the number of layers of 2D material by the electronic band structures described after.

2.2.2.2. Graphene

Graphene is the most typical 2D material with a single-carbon atomic layer, which has a hexagonal crystal structure with *sp*^{2} hybridization (Figure 2.13). The graphene shows outstanding physical properties such as tensile strength, elasticity and electrical conductivity [77]. Recently, mechanical exfoliation and chemical vapor deposition (CVD) methods have been employed to produce graphene [78].

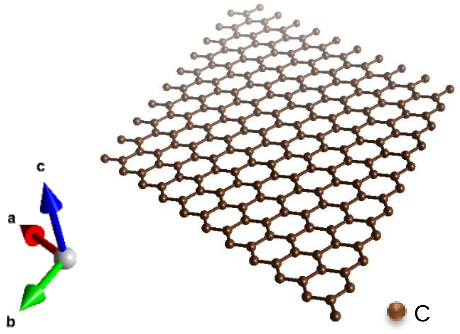

Figure 2.13 Crystal structure of graphene.

The electrons in the graphene are called Dirac mass-less electrons, which means that the electrons, like light, cannot rest. The electron velocity is about 1/300 of the speed of light, which is slower than the actual speed of light, but this is high electron velocity in the materials, showing the extremely high carrier mobility $\mu > 10^4$ cm^2/Vs. The energy dispersion relation without a gap is a cone-shaped so-called Dirac cone due to the symmetry of carbon crystal structure [79] (hexagonal honeycomb lattice). Graphene has been involved in field-effect transistors, solar cells and sensors [80].

2.2.2.3. *h*-BN

Figure 2.14 shows a schematic of the crystal structure of *h*-BN. It has a honeycomb structure, similar to graphene. The bulk *h*-BN stacked with multilayer structure due to weak van der Waals interaction and B–N–B network with sp^2 hybridization is formed. The *h*-BN with a wide bandgap (5.9 eV) and stable properties in air [81] can be used as a tunnel barrier and an ultraviolet light source. The atomically flat *h*-BN with fewer dangling bonds and charge traps on the surface could be an ideal substrate for 2D materials. Moreover, *h*-BN has also physically and chemically stable without reacting with other substances. The *h*-BN shows many potential applications in electronic and optical devices and substrate and cover layers of 2D materials [82–84].

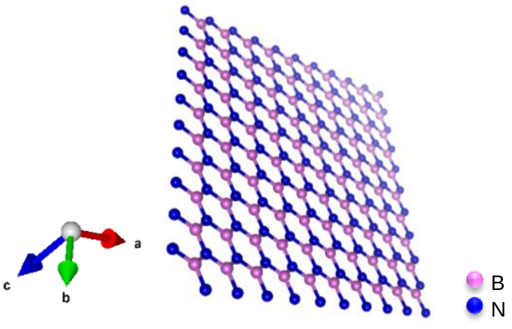

Figure 2.14 Crystal structure of *h*-BN.

2.2.2.4. Black phosphorous

BP is the most stable allotrope among a family of phosphorus. Figure 2.15 shows the atomic structure of BP. In bulk BP, a phosphorus atom is covalently bonded with three adjacent phosphorus atoms to form a corrugated layer structure, and layers are stacked via van der Waals interaction. Compared with other 2D materials, black phosphorus has a characteristic wrinkled structure and a double-layered structure along the zigzag direction. The wrinkled structure gives black phosphorus a higher specific surface area and anisotropic physical properties depending on the in-plane crystal directions [85].

The BP shows various bandgap tunability (0.3–2.0 eV), which contrasts with the zero-band gap nature of graphene [86]. This adjustable bandgap shows a wide absorption range from infrared to visible light region. Additionally, BP also has a higher carrier mobility (103 $cm^2V^{-1}s^{-1}$), which shows potential applications on electronics and optoelectronic devices. However, black phosphorus is also well-known as a typical unstable 2D material showing rapid degradation under ambient conditions. The anisotropic characteristics have also been found in other 2D materials such as ReS_2. However, the ReS_2 shows higher stability than BP, which will be discussed in Chapter 4, 5, 6.

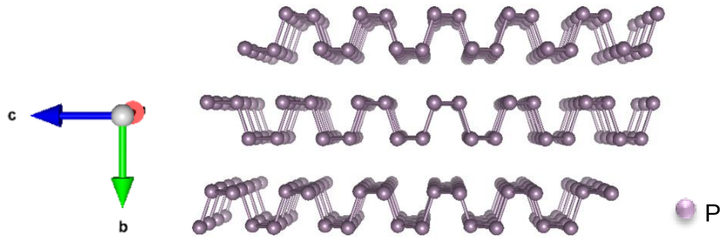

Figure 2.15 Crystal structure of BP.

2.2.2.5. TMDs

In TMDs with a chemical formula of MX_2, M refers to transition metal elements (such as Mo, W and Re), and X refers to chalcogen elements (such as S, Se and Te). A monolayer form of TMDs exhibits X-M-X sandwiched structure (as shown in Figure 2.16). The van der Waals forces between layers are weak, but there are strong covalent bonds in the plane of the layered bulk MX_2. Therefore, the bulk crystals could be easily mechanically exfoliated into thin layers similar to graphene. I will introduce the details of TMDs materials in the next section.

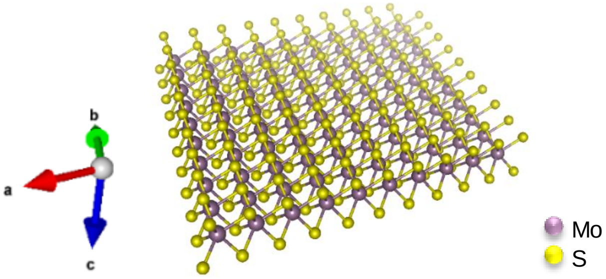

Figure 2.16 Crystal structure of MoS_2.

2.2.3. Overview of TMDs

The TMDs have unique electrical and optical properties. When the TMDs materials are made thin down from bulk to monolayer form, its energy band structure will change from indirect to direct. These peculiar electrical and optical properties in atomically thin semiconducting materials have promoted the application of optoelectronic devices compared to graphene [79–82]. Moreover, artificial heterostructure combined with TMDs and various 2D materials can be produced, which are expected to exhibit a novel platform for device applications [87]. The reduced dielectric screening and large Coulomb attractive interaction yield a rich manifold of photoexcitation, such as excitons (with strong binding energy), positively or negatively charged trions resulting from high carrier doping levels (from the substrate, vacancies, adsorbates etc.).

2.2.3.1. Crystal structure

Molybdenum disulfide (MoS_2) is the most typical TMDs material. Figure 2.17 shows the polytopes of TMDs structure with various metal atom coordination and stacking orders, indicated by 2*H*, 3*R* and 1*T* phases. The *H*, *R* and *T* are denoted by hexagonal, rhombohedral and tetragonal (octahedral) symmetry, respectively, while 1, 2 and 3 are assigned to layer numbers that correspond to one unit cell. The 1*T* phase has an octahedral coordination with metastable metallic structure; the 2*H* phase contains two Mo–S unit cells with a stable structure; the 3*R* structure has one more Mo–S unit cell than the 2*H* phase, with metastable structure. The two metastable states of the 1*T* and 3*R* phases could be transformed into a stable 2*H* phase at high temperatures. The 1*T* phase at TMDs has metallic properties, while the 2*H* and 3*R* phases exhibit semiconducting properties [88,89].

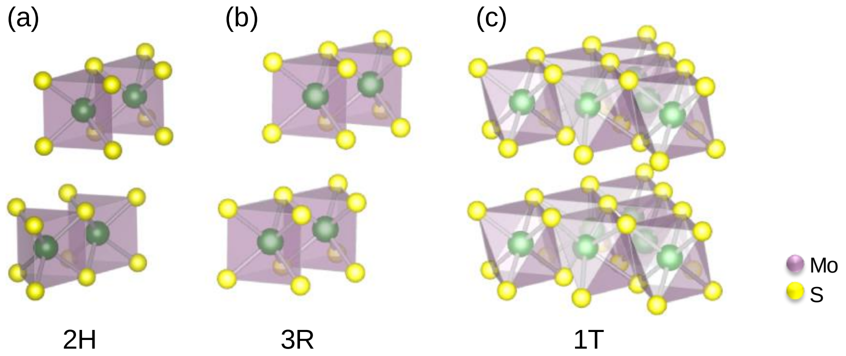

Figure 2.17 Crystal structure of polytopes of MoS_2 with (a) 2*H*, (b) 3*R* and (c) 1*T* phases. (Reproduced with permission from Ref. [88]. (c) (2015) The Physical Society of Japan.).

2.2.3.2. Electronic band structure

Figure 2.18 shows the energy band structure of bulk and monolayer MoS_2. For the bulk MoS_2 case, the VBM and CBM is in different momentum spaces of Γ point and between Γ and K point, respectively, which suggests that the bulk MoS_2 belongs to the indirect semiconductor bandgap at 1.2 eV. By contrast, the VBM and CBM exist in the same momentum space of K point in the monolayer MoS_2, suggesting the direct bandgap semiconductor with band energy of 1.9 eV. The most significant properties of MoS_2 are large modifications of electronic band structure, including the value of bandgap and indirect to direct gap transition depending on layer number of MoS_2. Moreover, the monolayer MoS_2 as a direct bandgap semiconductor overcomes the limitation of zero bandgaps in graphene and has been widely applied to optoelectronic device applications [90,91].

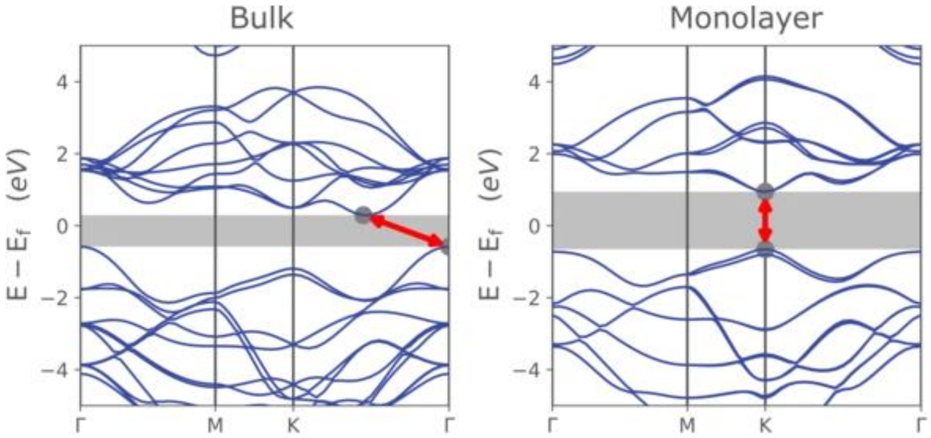

Figure 2.18 Band structure of bulk (left) and monolayer MoS_2 (right). (Image remains the copyright of Ossila. It was taken with permission from Ossila.com, Ref. [92]).

2.2.3.3. Raman scattering and photoluminescence spectroscopy

A monolayer of MoS_2 has a unique and strong PL in the visible wavelength because of its direct bandgap nature. This is unlike bulk and thick MoS_2 with a few layers, which belongs indirect-bandgap semiconductors with showing weak PL signals. This unique characteristic makes monolayer MoS_2 a good candidate for optoelectronic applications.

Raman scattering spectroscopy is widely used in determining the layer number of 2D materials. Figure 2.19 shows the Raman scattering spectra of MoS_2. The two spectral fingerprints of E^1_{2g} and A_{1g} modes at around 382 and 405 cm^{-1} are observed, where E^1_{2g}

mode and A_{1g} mode come from the in-plane S–Mo–S vibration and S atom out-of-plane vibration of, respectively. The layer number could be estimated by separating the two spectral fingerprints of E^1_{2g} and A_{1g} modes. As the number of layers increases, these two peaks become more separated, reaching 384 and 404 cm^{-1}, which the MoS_2 layers experience higher van der Waals force and long-range coulombic interlayer interactions, which contributed to the blue shift in E^1_{2g} mode and red-shift in A_{1g} peak.

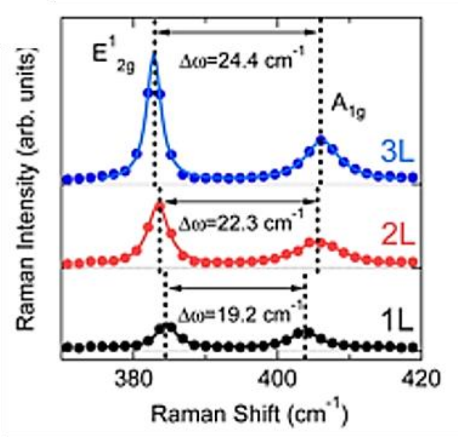

Figure 2.19 Raman spectra for 1L - 3L MoS_2. (Taken from. Ref. [93]).

Figure 2.20 shows PL spectra of MoS_2 with different layer numbers. The PL intensity drastically increases from bilayer (2 lay.) to monolayer (1 lay.) due to the change of band structures from indirect to direct band natures. Moreover, PL spectra with their intensity have also been changed, depending on the layer number of MoS_2 made to thin down from bulk (6 lay.) to monolayer limit (1 lay.). The characteristic PL peaks near ~1.9 eV (A exciton), at ~2.1 eV (B exciton) and below 1.6 eV (indirect exciton) is assigned, where the binding energy of exciton is evaluated as to be the extremely large value of > 500 meV in monolayer MoS_2. Hence, the exciton in monolayer MoS_2 is stable even at high temperatures above room temperature.

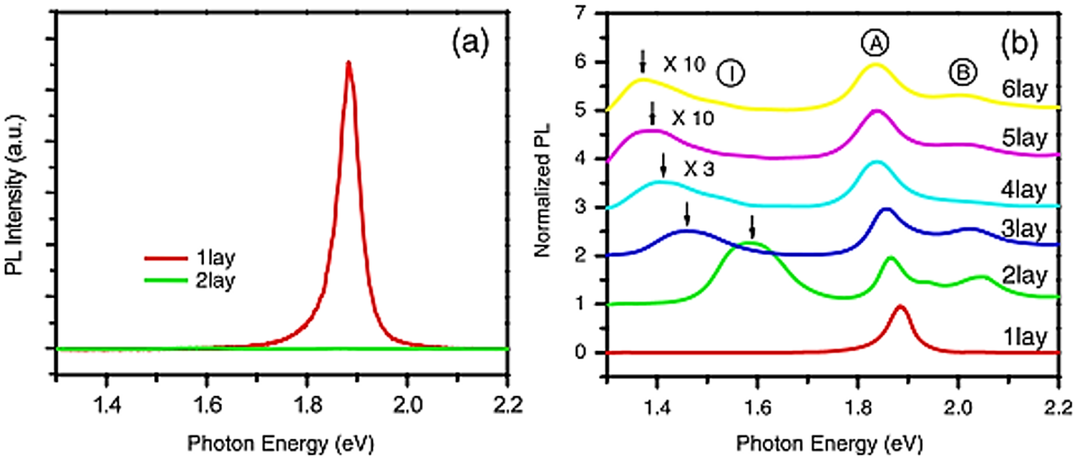

Figure 2.20 (a) PL spectra of 1L, 2L-MoS_2. (b) PL intensity normalized at peak A from 1L to 6L-MoS_2. (Taken from. Ref. [91]).

2.2.3.4. Valley polarization

Electrons have different internal degrees of freedom, such as charge and spin. During past decades, spintronics has matured through the manipulation of the spin degree of freedom. Recently, the discovery of valley degree of freedom in the momentum space, described below, has opened the new research fields of valley electronics (valleytronics). The spin state of the excited electron will not change during the photoexcitation process; however, the selective spin excitation of electrons in different valleys by light can be achieved in the valley and spin coupled system in monolayer TMDs with symmetry breaking and strong spin-orbit coupling. In Figure 2.21, the spin-polarized electrons with specific valleys (K or K’) are selectively excited by the circularly polarized light. The σ^+ (σ^-) circularly polarized light can excite the electrons with spin-up (down) and holes with spin-down (up) in the K (K’) valley, where K and K’ valley is inverted by the time operational connection, the spin angular momentum of the electron is reversed [94].

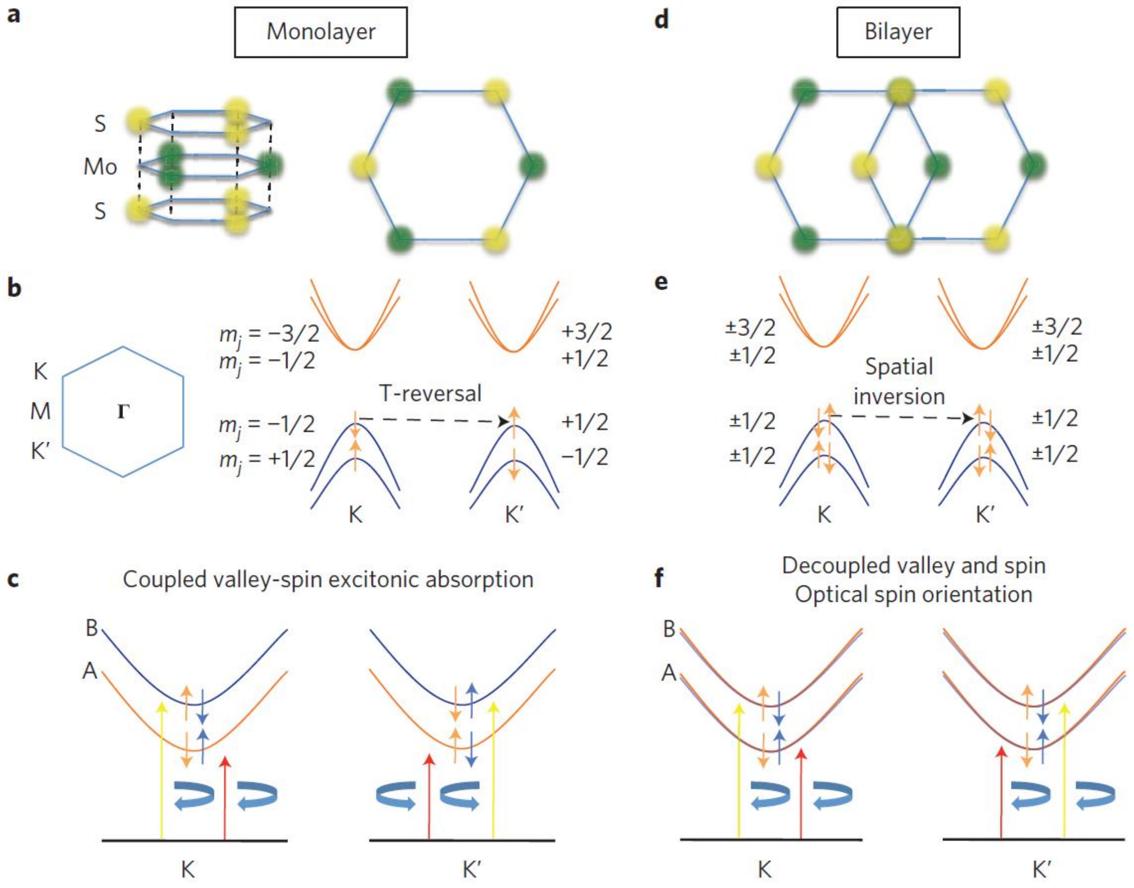

Figure 2.21 (a) and (d) Crystal structure of 1L, 2L-MoS_2 and (b), (c), (e) and (f) their spin valley characteristic (Taken from. Ref [94]).

2.2.3.5. Carrier dynamics in TMDs

Studying photogenerated carrier (exciton) dynamics can help us understand the optical response, photophysical mechanism and energy band structure in TMDs materials. Time-resolved photoluminescence (TRPL) and pump-probe techniques are typical ultrafast spectroscopy methods in measuring photocarrier (exciton) dynamics in the time scale of nanosecond to several hundred femtoseconds. The energy relaxation process and lifetime of photogenerated carriers (exciton) can be comprehensively investigated in TMD materials by utilizing transient spectroscopy with a high temporal resolution, which also provides important information on design, optimization and application of high-performance TMDs optoelectronic devices.

2.2.3.6. Anisotropic materials in TMDs family

The distorted crystal structure with symmetry reduction causes intriguing properties concerning electronic, thermal, valley and optical responses in 2D material materials [95–97], which have been intensively studied, such as in black phosphorene with in-plane anisotropy, as already mentioned in section 2.2.2.4. This thesis will focus on rhenium disulfide (ReS_2), which has become a new member of anisotropic TMD materials. Unlike most of the 2D layered materials, ReS_2 shows decoupled stacking structure from bulk to 1L. The intensity of Raman scattering and PL spectra increases with an increase in the layer number, suggesting that ReS_2 can provide new physical and optical properties due to its weak interlayer coupling. Compared with BP, ReS_2 is a naturally occurring yet extremely rare TMDs, so it is environmentally stable, which makes it an ideal candidate for applications in ambient conditions [98–100]. Moreover, the $ReS_{2,}$ as an *n*-type semiconductor, exhibits bi-axial characteristics [101].

The top side of the ReS_2 crystal structure is shown in Figure 2.22(a). Compared to other TMDs with a 1*H*-phase trigonal prismatic crystal structure, ReS_2 has a distorted 1*T*-phase octahedral structure. These ultimately distort the hexagonal symmetry, which unveils that Re chains break in one straight direction due to the strong metal-metal bond, which is defined as the b-axis. The triclinic structure shows in-plane anisotropic properties along the b-axis. Thus, in the unit cell, rhenium and chalcogen atoms are forced out into the same plane and cause anisotropy in the plane and out-of plane lattice vector.

The interlayer van der Waals interaction of bulk ReS_2 is extremely weak, and it exhibits electronic and vibration decoupling characteristics similar to monolayer ReS_2, which suggests that the properties of ReS_2 will not be strongly affected by the number of layers. Unlike other TMDs, when ReS_2 is gradually thinned from bulk to monolayer, there will be no transition from an indirect bandgap to a direct bandgap due to extremely weak interlayer coupling. This is mainly because there are seven valence electrons in the outer layer of the Re atom, leaving a lone pair of electrons after forming the Re-Re bond, resulting in mutual repulsion between the layers. Simultaneously, the total energy is reduced, forming a distorted 1*T* structure, and thus the interaction between layers is further weakened.

The two kinds of exciton state denoted as exciton1 and exciton2 are shown in the ReS_2 monolayer, as shown in Figure 2.22(a). The exciton1 with lower energy shows wavefunction spread along a parallel direction of the rhenium atomic chains (b-axis). In contrast, the exciton2 with higher energy shows the wavefunction spread relative to approximately 45° along the b-axis. The existence of two types of exciton demonstrates the anisotropic linear polarization dependence of optical responses in ReS_2, which lays its account with utilization for excitonic optoelectronic devices. The initial stage of density-functional theory (DFT) calculation suggests that the ReS_2 shows direct bandgap semiconductors from the bulk counterparts and monolayer limit, as shown in the calculated band structure of 1L-ReS_2 in Figure 2.22(b). These are different from typical TMDs, will be discussed more in detail after.

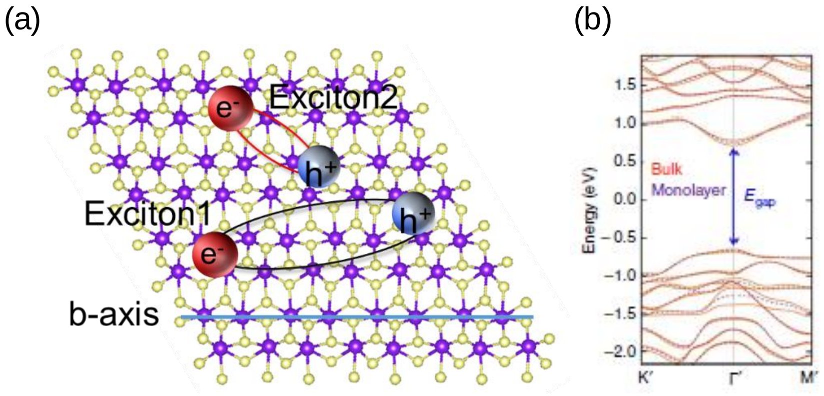

Figure 2.22 (a) Crystal structure of distorted 1T ReS_2. The blue line is Re chains indicated the b-axis. Exciton1 and Exciton2 are two types of bound electron-hole pairs with anisotropic alignment. (b) DFT calculation of electronic band structure for bulk (orange line) and monolayer (purple dashed-line) ReS_2. (Taken from Ref. [102]).

Figure 2.23(a) presents the DFT calculation for the electronic band structure of 1L-ReS_2 with its partial DOS, which indicates that ReS_2 could be identified as a semiconductor with a direct bandgap at Γ point. The partial DOS means that edges of the valence and conduction bands consist of Re-*d* and S-*p* states, respectively. The electronic band dispersion in DFT calculation with consideration of spin-orbit (SO) interaction is shown in Figure 2.23(b) to understand how the SO interaction affects the energy band structure of ReS_2. The bandgap energy of 1L-ReS_2 is reduced from 1.43 to 1.30 eV considering SO, and the enlarged images around the band edge at Figure 2.23(b) reveal the significance of SO interactions at distorted 1*T* phase.

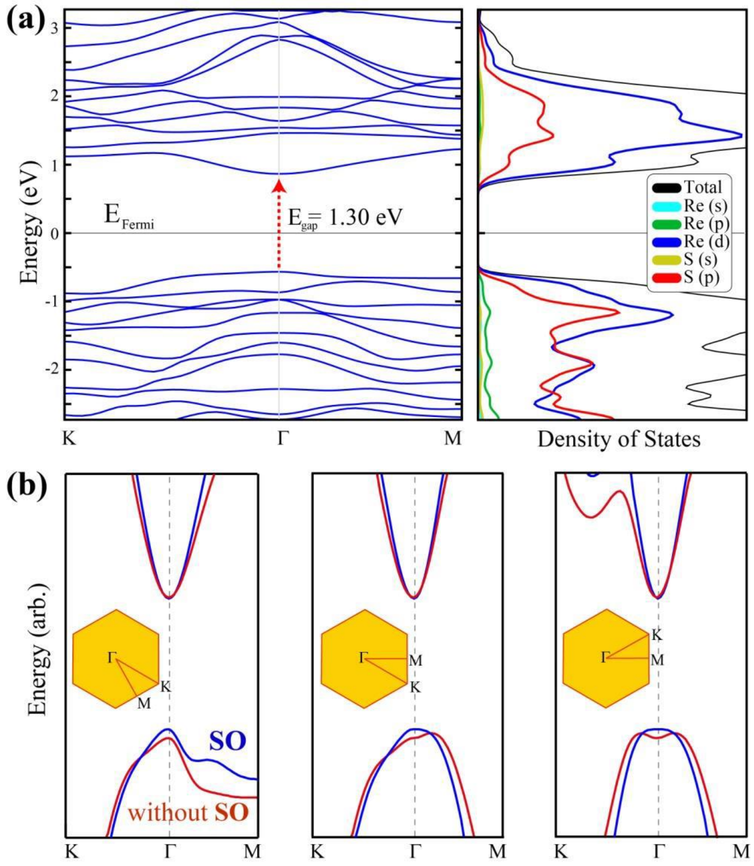

Figure 2.23 (a) Calculated energy band dispersion (GGA + SO) and partial DOS in 1L-ReS_2. (b) Zoom-in plots of CBM and VBM in different momentum directions. (Taken from Ref. [102]).

Figure 2.24 (a) and (c) show the annular dark-field (ADF) images of ReS_2 by transmission electron microscopy. Figure 2.24(b) represents a schematic of crystal structures in ReS_2. The ADF image exhibits the Re-chain (b-axis) of ReS_2.

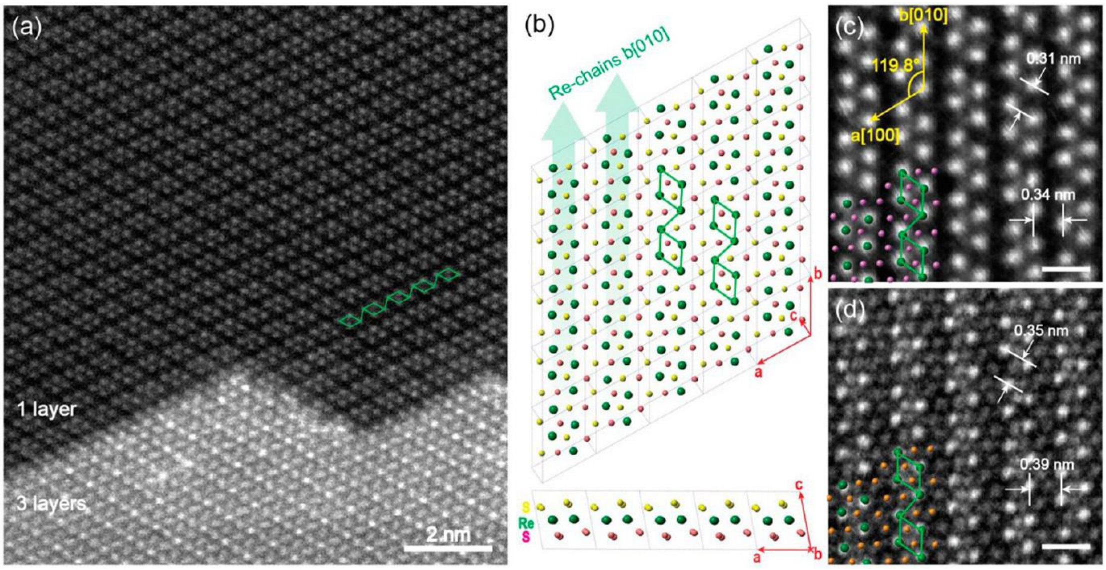

Figure 2.24 (a) ADF image of ReS_2 under low magnification conditions. The upper parts in the image show 1L with diamond-shaped phase structure, and the lower parts show 3L-stacking. (b) Crystal structure of ReS_2. (c), (d) ADF image of ReX_2 (X: S, Se). The lattice spacing for Re diamond chains is 0.34 nm and 0.39 nm, Re diamond-shape clusters, is 0.31 nm and 0.35 nm, in ReS_2 and $ReSe_2$, respectively, with a 0.5 nm scale bar. (Image remains the copyright of ACS. They are taken with permission from https://pubs.acs.org/doi/10.1021/acsnano.5b04851, Ref. [103]).

Raman scattering and differential reflectance ($\Delta R/R$) spectra have also shown the highly-sensitive response to the angle of incident light polarization due to the anisotropic structure of ReS_2. Figure 2.25(a) shows the Raman scattering spectrum of 1-layer (1L) to 4-layers (4L) ReS_2. There are five peaks of Raman modes: Mode I - Mode V contain two prominent peaks, and Mode III and Mode V show different responses with respect to the cleaved edge, along Re-chain (b-axis) (Figure 2.25(b)). A similar anisotropic response is also observed at differential reflectance spectra of 1L-ReS_2 (Figure 2.25(c)), where the intensity of exciton1 and exciton2 response parallel and almost perpendicular to the b-axis, respectively. Figure 2.25(d) shows the PL spectrum of ReS$_2$ with a different number of layers. In contrast with typical TMDs, PL intensity increases as increasing the layer numbers.

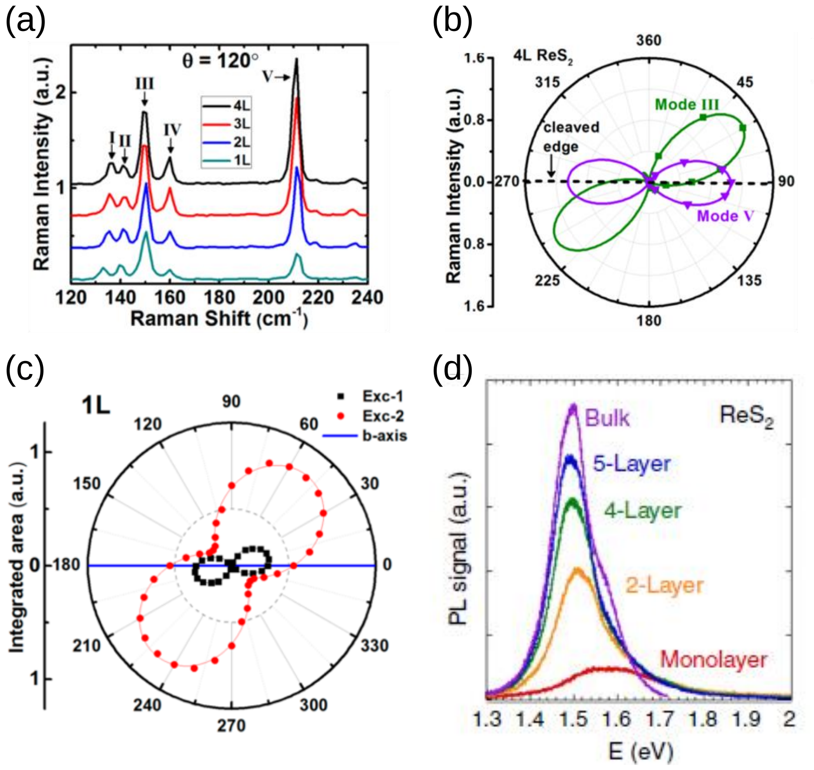

Figure 2.25 (a) Raman scattering spectra of ReS$_2$ with different layer numbers. (b) Polar plot of Raman intensity in Mode III and Mode V. (c) Polar plot of differential reflectance intensities showing anisotropic responses. (d) PL spectrum of ReS$_2$ different layer numbers. (Taken from Ref.(a,b) [104] (c) [33] and (d) [102])

The ReS$_2$, with highly anisotropic optical and electronic properties, must provide an additional degree of freedom and new opportunities in developing its applications in optical and electrical devices [105–110]. However, there are still many things needed to clarify the optical and electronic properties. For example, the early stage of studies reported that ReS$_2$ remains a direct bandgap semiconductor from bulk to monolayer limit by DFT calculations. In contrast, the other experimental studies have reported that the band structure, including direct or indirect bandgap, strongly depends on the layer number. The understanding of electronic and optical properties, including the optically excited carrier dynamics, are still controversial and are not fully understood.

2.2.3.7. Application of ReS_2

The outstanding performance of ReS_2 provides many opportunities in the fields of rechargeable batteries, catalysis, optoelectronic devices, stimulus-response and photothermal therapy [111]. Based on the extremely weak interlayer coupling effect described above, ReS_2 leads to a fast ion diffusion rate and easy insertion-extraction of ions due to the large interlayer spacing (0.62 nm) with application prospects in the application of rechargeable batteries. The ReS_2 also has moderate adsorption, which makes it easier for ions or molecules to be adsorbed or desorbed, which is beneficial to promote the reaction rate of the catalytic system. Additionally, ReS_2 has strong light absorption in wide wavelength regions without limitation of layer numbers, which is easy for the preparation of photoelectric devices.

Another instance of applications being widely discussed and developed are optical devices. Extensive device studies have been conducted in the potential application of ReS_2 with taking advantage of unique asymmetric crystal structure, where Re chains are arranged in a parallel direction with a b-axis. This makes ReS_2 with many riveting anisotropic optoelectronic properties, making novel and important electronic and optical device applications realize. The ReS_2 exhibits anisotropic optical responses from near-infrared to visible light regions, useful for novel photodetectors with polarization selectivity. Furthermore, the photodetector based on heterostructures has also been researched, built by a combination of ReS_2 and other 2D materials [112–117]. In the photodetectors based on ReS_2/2D material heterostructure, light absorption and separation of photogenerated carriers (electrons and holes) could enhance gate tunable behavior, carrier mobility, photoresponsivity, external quantum efficiency and detectivity.

Chapter 3. Experimental procedure

Sample preparation, experimental method and the optical setup for the measurements in this study will be introduced in this chapter.

3.1. Sample preparation

As introduced in the previous chapter, weak van der Waals interactions exist between layer to layer at TMDs. Therefore, they can be easily mechanically exfoliated by a tape with weak adhesive properties [46] (Figure 3.1(a)). The detailed processes of mechanical exfoliation are shown in Figure 3.1(b). In this study, a piece of single crystal flakes of ReS_2 purchased (hq graphene) was mechanically exfoliated by a blue tape (Nitto Denko co, BT-130E), and then, small pieces of flake were transferred onto a cleaned Si/SiO_2 (SiO_2 thickness of 270 nm) or quartz substrate by using a polydimethylsiloxane (PDMS) film (Gel-pak, GEL-FILM PF-20/17-X4). The number of ReS_2 layers on the substrate was determined by optical contrast in optical microscopy image and optical techniques such as Raman scattering and PL spectroscopy. The thickness of ReS_2 was also measured by atomic force microscopy (AFM).

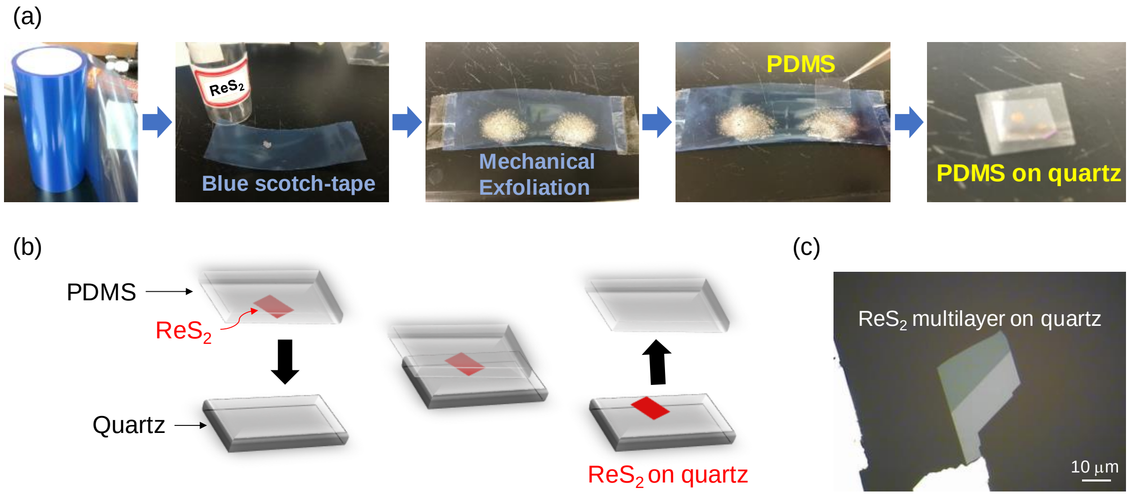

Figure 3.1 (a) Process of mechanical exfoliation method using a blue tape. The PDMS was used to transfer the flakes on the quartz substrate. (b) Schematic of dry-transfer process of thin ReS_2 on the quartz substrate. (c) Optical image of multilayer ReS_2 on the quartz substrate after the dry-transfer process.

Identification of ReS_2 flakes such as their thickness and crystal directions was executed by an optical microscope equipped in a micro-Raman spectroscopy system (Nanophoton, Ramantouch), as shown in Figure 3.2(a). A semiconductor laser of 532 nm was used to excite thin layers of ReS_2, and a cooled CCD camera equipped with a spectrometer in the Raman spectroscopy system has been used to measure Raman scattering or photoluminescence (PL) spectrum (Figure 3.2(b)). The details of Raman scattering and PL measurement will be discussed in section 3.4.

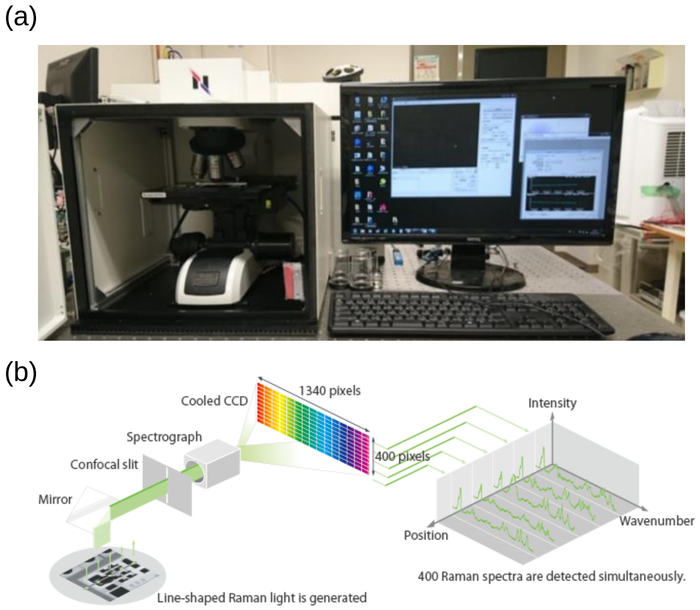

Figure 3.2 (a) Overview of micro-Raman spectroscopy system (Nanophoton, Ramantouch), and its optical microscope part is shown in the left part of the photograph. (b) Schematic representation of Raman scattering spectroscopy (Image remains the copyright of NanoPhoton Co. Taken with permission from https://www.nanophoton.jp, Ref. [118]).

3.2. Field-Effect Transistor device preparation

The field-effect transistor (FET) is used to tuning carrier density of thin layer ReS_2 in optical experiments. To fabricate a FET device, thin layers of ReS_2 were prepared by mechanical exfoliation and then dry-transferred from PDMS film onto Cr/Au electrodes on SiO_2/Si substrate. Electron-beam lithography (JSM-6500F, JEOL and SPG-724, Sanyu Electron) was used to pattern metal electrodes [113]. Figure 3.3(a) shows the dry-transfer process of thin layer ReS_2. The optical microscope image of thin layer ReS_2 on the electrodes as a FET structure is shown in Figure 3.3(b). To obtain highly reliable contacts between the thin ReS_2 and the metal electrodes, Figure 3.3(c) and (d) show a schematic of the vacuum thermal annealing with a gas mixture of Ar/H_2 (97:3), which maintained at 200°C for 2 h at 150 standard cubic centimeter per minute (sccm) flow rate. After the fabrication of the FET device, the carrier density could be controlled by applying back-gate voltage (V_G) on the thin layer ReS_2 device.

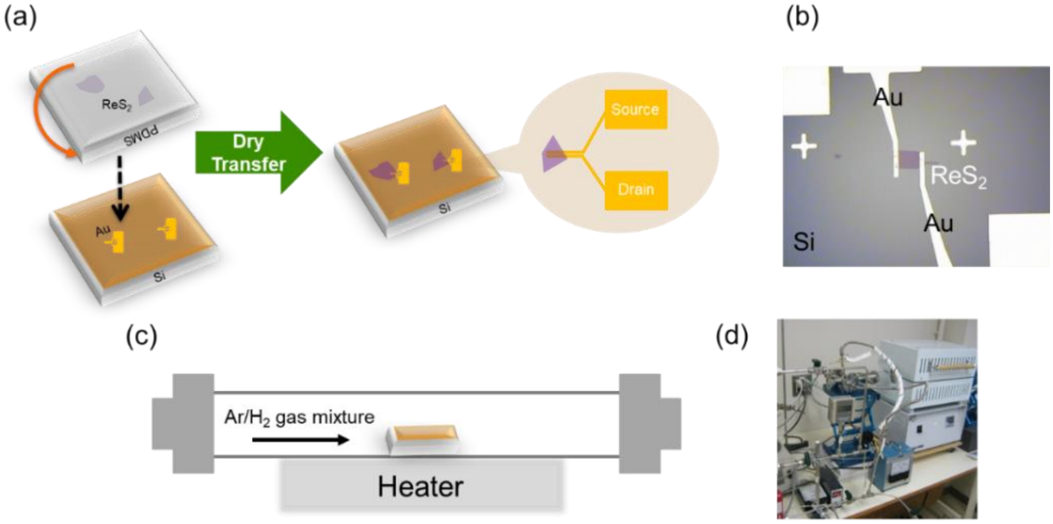

Figure 3.3 (a) Schematic of a fabrication process of thin layer ReS_2 FET devices by a dry-transfer method. (b) Optical image of ReS_2 FET device on SiO_2/Si substrate. (c) Schematic thermal annealing process and (d) photograph of a split-tube furnace (As-one co, Electric Furnace, MMF) for annealing FET devices.

3.3. AFM measurement

AFM (SII, Nano Navi IIs) was used to measure the thickness of ReS_2 after dry-transfer on SiO_2/Si or quartz substrate, with self-detected type cantilever probes (HITACHI, Micro Cantilever). The photograph of AFM is shown in Figure 3.4(a). DURING MEASUREMENT, the AFM probes parameter is set as follows: resonant frequency ~ 500 kHz, spring constant ~ 40 Nm^{-1}, scan rate ~ 0.29 Hz per line, the number of scan lines ~ 1024, and single-mode. Once the distance between the cantilever probe and sample surface reaches below 1 nm, the atomic force becomes significant. The cantilever probe starts scanning by monitoring the frequency, amplitude and phase of probe vibration. After scanning, the information will be converted into the height image. Figure 3.4(b) shows the typical AFM image of a few layer ReS_2 on a quartz substrate. Details on the results will be discussed in section 4.3.

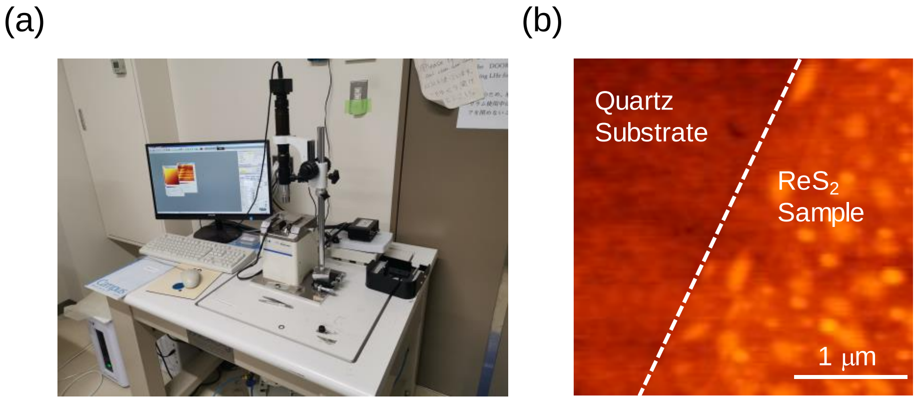

Figure 3.4 (a) Photograph of AFM (SII, Nano Navi IIs). (b) Typical AFM image of thin layer ReS_2.

3.4. Raman and PL spectrum measurement

Raman scattering and PL spectrum measurement by micro-Raman setup has been mentioned in section 3.1. The main purpose of these measurements is to identify the layer number of thin layer ReS_2 and characterize their fundamental optical properties. Raman scattering process occurs due to the interaction between light and materials, where the scattered light contains a different wavelength (color) from that of the incident light. Raman shift, defined as the difference of incident laser light and scattered light-independent on the incident laser wavelength, is measured with an interaction between light and lattice vibrations (phonons) in the crystals. Lattice structures of materials could be conjectured by Raman scattering signal (shift) through the light-lattice vibrations (phonons) interaction. However, the PL spectroscopy gives us information on the recombination process of bound electron and hole pair (exciton) with emitting photons.

Figure 3.5(a) represents a simplified diagram of the micro-Raman spectroscopy setup. A continuous wave semiconductor laser (532 nm) was used for excitation light, and an objective microscope lens (×100, NA = 0.9) was used in the optical microscope. Raman scattering and PL signals from the samples were detected by spectrometer equipped with Si CCD detector. For thin layer ReS_2 with anisotropic structures, the linear polarizer, half-wave plate $(\lambda/2)$ or quarter-wave plate $(\lambda/4)$ were placed above the objective lens to observe the anisotropic optical properties by controlling the incident polarization angles of the excitation laser light. The green and solid red lines in Figure 3.5(a) schematic indicate the excitation of laser light and emission from ReS_2, respectively.

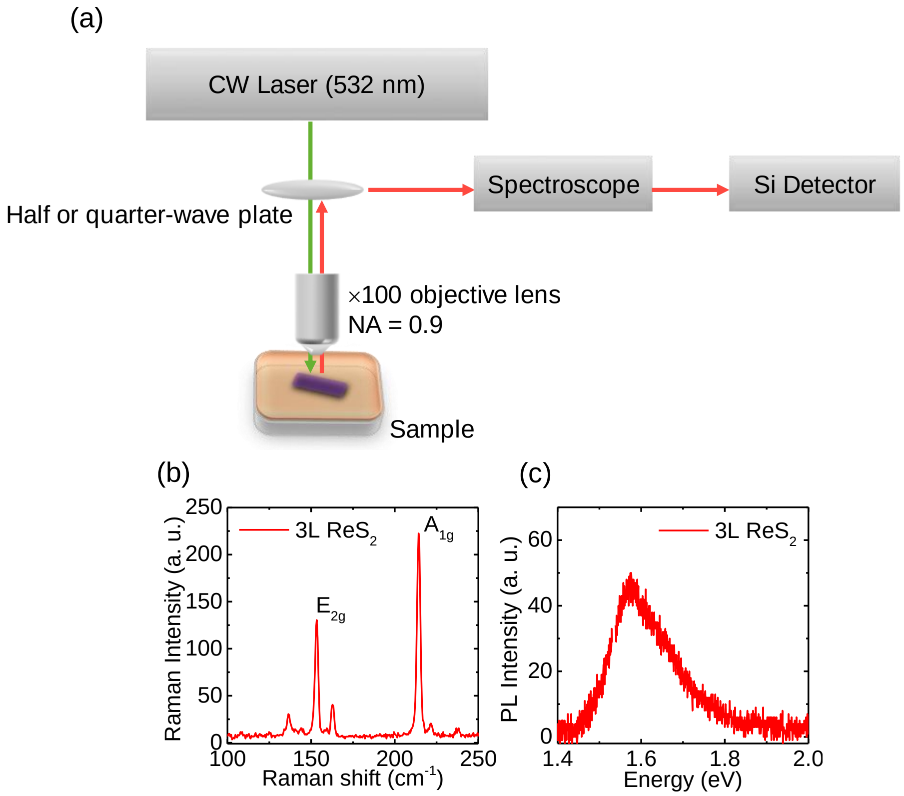

Figure 3.5 (a) Schematic of optical alignment in the micro-Raman setup. (b) Raman scattering and (c) PL spectrum of 3L-ReS$_2$ on a quartz substrate. Details will be described in Section 4.3.

3.5. Optical measurements

The optical measurement using a home-build setup revealed the optical properties and physics of the excitonic states in the thin layer ReS$_2$. In this thesis, almost all the results described after have been obtained using a home-made optical system, shown in Figure 3.6(a), (b). ReS$_2$ FET device was set into cryostat (ST-500-UC, JANIS) in the vacuum condition, and the temperature were controlled by the flow of liquid He (RH100, AIR LIQUIDE). The optical measurement was conducted by a continuous wave He-Ne semiconductor laser (2.33 eV) with a band pass filter (2.33 eV) to remove other emission lines. The source meter (Keithley 2400, TEKTRONIX) was used to monitor and modulate the carrier doping density for thin layer ReS_2 by applying a back-gate voltage. For polarization-resolved optical measurements, a broadband half-wave plate (THORLABS, WPH10E) was set above the objective lens (×100, NA = 0.5; MPlan APO NIR, Mitutoyo) and was fixed at 45° by b-axis of ReS_2 crystal direction in a linearly polarized excitation. The excitation laser light was focused on the sample surface with a spot size of ~2 μm. The emission signals with linearly polarized components were selectively detected and resolved by rotating a half-wave plate set in front of the monochromator (SP-2360, Princeton Instruments). Furthermore, a long pass filter (< 2.33 eV) was used to block the incident laser. Finally, the PL signals were detected with a CCD camera cooled with liquid N_2 (PyLoN: 100BR eXcelon, Princeton Instruments).

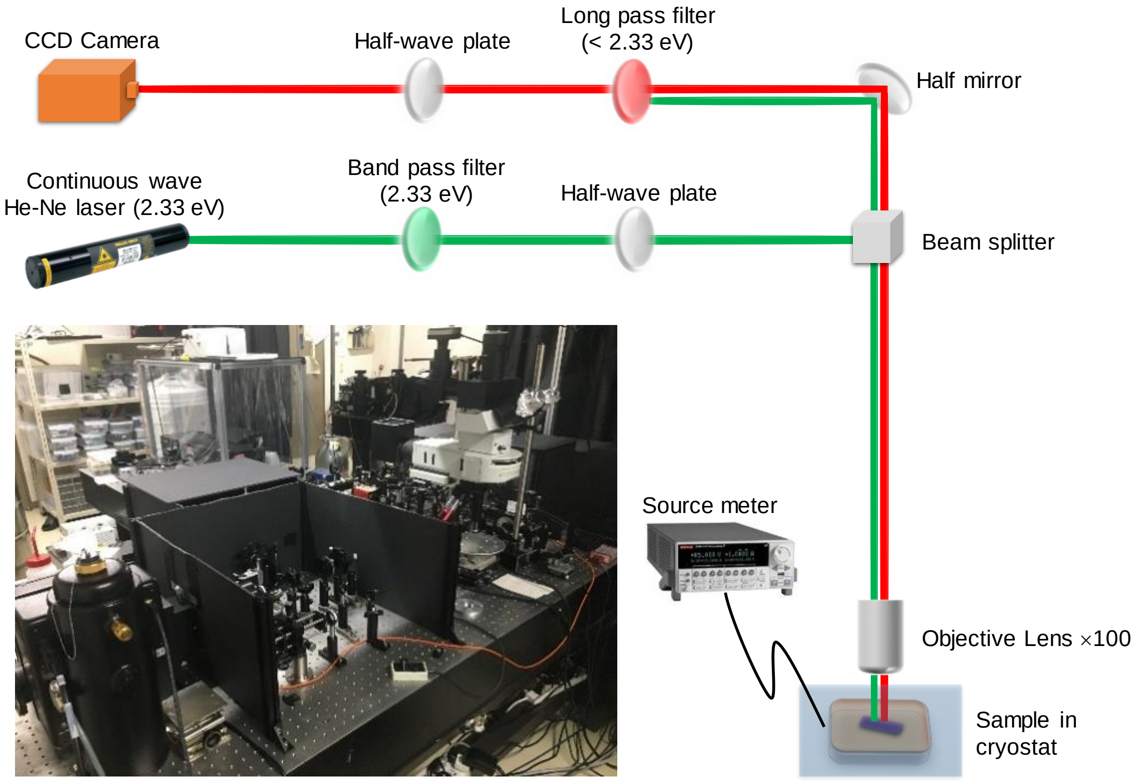

Figure 3.6 Schematic of home-built setup for optical measurements and photographs of

the optical setup.

3.6. Time-resolved PL measurements

Measurement of time-resolved PL has frequently been employed to understand ultrafast carrier dynamics. The Time-correlated single-photon counting (TCSPC) technique is the most widely used method for time-resolved PL measurement. The operating principle is recording the time-dependent intensity profile of the emitted photon (fluorescence) from the sample. In TCSPC, single photons are repetitively registered upon the reference timing of periodic excitation pulse like a stopwatch (start-stop), and then a single-photon histogram is formed over multiple cycles, as shown in Figure 3.7.

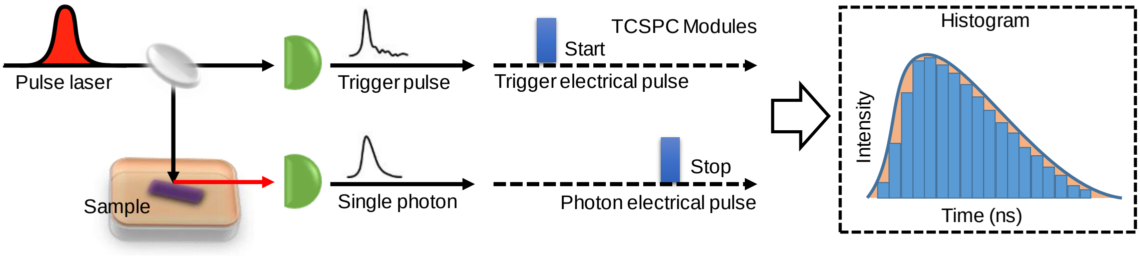

Figure 3.7 Schematic of the principle of TCSPC method for single-photon detection.

This TCSPC technique measured the time-resolved PL decay profile of atomically thin ReS_2. The schematic of the TCSPC system is shown in Figure 3.8. To optically excite a few layer ReS_2 samples, the monochromated and linearly polarized light from a super-continuum light source (laser energy of 1.80 eV, pulse width of ~20 ps and 40 MHz repetition rate) (NKT photonics, Extream-K) with a bandpass filter (1.80 eV) was used. A linear polarizer detected the signals through the long pass filter of < 1.65 eV using a Si avalanche photodiode (MPD, SPD-050-CTD-FC). The excitation laser was focused on the sample with ~2 μm (mentioned before). A liquid N_2-cooled charge-coupled device camera was used to detect a signal with a monochromator. The time-resolution of TSCPC is evaluated as about 60 ps from the instrumental response function in this setup.

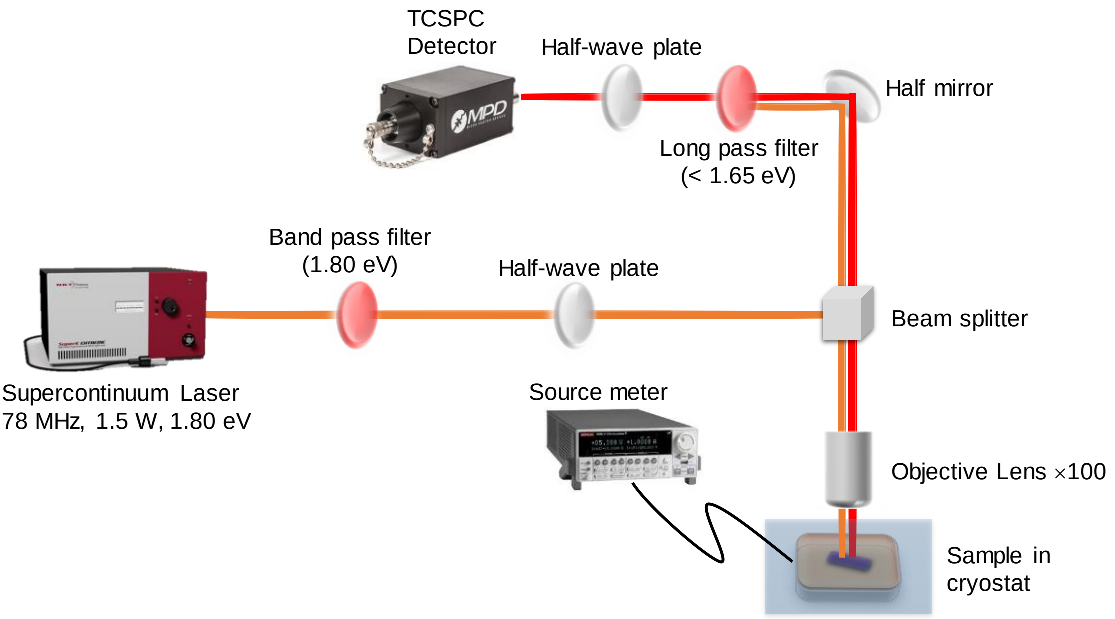

Figure 3.8 Schematic of time-resolved PL measurement using TCSPC method in this research and photographs of the optical setup for time-resolved PL measurement.

3.7. Pump-probe measurements

Pump-probe measurement is an alternative spectroscopic technique to study ultrafast carrier dynamics of materials. Two ultrafast pulse lasers as the pump pulse for generating the optically excited state (optical generation of carriers) and probe pulse for probing the change of optical absorption (reflectance) signals induced by pump pulses were used. The change of optical absorption (reflectance) signals was recorded with the pump-probe pulse delay time. Consequently, transient absorption spectroscopy with an ultrafast time-resolution determined only by the auto-correlation of the laser pulse (several hundred femtoseconds) could be obtained. The schematic of the pump-probe method is shown in Figure 3.9.

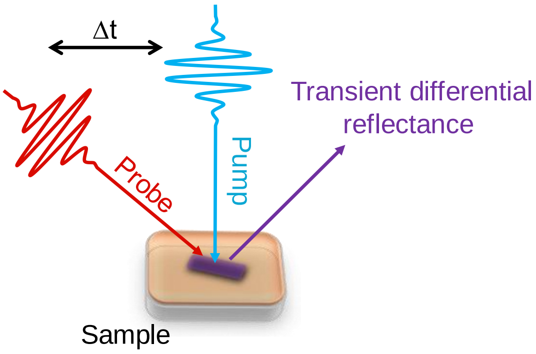

Figure 3.9 Schematic of the pump-probe method.

The transient changes of optical spectra, e.g., absorption-decrease (bleaching), -shift, -broadening and photo-induced absorption, contribute to the signals of pump-probe spectroscopy. The photoexcited carriers (electrons or holes) and excitons (electron-hole pairs) induced by the pump pulse block the optical absorption by the probe pulses due to Pauli-exclusion principle (state-filling effect), and then, decrease of optical absorption (bleaching) occurs until the lifetime of excited carriers or excitons in the excited state. The transient absorption decrease (bleaching) is mainly attributed to the differential reflectivity change $\Delta R/R$.

The pump-probe system in this research is shown in Figure 3.10. The transient differential reflectance was measured by the pump and probe method in this study. Linearly polarized pump pulse (1.8 eV, approximately 10 μW) with 200 fs duration and 1 MHz reputation rate excited to sample. The linearly polarized white light (1.46–1.77 eV) with a duration of 350 fs was used as a probe pulse. The pump and probe pulses were focused on the sample's spot size of ≈ 2 μm in diameter. The lock-in amplifier technique detected an ultrafast transient differential reflectance signal with a chopping frequency of ≈ 1 kHz as delay time (delay line) among linearly polarized pump-probe pulses. The reflected probe light was passed through a monochromator and detected by a Si photodiode. Differential reflectance $\Delta R/R = (R_{\mathrm{Sample+Quartz}} - R_{\mathrm{Quartz}})/R_{\mathrm{Quartz}}$ is derived from the reflectance of 3L-ReS$_2$ (R_{Sample}) and that of the transparent quartz substrate (R_{Quartz}) [119–121]. The temperature of 3L-ReS$_2$ was controlled by the cryogen-free cryostat (Montana, Cryostation s50).

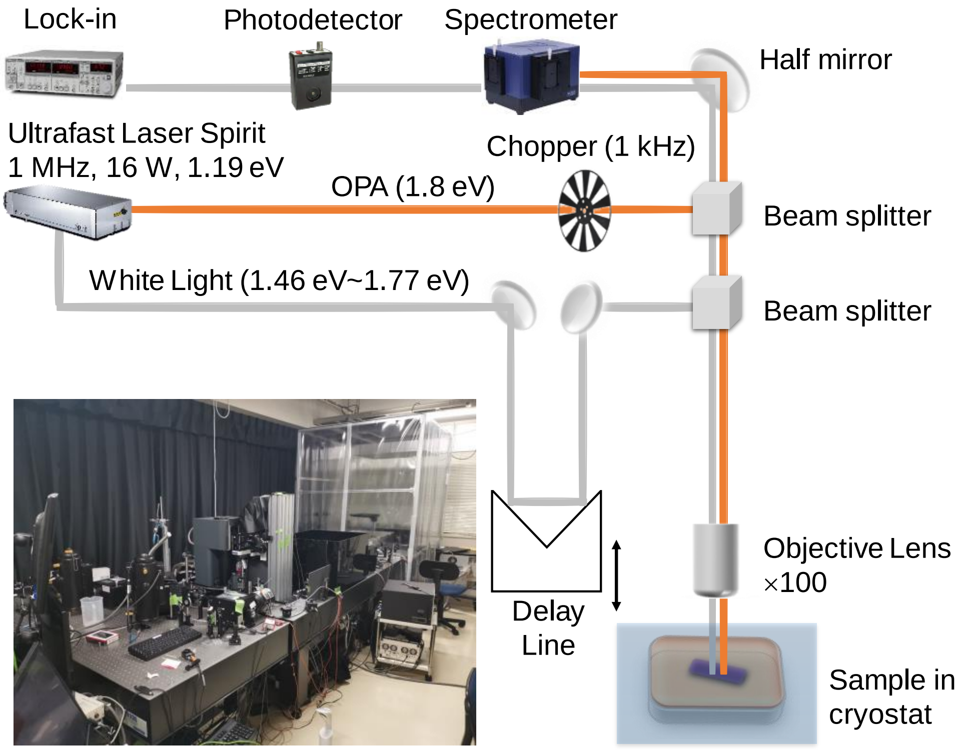

Figure 3.10 Schematic of pump-probe system and photograph of pump-probe setup used in this study.

Chapter 4. Exciton Dynamics in Few-Layered ReS_2

In this chapter, I will provide a brief introduction on ultrafast carrier and exciton dynamics in few-layered ReS_2, by using transient PL and ultrafast pump-probe spectroscopy.

4.1. Introduction

Atomically-thin layered materials including graphene and transition metal dichalcogenides possess intriguing physical properties originating from the two dimensional honeycomb structure [23,122–128], which has been mentioned in Chapter 2. ReS_2 is a new class of the layered material with reduced symmetry because of the distorted 1*T* structure, which imparts highly anisotropic one-dimensionality to optical and electronic properties [29,32,129–135]. The early studies reported that ReS_2 remains direct bandgap semiconductor from bulk to monolayer [102,136], while the other reported that the band structure depends on the layer number [51]. The understandings of electronic and optical properties including the optically excited carrier dynamics are still controversial, and are not fully understood.

In this chapter, I will describe the ultrafast carrier dynamics of 3-layer (3L) ReS_2. The direct and indirect exciton dynamics of a 3L-ReS_2 was investigated by polarization-resolved transient PL and ultrafast pump-probe spectroscopy in order to make a clear recognition on the band structure of 3L-ReS_2. The various time scales of the decay signals of the time-resolved PL, with monitoring of the populations of electron-hole pairs (exciton), and the transient differential reflectance, with monitoring of the populations of electrons and/or holes in the excited states, were observed. These findings provide important information regarding the indirect band gap nature of few-layered ReS_2 and its characteristic exciton dynamics, boosting the understanding of the novel electronic and optical properties of atomically thin-layered ReS_2.

4.2. Sample preparation

Thin layer ReS_2 was prepared by mechanical exfoliation method, which has been described in section 3.1. Figure 4.1(a) shows an optical image of a 3L-ReS_2 after transferring on a quartz substrate. The 3L-ReS_2 has the same cleavage axis as the nearby bulk crystalline flakes. Consequently, the flakes break along the linear direction of the Re chain, defined as the crystal b-axis, due to the strong Re-Re bonds [137–139]. The triclinic structure shows an in-plane anisotropy along the b-axis. From the sharp fissures of few-layered and bulk flakes, the b-axis of ReS_2 is assigned along the blue line in the optical image. The assigned b-axis was also confirmed by the PL measurements, which will describe later.

4.3. Height profile, Raman and PL property of 3L-ReS_2 on quartz substrate

The layer number (three-layers) was characterized by AFM measurement, Raman scattering and PL spectroscopy. Figure 4.1(b) show the AFM image and its height profile in order to support the identification of layer numbers. The experimentally obtained height profile in Figure 4.1(b) shows that the thickness of measured ReS_2 is ~2 nm, which is consistent with the previously reported thickness of 3L. The Raman scattering spectra of 3L-ReS_2 were measured with a continuous wave semiconductor laser (2.33 eV). Figure

4.1(c) shows the Raman scattering spectrum of 3L-ReS$_2$. The several Raman scattering peaks originate from the low-symmetry anisotropic crystal structure of 3L-ReS$_2$. The rhenium and chalcogen atoms are forced into the same plane and, accordingly, induce in-plane and out-of-plane anisotropic lattice vibrations. In-plane vibrations of the A$_{1g}$ mode peak at 214 cm^{-1} and both the in-plane and out of-plane vibrations of the E$_{2g}$ mode peak at 153 cm^{-1} have been observed [29,132,138]. Figure 4.1(d) presents the PL spectrum of 3L-ReS$_2$ at room temperature. The PL peak at approximately 1.56 eV, accompanied by a weak shoulder at 1.62 eV. The inset of Figure 4.1(d) shows the layer number dependence of PL spectra at room temperature, which further supports that the number of layer is a three-layer for the investigated sample [29,140,141].

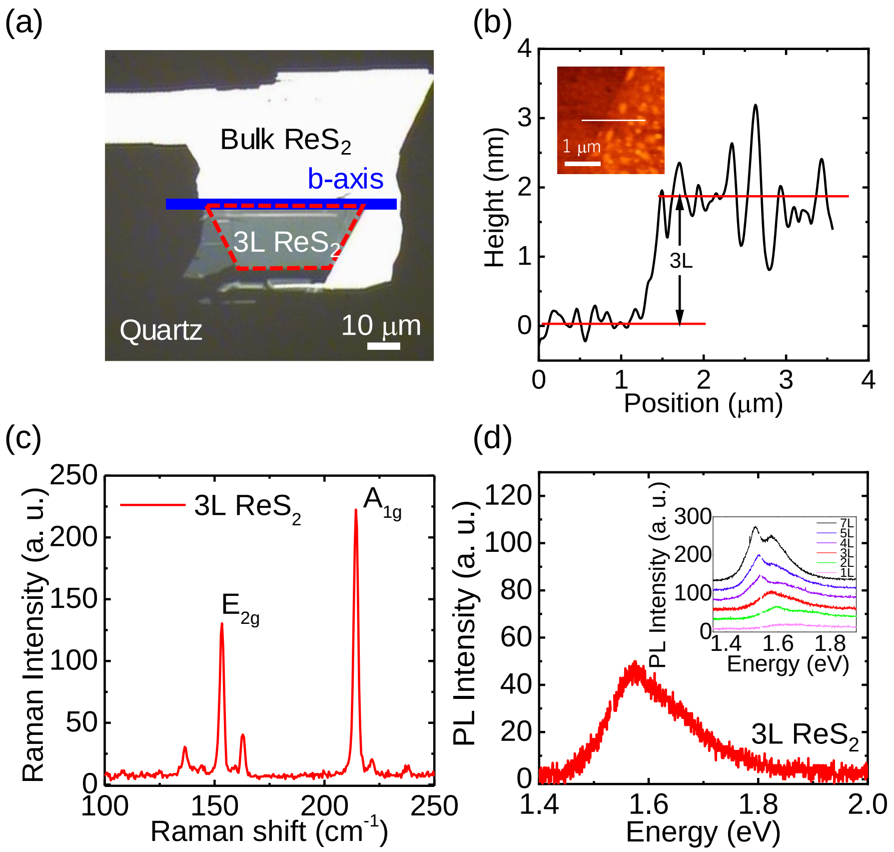

Figure 4.1 (a) Optical image of 3L-ReS$_2$ on the quartz substrate. The blue line indicates the direction of the Re chains (b-axis) of ReS$_2$. (b) Height profile along the white line of

3L-ReS_2 on Si substrate. Inset shows its atomic force microscopy (AFM) image with 1 μm scale bar. (c) Raman scattering spectrum and (d) PL spectrum of 3L-ReS_2 at room temperature. Inset of (d) shows the PL spectra of ReS_2 with different numbers of layers at room temperature. The red line is the spectrum of the 3L-ReS_2 studied in this thesis.

4.4. Polarization-resolved PL spectra

After identification for the layer number, polarization-resolved PL spectra at low temperature were measured, in order to confirm the polarization dependent optical properties, as shown in Figure 4.2(a). Two-peaks can be found at 1.58 and 1.62 eV in the spectra. The relative intensities of both peaks significantly alter with changing the excitation polarization angle (θ), where the polarization angle is defined by the relative angle from the b-axis of 3L-ReS_2. The PL intensity of lower energy peak at 1.58 eV shows the maximum intensity at excitation polarization angle (θ) of ~10°, while that of the higher energy peak at 1.62 eV exhibits the maximum at θ ~60°. The polarization-resolved PL spectra of 3L-ReS_2 are fitted by the Voigt functions to evaluate the polarization angle dependence of integrated PL intensities, and the detail of fitting results are shown in Figure 4.2(b). The spectrum was fit with Voigt functions for the X_1 (red line), X_2 (blue line) and indirect transition (green line) peaks.

Figure 4.2(c) shows the polar plot of integrated PL intensities of two peaks at 1.58 and 1.62 eV, as indicated by solid black circles and red squares. The both plots clearly show a double-lobed features, where the polarization angles at maximum integrated intensities are different, which is observed in the PL spectra in Figure 4.2(a). The data of polar plots are well reproduced by the PL intensity of lower energy peak at 1.58 eV showing the maximum value at about 10°, which is almost parallel to b-axis of ReS_2. The lower energy peak X_1 is assigned as PL from the confined excitons along the crystal direction of the rhenium atomic chains (b-axis), confirmed by the energy positions and polarization dependence of the intensity [33]. In contrast, the maximum intensity of higher energy peak X_2 is tilted as about 60° from the b-axis. The PL of higher energy peak comes from the the confined excitons along the crystal direction of the rhenium and sulfur atomic bonds [33]. The two different anisotropic excitons are confined by the reduced symmetry and anisotropic dielectric screening in the ReS_2.

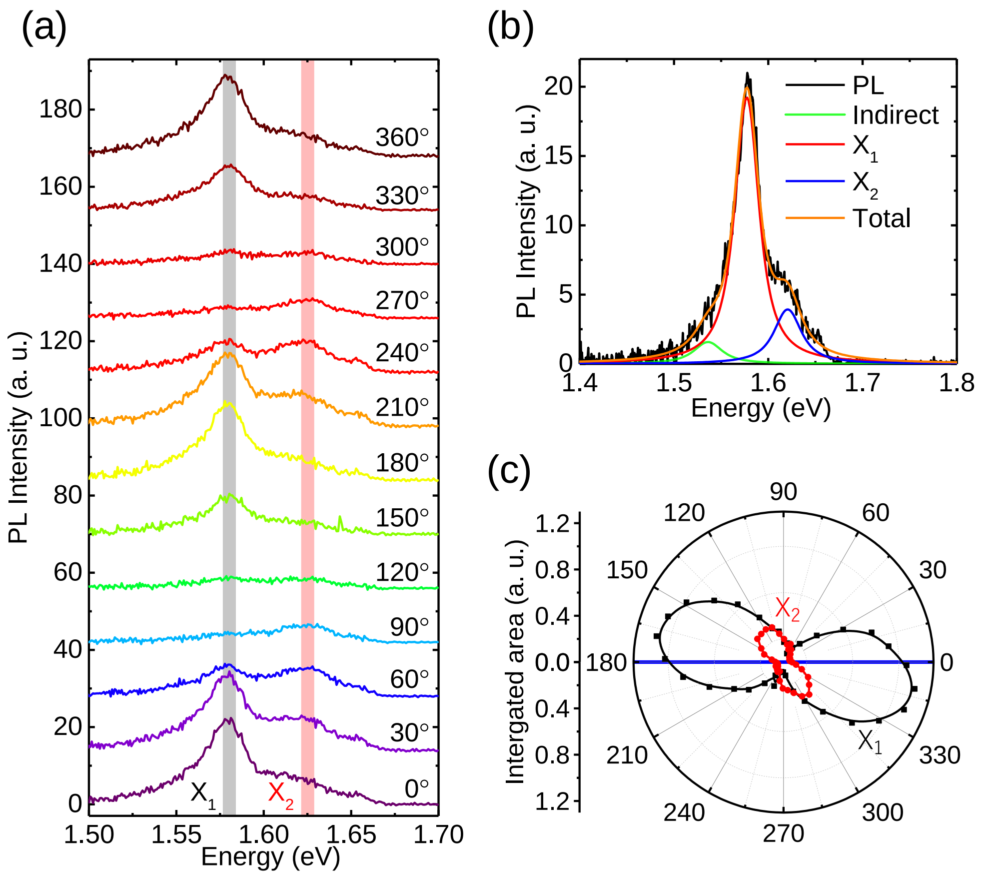

Figure 4.2 (a) PL spectra of 3L ReS_2 at different polarization angles (θ) of linearly polarized incident light (intervals = 30°) at 10 K, where θ is defined relative to the b-axis. The spectra are offset vertically for clarity. (b) and (c) Polar plot of the integrated PL

intensity of the X_1 and X_2 peaks at 10 K. Solid black circles and red squares plot the integrated PL intensities of the 1.58 (X_1) and 1.62 eV (X_2) peaks, respectively. The blue line indicates the direction of the b-axis.

4.5. Transient PL decay profiles

The polarization- and time-resolved PL measurements was conducted to investigate the dynamics of electron-hole pair in 3L-ReS_2 at 10 K. Figure 4.3(a) shows the time-resolved PL decay profiles measured at the excitation light polarization of parallel and perpendicular configuration to b-axis, and the instrumental response function (IRF) is also shown, as a black solid line. The profile of upper panel mainly attributed to the PL decay of X_1 peak exhibits a fast response, where the PL decay profile is almost identical to IRF.

Figure 4.3(b) indicates that the experimentally determined PL decay (red squares) and analysis by convolution of the instrumental response function (IRF) and a single exponential with different time constants (1-30 ps). The curves with time constants of 1, 5 and 10 ps fit the PL signal well, but those with larger time constants deviate from the data. Therefore, the PL decay time of X_1 peak is evaluated as less than 10 ps from the analysis of convolution procedure. Moreover, the profile in the lower panel from X_2 peak also shows the very fast decay profile as identical to IRF, and the evaluated PL decay time of X_2 peak is also less than 10 ps. The very fast PL decay times suggest that the recombination lifetime of electron-hole pair in the X_1 and X_2 transition is a very fast time scale of less than 10 ps.

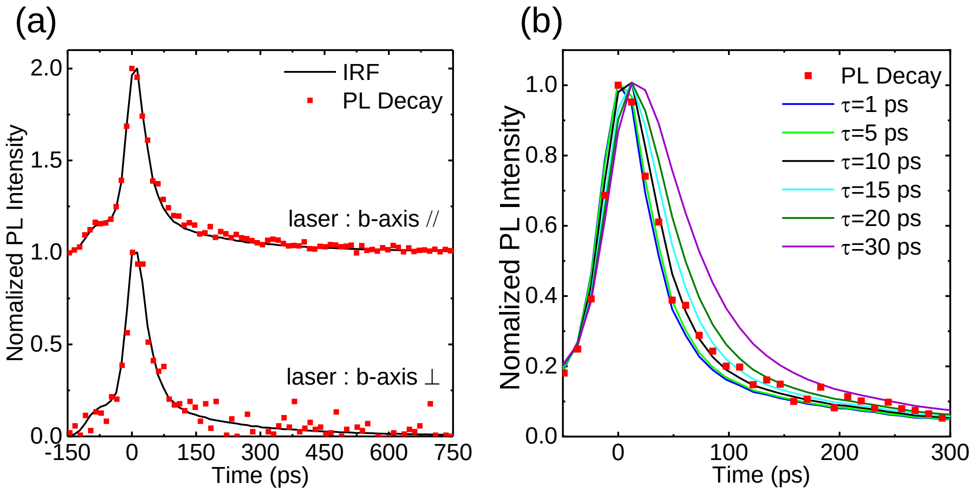

Figure 4.3 (a) Transient PL decay profiles at 10 K. The excitation light is polarized parallel and perpendicular to the b-axis at 10 K in the upper and lower panels, respectively. The black curves are the IRFs of the experimental setup. (b) Experimentally determined PL decay (red squares) and analysis by convolution of the IRF and a single exponential with different time constants (1-30 ps).

4.6. Decay profiles of transient differential reflectance spectra

The ultrafast optical dynamics of 3L-ReS_2 were investigated by polarization-resolved pump-probe spectroscopy. In pump-probe spectroscopy, the photoexcited electrons and/or holes, composed of excitons induced by the pump pulse, block the optical absorption (differential reflectivity) of the probe pulse due to the Pauli-exclusion principle (state-filling effect). The time evolution of transient pump-probe signals corresponds to the relaxation processes of photoexcited electrons and/or holes composed of excitons. Therefore, the optical absorption spectra arising from the exciton transition was investigated. Figure 4.4(a) shows the polarization-resolved differential reflectance $\delta R/R$ of 3L-ReS_2 on the quartz substrate at 10 K. The differential reflectance spectra on the polarization angle θ of 0, 45, 90 and 135° with linearly polarized light are shown. The differential reflectance spectrum of atomically thin few-layer material on the transparent substrate corresponds to the absorption spectrum. The two distinct peaks at 1.58 and 1.62 eV corresponding to X_1 and X_2 transition are clearly observed as similar to those of PL spectra in Figure 4.2(a). The X_1 and X_2 peak in the differential reflectance spectra show the strongest intensity at $\theta = 0°$ (parallel to b-axis) and = 45°, respectively, which is well consistent with the results observed in the polarization-resolved PL spectra in Figure 4.2(a).

Figure 4.4(b) shows 2D colour plot of the results of pump-probe spectroscopy, where vertical, horizontal axis and colour scale correspond to delay time between pump and probe pulse, probe photon energy, and differential reflectivity intensity $\Delta(\delta R/R)$ defined as the difference in the spectrum with and without the pump pulse with photon energy of 1.8 eV and power density of 120 μJ/cm^2, respectively, where the linear-polarizations of both pump and probe are parallel to b-axis. It shows the reflectivity change at 1.58 and 1.62 eV, corresponding to X_1 and X_2, respectively, after the arrival of the pump pulse. The differential reflectance spectra for a certain delay time can be obtained by horizontal cuts of the 2D plot as shown in Figure 4.4(c). The transient differential reflectance spectrum $\Delta(\delta R/R)$ at 1.58 eV corresponding to bleaching of peak X_1 has maximum at 0.3 ps and decaying on the time scale of 100 ps.

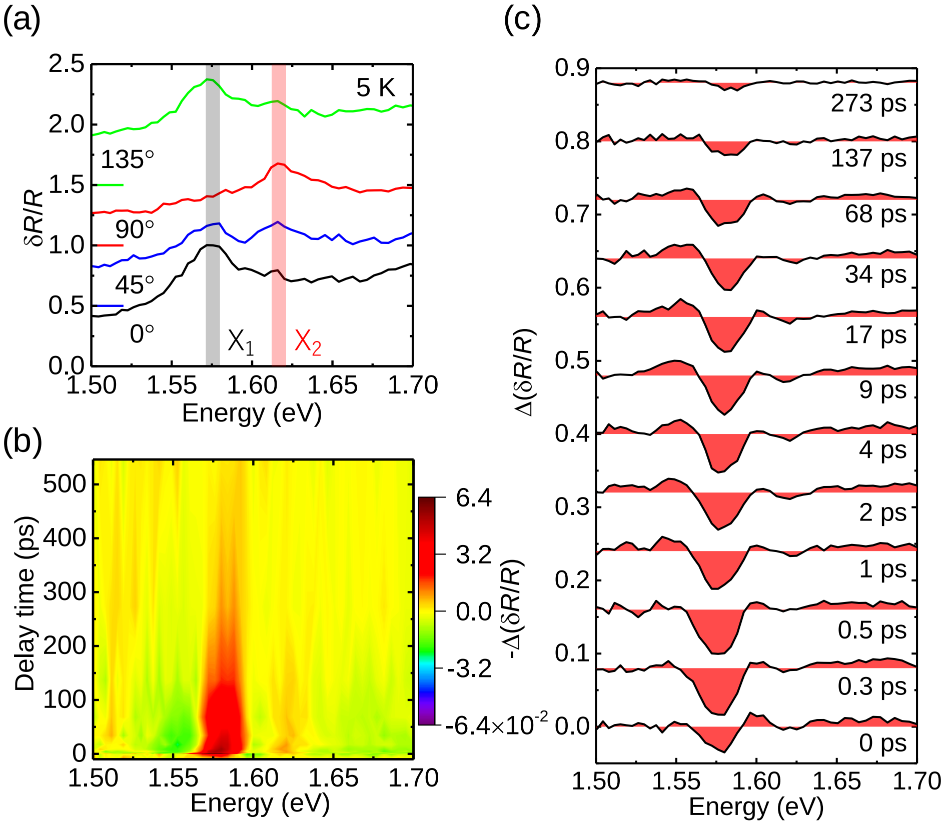

Figure 4.4 (a) Polarization-resolved differential reflectance of 3L-ReS_2 under four different polarization configurations at 5 K. The spectra are offset vertically for clarity (zero reflectance is indicated for each spectrum by the horizontal line). (b) 2D colour plot of the transient differential reflectance spectra of 3L-ReS_2 measured by the pump-probe method at 5 K. The pump and probe pulses are polarized parallel to the b-axis. The colour bar indicates the intensity of the transient differential reflectance signal. (c) Transient differential reflectance spectra with different delay times. The data are plotted with an offset.

The transient differential reflectance signal $\Delta(\delta R/R)$ monitored at 1.58 eV as a function of delay time after the arrival of pump pulse is plotted in Figure 4.5(a) and (b), where the pump and probe pulses are linearly polarized parallel to b-axis. The profile of

$\Delta(\delta R/R)$ in X_1 peak shows the multiple decay components, and well reproduced by the double exponential functions with decay times of 0.3 ± 0.04 and 116 ± 3 ps. The decay profiles of the transient differential reflectance under parallel polarization configurations fit by double exponential functions with the decay times, as shown in Figure 4.5(c). It is noted that the time-scale of slow component in X_1 peak is much different in the PL (< 10 ps), which will be discussed later in detail. The signal intensity of $\Delta(\delta R/R)$ with increasing the pump power density at 0.3 ps is plotted in the inset of Figure 4.5(a). The signal intensity of $\Delta(\delta R/R)$ changes linearly with the pump pulse intensity as indicated by the solid line, suggests that the bleaching signal comes from the Pauli blocking of the photogenerated carrier (electron and/or hole), not from multiple carriers such as Auger recombination and exciton-exciton annihilation process [142–145].

The time profiles in other three polarization experimental configurations are shown in Figure 4.5(d)-(e), where the polarization parallel to b-axis (//) and perpendicular to b-axis (⊥) are defined. In the configuration of pump (⊥) - probe (⊥), the profile of $\Delta(\delta R/R)$ mainly monitoring X_2 peak shows the multiple decay components, as similar to that in pump (//) - probe (//) in Figure 4.5(a). The profile of $\Delta(\delta R/R)$ of X_2 peak also shows the multiple decay components with decay times of 0.6 ± 0.08 and 118 ± 10 ps. The decay time constants of four alternative polarization configurations in the transient differential reflectance well fit by double exponential functions, as shown in Figure 4.5(f). Although the signal intensity on the transient differential reflectance changes depending on the pump and probe configuration, the decay profiles of X_1 and X_2 shows the same multiple components with decay times of ~1 and ~100 ps.

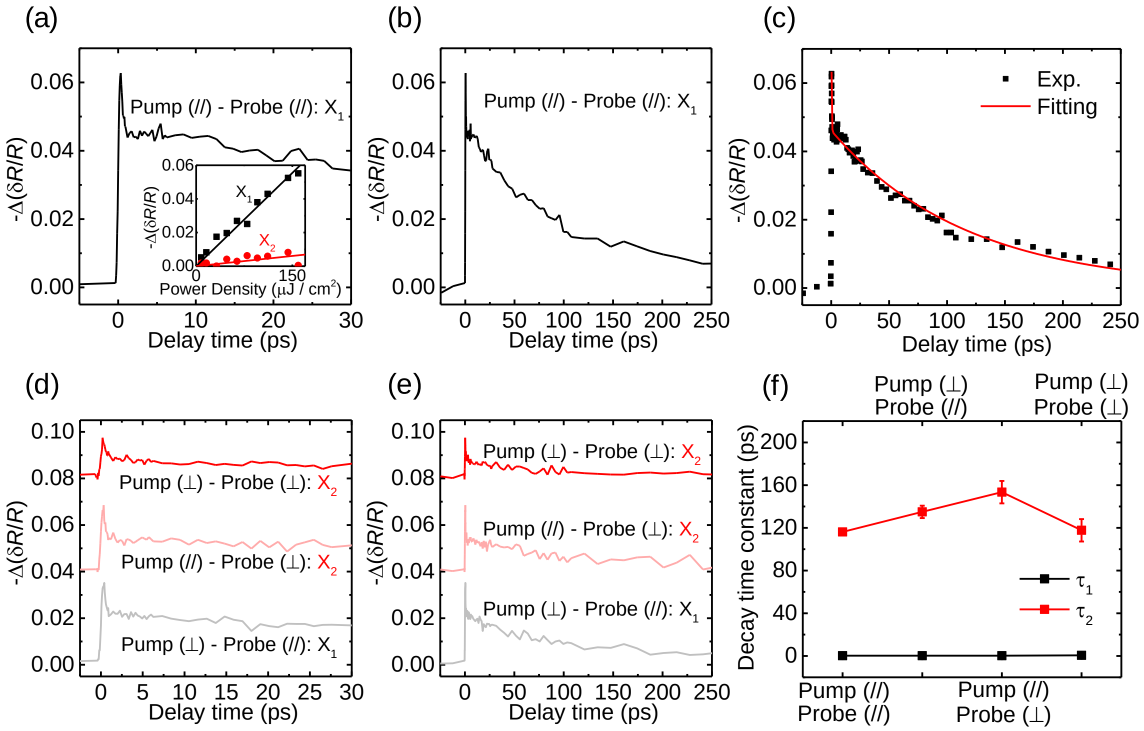

Figure 4.5 (a) and (b) Decay profiles of transient differential reflectance spectra of 3L-ReS$_2$ measured at 5 K. Inset of (a) shows the signal intensity of $\Delta(\delta R/R)$ at 0.3 ps versus the pump power density. (c) Decay profiles of transient differential reflectance under // pump–// probe polarization configurations fitting by double exponential functions with decay times. (d) and (e) Decay profiles of the transient differential reflectance under three polarization configurations, where the polarization is defined as parallel (//) or perpendicular (⊥) to the b-axis. The data are plotted with an offset. (f) Transient differential reflectance decay time constants of our alternative polarization configurations fitting by double exponential functions.

4.7. Carrier dynamics in 3L-ReS$_2$

According to the results of transient PL and pump-probe spectroscopy, the intra-band and inter-band photocarrier and exciton dynamics of 3L-ReS$_2$ can be elucidated. The time-scale on the transient differential reflectance (~100 ps) is much longer than that of the PL lifetime (< 10 ps), because the origins of signals between the pump and probe and PL spectroscopy are different, where the transient differential reflectance and PL signal monitor the populations of electron and/or hole, and electron-hole pair in the excited states, respectively. The different time-scale suggests the dissimilar intra-band and inter-band photocarrier dynamics. Figure 4.6(a) shows the schematic of energy band structure of 3L-ReS$_2$ around the conduction band minimum (CBM) and valence band maximum (VBM). The conduction band minimum is at Γ point, and valence band maximum at slightly displaced from Γ to X point in the momentum space, which suggests that the 3L ReS$_2$ is indirect band gap semiconductor with close direct band gap near Γ point. The band structure could strongly affect the intra-band and inter-band carrier dynamics in 3L-ReS$_2$, indicating the different time-scale observed in the transient differential reflectance and time-resolved PL measurement.

The conjectured intra-band and inter-band carrier dynamics from the experimental results are summarized in Figure 4.6(a) and (b). The electron and hole pair is generated in the optical excitation process by the photon energy of 1.8 eV. The optically generated electron and hole pair is relaxed to Γ point, within the time-scale of several hundred femtoseconds during the intra-band relaxation, based on the experimental results of fast rise of transient differential reflectance signal (< several hundred femtosecond) caused by the effect of phase-space filling. The fast recombination of electron and hole pair corresponding to X$_1$ and X$_2$ transition occurs, which can be monitored by the PL signals less than 10 ps. Then, the electron further relaxes to the minimum point of conduction band at X point nearby the Γ point during less than 10 ps, while the hole stays at the conduction band maximum at the Γ point. The electron and hole are at different position in momentum space. As a result, the PL signal due to the recombination of electron-hole pair at the Γ point quickly decays within less than 10 ps, as shown in Figure 4.6(a). In contrast, the transient differential signal due to the state filling persists on the order of 100 ps as far as the hole stays at the Γ point, because the X_1 and X_2 transition are prevented by the Pauli-blocking by the hole at the Γ point. Finally, the inter-band recombination of momentum mismatched electron-hole pair as indirect exciton composed of electron near the Γ point and hole at the Γ point could occur through the phonon emission process due to the momentum matching, and the indirect exciton slowly decays, as shown in Figure 4.6(b). The indirect recombination process could be observed in the time-resolved PL decay although the intensity is expected to be quite small.

In order to confirm the recombination process of the indirect exciton, the transient differential reflectance in various temperatures T was investigated. Figure 4.6(c) shows the time-evolutions of transient differential reflectance at X_1 peak from 5 to 230 K. The amplitude of signal on the transient differential reflectance decreases with increasing the temperature, because the peak of X_1 broadens with increasing the temperature. The profiles of transient differential reflectance on X_1 peak show the biexponential decay in the temperature range from 5 to 230 K, and the gradually changes with increasing the temperature. Figure 4.6(d) shows the evaluated slow lifetimes as a function of temperature. The slow decay constants gradually decrease with increasing the temperature. On the basis of the phonon-emission process, the decay rate γ corresponding to the recombination rate of indirect exciton should be given by:

$$\gamma(T) = \gamma_0(1+n) = \gamma_0\left(1+\exp\left(-\frac{E_{\mathrm{ph}}}{k_{\mathrm{B}}T}\right)\right) \ , \tag{4.1}$$

where k_{B} is Boltzmann constant, T is temperature, E_{ph} is a phonon energy and γ_0 is a temperature independent recombination rate. The temperature dependence of the phonon-emission process given in the eq. 4.1 is also shown in Figure 4.6(b) with red solid line assuming γ_0=(120 ps)$^{-1}$ with the phonon energy of 153 cm^{-1} in the Raman scattering spectrum in Figure 4.1(b), which well reproduces the tendency of experimental result of temperature dependence of decay time. The experimental results support the phonon-assisted recombination of indirect exciton in 3L-ReS$_2$.

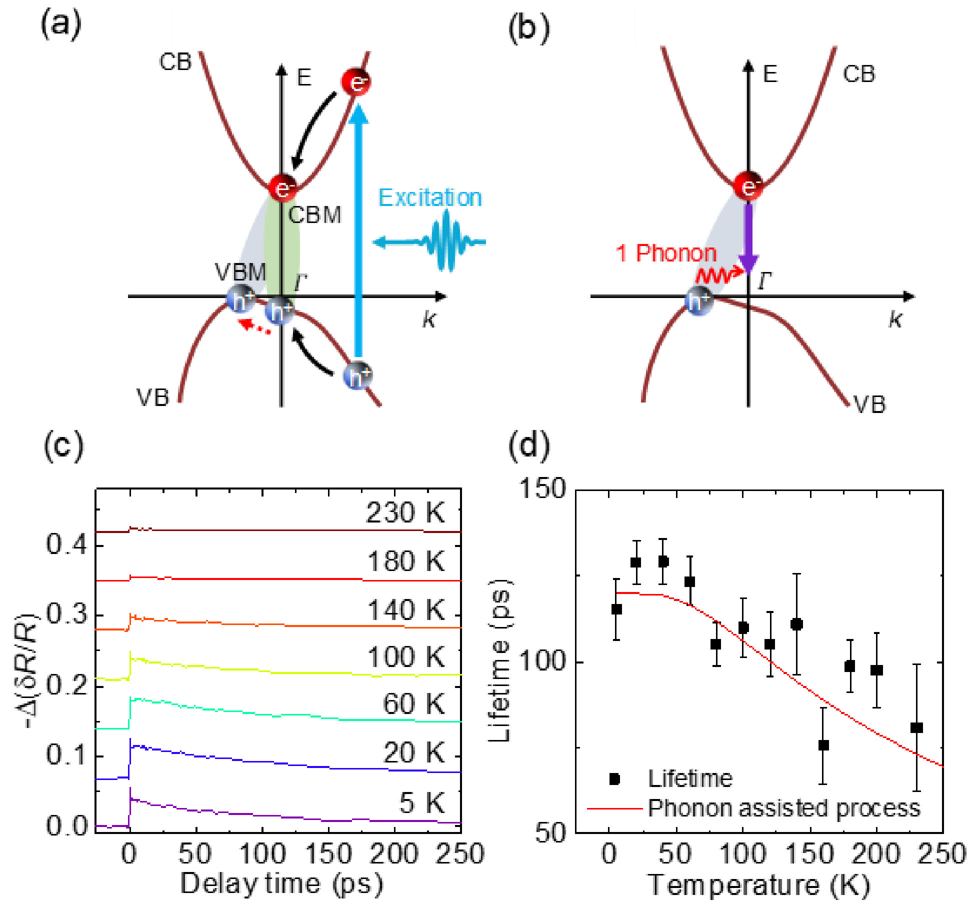

Figure 4.6 (a) Schematic of the energy band structure of 3L-ReS$_2$ and intra-band dynamics. The photocarrier relaxation dynamics are shown at the initial stage of

photoexcitation. The green and blue shades represent the formation of direct excitons at the Γ point and indirect excitons, respectively. (b) Schematic of inter-band photocarrier dynamics at the late stage, when the electrons and holes relax to different points in momentum space. (c) Decay profiles of transient differential reflectance monitored at the X_1 peak of 3L-ReS_2 at different temperatures (5-230 K). The data are plotted with an offset. (d) Evaluated lifetime of the slow component in the decay of the transient differential reflectance, plotted as a function of temperature. The solid line is the plot of eq. 4.1 based on the one-phonon emission process.

4.8. Chapter Summary

In this chapter, I described the intra-band and inter-band photocarrier dynamics of 3L-ReS_2 by polarization-resolved transient PL and ultrafast pump-probe spectroscopy. The polarization-resolved PL spectra show the two-peaks (X_1 and X_2) from recombination of excitons confined along the crystal direction of the rhenium-sulfur, and rhenium-rhenium atomic bonds due to its 1*T* distorted crystal structure of ReS_2. The decay profiles of X_1 and X_2 peak clearly shows the different time-scales in the time-resolved PL (<10 ps) and the transient differential reflectance (~100 ps), with monitoring the populations of electron-hole pair, and electron and/or hole in the excited states, respectively. The characteristic intra- and inter-band carrier dynamics of rapid electron relaxation and recombination process of momentum mismatched exciton with accompanied by the phonon emission are revealed. Our findings provide important information regarding the indirect band gap nature of few layers ReS_2 and characteristic carrier dynamics, which leads to understand the novel electronic and optical properties of ReS_2 atomically-thin layered materials.

Chapter 5. Radiative lifetime and dynamics of trion in ReS_2

In chapter 5, I will describe the exciton and trion dynamics of few layered ReS_2. From this chapter, I will introduce the optical properties of thin layer ReS_2 FET structure under the controllable conditions of carrier density by external gate voltage, which could enable to identify the negatively charged excitons (negative trions).

5.1. Introduction

As mentioned in chapter 2 and 4, since the discovery of atomically thin black phosphorous (back phosphorene), the atomically thin 2D materials with anisotropic crystal structures such as GeX (X=S, Se) [146], SnX (X=S, Se) [147], and so on have been intensively studied as new research directions of 2D materials. Such an atomically thin 2D materials exhibit the anisotropic carrier transport and optical properties due to the anisotropic electronic structures, which provides the novel characteristics of linear dichroism [148,149], valley selective excitation by linearly polarized light [150] and polarization sensitive photodetectors from the viewpoints of optical physics [151,152] and device applications [153–155]. Be contrary to isotropic 1*H* structure MX_2, ReS_2 is a layered material with reduced symmetry because of the weak interlayer coupling from distorted 1*T* structure [29], which imparts highly anisotropic optical absorption and PL spectra [156–158]. Moreover, the field effect transistor with highly anisotropic carrier transport, polarization sensitive photodetectors have been demonstrated [136,159–162].

Optically excited bound electron-hole pairs (neutral excitons) confined in atomically thin materials are formed due to strong Coulomb interaction play important roles in the optical response of atomically thin 2D MX_2 with isotropic crystal structures [163–166]. The three-particle bound states of charged excitons (trions) with a charge degree of freedom also plays an important role in the optical response in the intentionally and unintentionally doped atomically thin 2D MX_2 [167,168]. The experimentally observed trions in the atomically thin monolayer 2D transistion metal dichalcogenides, MX_2 with isotropic crystal structure have been intensively studied [166,169–176]. However, the trions in atomically thin 2D materials with an anisotropic crystal structure, have not been fully understood.

In this chapter, I will introduce negatively charged excitons (negative trions) in few-layer ReS_2 with field effect transistor (FET) structures. The emerging new PL peak below the lower energy side of neutral excitons is attributed to negative trions by tuning the gate voltages. In addition, the dynamics and radiative lifetime of negative trion in a few-layer ReS_2 investigated by temperature dependence of PL spectroscopy and phenomenological rate-equation analysis will also be discussed.

5.2. Sample preparation

The atomically thin layers ReS_2 with thickness of three layer (3L) with back-gate FET structures were fabricated by dry-transfer process onto the Cr/Au electrodes, which has been described in Chapter 3.2. The optical image of typical 3L-ReS_2 FET is shown in Figure 5.1(a). The cleavage axis (Re-Re bond) corresponding to b-axis during mechanical exfoliation [157,158], which has been described in Chapter 4.1. From the sharp fissures of three-layered flakes, the b-axis of ReS_2 is assigned along the red dash line in the optical image. The distance between two electrodes keeps about 10 μm, which is suitable for the optical measurement.

5.3. Raman and PL property of 3L-ReS_2 on Si substrate

Figure 5.1(b) shows Raman scattering spectrum of 3L-ReS_2 on the Si substrate. The in-planes vibration peaks at 153.4 cm^{-1} and 139.4 cm^{-1} were observed and the frequency difference of 14 cm^{-1}, which indicate an isotropic AB-stacking characteristic of three layer [177], as described in chapter 4.8. The PL spectrum was also measured to further confirm the layer number. The main PL peak can be observed at approximately 1.56 eV with a weak shoulder at 1.62 eV. Both Raman scattering and PL spectra are well consistent with the results in chapter 4.2 and previously reported papers [157].

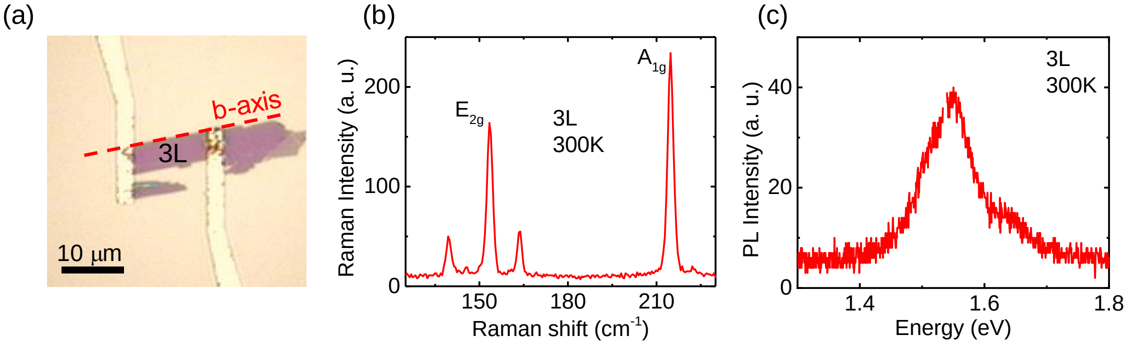

Figure 5.1 (a) Optical microscopy image of 3L-ReS_2 with an FET structure using the Cr/Au electrodes on a SiO_2/Si substrate. The red line indicates the direction of the Re-Re chains (*b*-axis) of ReS_2. (b) Raman scattering spectrum of 3L-ReS_2. (c) PL spectrum of 3L-ReS_2 at room temperature.

5.4. Observation of trion in ReS$_2$

Figure 5.2(a) shows the 2D color plot of PL spectra in 3L-ReS$_2$ as a function of gate voltage at 20 K. The 2D color plot clearly displays the change of PL spectra depending on the gate voltage. Figure 5.2(b) shows the PL spectra obtained from the 2D color plot at different gate voltages. In larger negative gate voltage region (-45 V), the sharp emission peaks around 1.58 (X$_1$) and 1.62 eV (X$_2$) are clearly observed. With the positive gate voltage (> 0 V), new peak emerges at 1.56 eV at lower side of the X$_1$. With increasing the gate voltage from -45 to 45 V, the new peak at 1.56 eV increases, while the emission peak of X$_1$ at 1.58 eV and X$_2$ at 1.62 eV decreases. The gate-voltage dependence of PL spectra suggests that the new shoulder at 1.56 eV originates from negative trion (X$_1^-$) by the X$_1$ capturing injected electron above the positive gate-voltage (> 0 V). The broad peak around 1.7 eV is probably due to higher-series excitonic transitions, corresponding to Re 5d t_{2g} to Re 5d t_{2g}^* hybrid with chalcogen X (S, Se) p^* antibonding states [178].

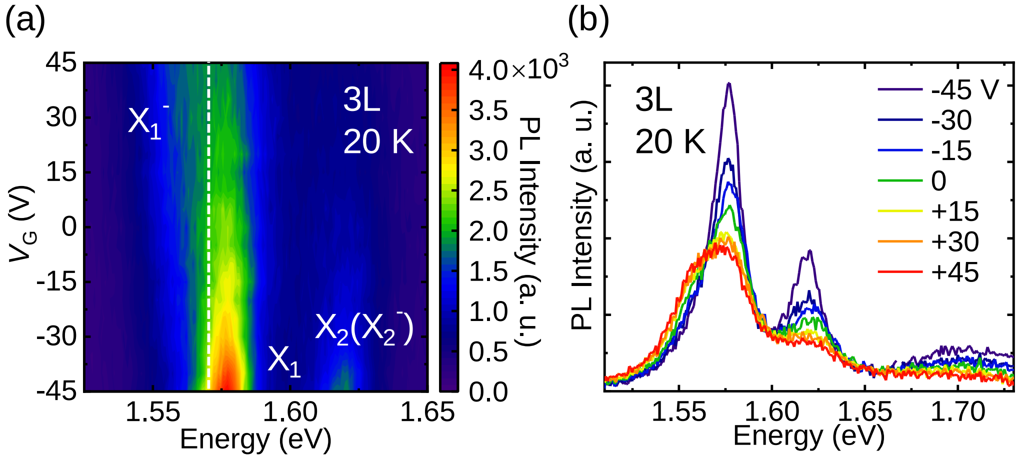

Figure 5.2 (a) 2D contour plot of PL spectra in 3L-ReS$_2$ FET device as a function of back gate voltage at 20 K. The excitation polarization direction is fixed at 45° with respect to *b*-axis of ReS$_2$. (b) PL spectra of 3L-ReS$_2$ under various back gate-voltages. The emission peaks at 1.56 and 1.58 eV are denoted as X$_1^-$ and X$_1$, 1.61 and 1.62 eV are denoted as X$_2^-$

and X_2.

In order to analyze the gate-voltage dependent PL spectral change, the spectral fitting of 3L-ReS_2 at 20 K were conducted with multiple peaks assuming Voigt functions. Figure 5.3(a) shows the PL spectrum at the gate-voltage of +20 V and fitted results with five-components of X_1^- (1.56 eV, red), X_1 (1.58 eV, green), X_2^- (1.62 eV, blue), X_2 (1.63 eV, cyan) and X* (1.7 eV, magenta). The total fitted results (yellow) well reproduced the experimentally obtained PL spectrum. Figure 5.3(b) shows the PL spectra and fitted results at various gate voltages. With increasing the gate voltage from -45 V, the intensity of X_1^- increases, while the intensity of X_1 gradually decreases. Noted that the gate voltage dependent PL changes are strongly anti-correlated between X_1^- and X_1. The increasing of X_1^- intensity with a function of back-gate voltage (carrier density) suggests that the X_1^- come from the emission of a negatively charged exciton (negative trion) in atomically thin anisotropic ReS_2, which will be discussed in the next chapter.

The changes of trion/exciton ratio are strongly correlated to the electrical properties of ReS_2. The stronger X_1 emission peak below -20 V in the intrinsic low-carrier density region suggests that the X_1 peak in the spectra comes from the recombination of neutral bound electron-hole pair (exciton). In contrast, the emerging X_1^- peak above -20 V in *n*-doped region with high electron density is attributed to emission from charged bound state of a couple of electrons-hole (negatively charged exciton, negative trion). The injected electrons by the positive gate-voltage induce the spectral weight transfer of excitons to that of negative trions because of the trion formation. To further prove this, detail studies will be described in chapter 6.

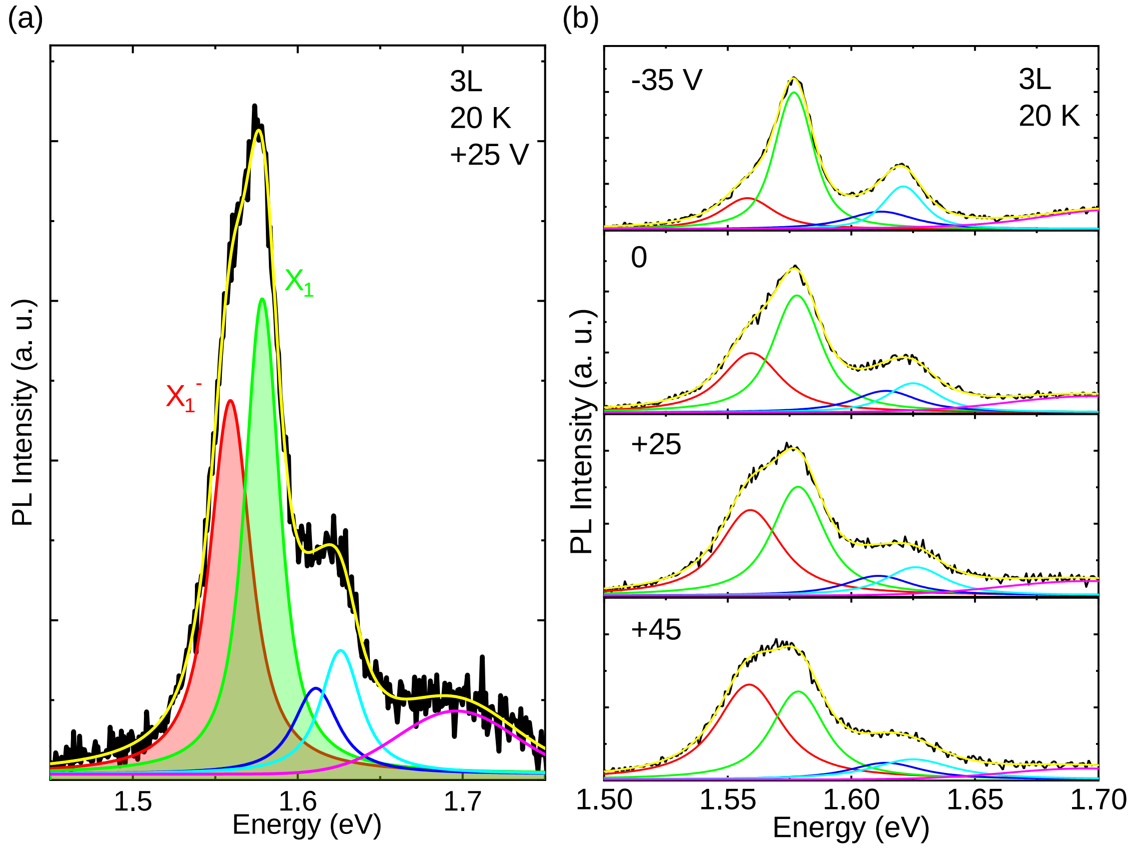

Figure 5.3 (a) PL spectra of 3L-ReS_2 at 20 K, with applying the gate-voltage of +25 V (black curve). The Voigt function fitting curves are indicated: red and blue shade curve is negative trion (X_1^- and X_2^-), green and cyan shade are natural excitons (X_1 and X_2), and magenta curve is higher-series exciton. The total of Voigt function fitting curves with five peak components is also shown. (b) PL spectra with an applied gate-voltage of -35, 0, +25 and +45 V. The Voigt function fitting curves are indicated.

5.5. Temperature dependence of PL

The temperature dependence of PL spectra was investigated in order to reveal the trion dynamics in ReS_2. Figure 5.4(a) shows the counter maps of temperature-dependent PL spectra of 3L-ReS_2 from 10 to 250 K under the back-gate voltage (V_G) of +45 V (doped carrier density of n_e=7.5×10^{12} cm^{-2}), where the linear polarization plane of the excitation laser was set as parallel direction of b-axis in ReS_2. The gradually shift to lower energy side and broadening of PL peak around 1.57 eV are experimentally observed with increasing temperature due to the bandgap shrinkage, which is well consistent with the previously reported results of 1L-MX_2 [179–181].

The PL spectrum of 3L-ReS_2 at 10 K were analyzed by using multiple Voigt functions, which has been also described in section 5.4. In Figure 5.4 (b), the main and subsequent PL peaks are assigned from the neutral exciton (X_1) and trions (charged exciton X_1^-) at 1.57 and 1.55 eV with a parallel direction to b-axis, and X_2 and X_2^- with a perpendicular direction to b-axis around 1.63 eV. The totally fitted result indicated by a yellow line accurately well reproduces the experimentally obtained PL spectrum. The fitted results are well consistent with those in the gate-dependent PL spectroscopy.

Figure 5.4(c) shows the PL spectra of 3L-ReS_2 from 10 to 200 K at a gate voltage of +45 V. The PL intensity drastically decreases and spectral shape significantly changes depending on temperature. The PL spectra were also fitted by the same procedures as shown in Figure 5.4(b) and all the spectra were well reproduced by the fitted results. The detail temperature dependence of energy positions, linewidth and PL intensity of each peak, will be discussed after.

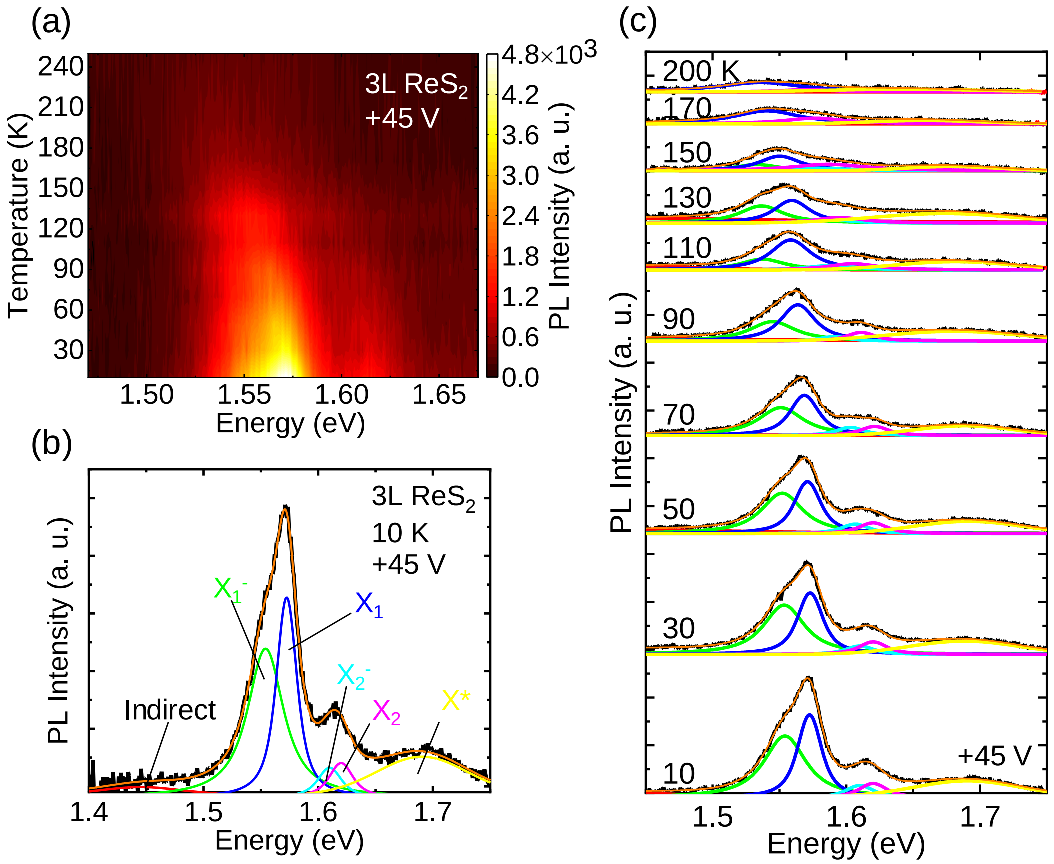

Figure 5.4 (a) Contour plot of the PL spectra in field effect transistor structure of 3L-ReS$_2$ as a function of temperature at back-gate voltage of +45 V. (b) PL spectra of 3L-ReS$_2$ at 10 K with an applied gate voltage of +45 V (black curve). The Voigt function fitting curves are presented as follows: the green and cyan curve denote the emissions from the negative trion (X_1^- and X_2^-), the blue and magenta curve are the neutral excitons (X_1 and X_2), and the red and yellow curve are indirect exciton and a higher-series exciton (X*). The total of Voigt function fitting curves is also depicted (yellow curve). (c) Temperature dependence of PL spectra for 3L-ReS$_2$ from 10 to 200 K at the back-gate voltage of +45 V. The fitted curves containing each peak components using Voigt functions are also shown.

Figure 5.5(a) shows the energy positions of exciton X_1 (red circles) and trion X_1^- (black circles) as a function of temperature from the analysis of Figure 5.4 (c). Both X_1 and X_1^- peaks gradually shift to lower energy side with an increasing in temperature from 10 to 200 K. The temperature dependence of both peak shifts are fitted by empirical Varshini equation as follows [182]:

$$E_{\mathrm{X}_1(\mathrm{X}_1^-)}(T) = E_{\mathrm{X}_1(\mathrm{X}_1^-)}(0) - \frac{\alpha T^2}{T + \beta} \ , \tag{5.1}$$

where T is the temperature, α and β are parameters, and $E_{\mathrm{X}_1(\mathrm{X}_1^-)}(0)$ is the spectral energy position of the exciton (trion) at the zero temperature limit. As shown by the solid lines in Figure 5.5(a), the temperature dependence of the shifts for both X_1 and X_1^- is well reproduced by using eq. 5.1. The values for $E_{\mathrm{X}_1(\mathrm{X}_1^-)}(0)$ of 1.57 and 1.55 eV are obtained for the exciton and trion peaks, respectively, and α and β are commonly determined to be 3×10^{-4} eV/K and 197 K, for X_1 and X_1^- [183]. The Varshini equation could effectively describe the temperature dependence of band gap shifts in semiconductors including TMDs. The well-reproduced temperature dependence of the exciton and trion energies using the Varshini equation indicates that the energy of the exciton and trion peaks shift are determined by the temperature dependent bandgap shift of ReS_2. About ~20 meV energy difference (ΔE) between X_1 and X_1^- can be observed, which is dominated mainly by the binding energy of the trion, and very small contribution of the increase in Fermi energy from the bottom of the conduction band by the doped electrons [49]. Sphere plot in Figure 5.5 (a) is experimental fitting result from Figure 5.4 (c), which also keeps a consistent value of ~20 meV from 10 to 170 K. This result is well consistent with the previous results of other MX_2 such as WSe_2 [184] and $MoTe_2$ [181].

Figure 5.5(b) shows temperature dependence of intrinsic linewidth of X_1 and X_1^-. The linewidth defined as the half maximum (FWHM) of Lorentzian component in the fitted Voigt function with consideration of a constant Gaussian linewidth of 11 meV, which is the most suitable value for fitting. Noted that the intrinsic linewidth corresponding to homogeneous linewidth for both exciton and trion at the lowest temperature of ~10 K shows the larger values than those in typical 1L-MX_2 [185,186]. The broader homogeneous linewidth suggests faster relaxation paths of the exciton (X) and trion (X^-) towards the lower indirect exciton states of ReS_2 [156,187].

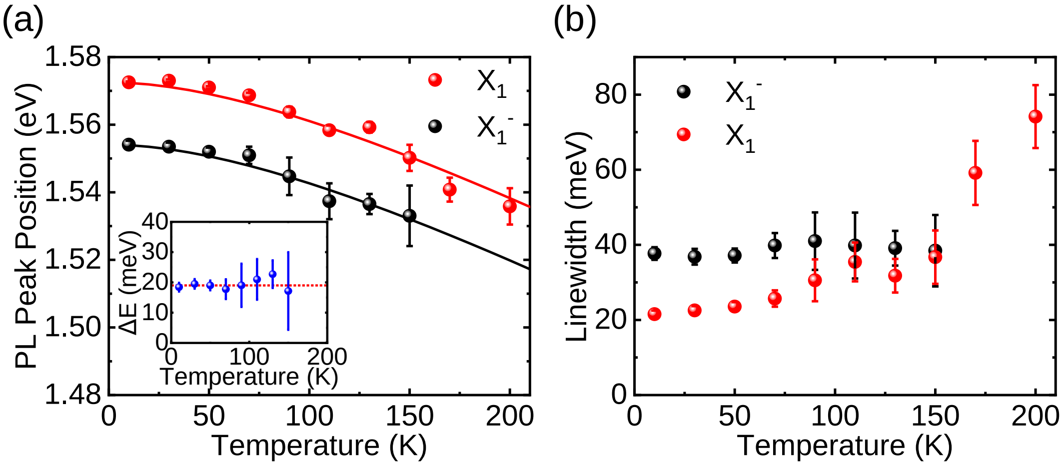

Figure 5.5 (a) Temperature dependence of PL peak position from exciton (red squares) and trion recombination (black circles) from 10 to 200 K at the back-gate voltage of +45 V. (b) Linewidth of exciton and trion PL peak as a function of temperature.

5.6. Radiative lifetime of trion

The formation dynamics of trion and temperature dependence of its radiative lifetime will be discussed from the temperature dependence of PL spectroscopy in this section. Figure 5.6(a) shows the integrated PL intensity of exciton and trion as a function of temperature. The integrated PL intensities of both exciton and trion decrease with an increase of temperature under a back gate voltage of +45V. The temperature dependence of PL intensity ratio ($I_{X_1^-}/I_{X_1}$, blue circles) was also shown in Figure 5.6(b), which suggests that the PL intensity ratio gradually decreases with increasing the temperature.

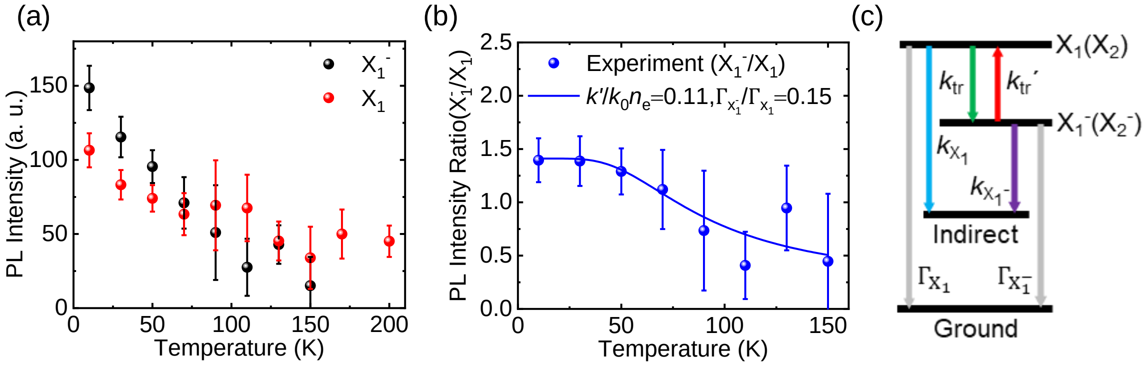

Figure 5.6 (a) Temperature dependence of exciton (red) and trion (black) PL intensity in 3L–ReS$_2$ from 10 to 200 K at the back-gate voltage of +45 V. (b) PL intensity ratio of trion and exciton as a function of temperature. The fitted result using eq. 5.6 is also shown as a solid line. (c) Four-level model including of exciton, trion, indirect and ground state.

Four-level system is used to describe the mechanism with the lowest exciton (X_1), trion (X_1^-), indirect exciton and ground state (g) states, in order to clarify the exciton and trion dynamics, as shown in Figure 5.6 (c). The energy difference between X_1 and X_2 is about 50 meV, which is much larger than the energy scale of thermal energy. Thus, the dynamics between X_1 and X_2 could be neglected in the analysis. The time evolution of populations of exciton (N_{X_1}) and trion ($N_{X_1^-}$) in the four-level model for calculating the PL intensity ratio ($I_{X_1^-}/I_{X_1}$) can be described as follows:

$$\frac{dN_{X_1}}{dt} = G - k_{X_1}N_{X_1} - k_{tr}N_{X_1} - \Gamma_{X_1}N_{X_1} + k'_{tr}N_{X_1^-} \ , \tag{5.2}$$

$$\frac{dN_{X_1^-}}{dt} = -k_{X_1^-}N_{X_1^-} - \Gamma_{X_1^-}N_{X_1^-} + k_{tr}N_{X_1} - k'_{tr}N_{X_1^-} \ , \tag{5.3}$$

where G is optical generation rate of initial exciton, $\Gamma_{\mathrm{X_1(X_1^-)}}$ and $k_{\mathrm{X_1(X_1^-)}}$ are the radiative and non-radiative decay rate of exciton or trion, and k_{tr} (k'_{tr}) is a formation rate of trion from the exciton through one-phonon emission (dissociation rate of trion through one-phonon absorption) process. The populations of excitons and trions derived from the steady-state solutions of coupled rate equations described above are expressed as follows:

$$N_{\mathrm{X_1}} = \frac{G \cdot \left(k_{\mathrm{X_1^-}} + \Gamma_{\mathrm{X_1^-}} + k'_{\mathrm{tr}}\right)}{\left(k_{\mathrm{X_1}} + \Gamma_{\mathrm{X_1}} + k_{\mathrm{tr}}\right)\left(k_{\mathrm{X_1^-}} + \Gamma_{\mathrm{X_1^-}} + k'_{\mathrm{tr}}\right) - k'_{\mathrm{tr}}k_{\mathrm{tr}}} \ , \tag{5.4}$$

$$N_{\mathrm{X_1^-}} = \frac{G \cdot k_{\mathrm{tr}}}{\left(k_{\mathrm{X_1}} + \Gamma_{\mathrm{X_1}} + k_{\mathrm{tr}}\right)\left(k_{\mathrm{X_1^-}} + \Gamma_{\mathrm{X_1^-}} + k'_{\mathrm{tr}}\right) - k'_{\mathrm{tr}}k_{\mathrm{tr}}} \ , \tag{5.5}$$

The formation rate from exciton to trion state can be denoted as $k_{\mathrm{tr}} = k_0 n_{\mathrm{e}}(1 + \langle n_{\mathrm{ph}} \rangle)$, and dissociation rate from trion to exciton rate can be denoted as $k'_{\mathrm{tr}} = k_0 n_{\mathrm{e}} \langle n_{\mathrm{ph}} \rangle$. In these equations, n_{e} is the doped carrier density, k_0 is the transition rate between exciton and trion at low carrier density limit. $\langle n_{\mathrm{ph}} \rangle$ is the phonon occupation number, which can be described as $\langle n_{\mathrm{ph}} \rangle = 1/\{\exp(\Delta E/k_{\mathrm{B}}T) - 1\}$. ΔE (≈20 meV) is the energy difference of exciton and trion states, which is almost similar to near the energy of E_{2g} mode with in-plane Raman vibration peaks at 153.4 $\mathrm{cm^{-1}}$ as shown in Figure 5.1(b). The E_{2g} phonon mode would contribute to the dynamics between exciton and trion states. The PL intensity of exciton (trion) is calculated as $I_{\mathrm{X_1(X_1^-)}} \propto \Gamma_{\mathrm{X_1(X_1^-)}} \cdot N_{\mathrm{X_1(X_1^-)}}$. As a consequence, the PL intensity ratio $I_{\mathrm{X_1^-}}/I_{\mathrm{X_1}}$ can be approximately described as:

$$\frac{I_{\mathrm{X}_1^-}}{I_{\mathrm{X}_1}} = \frac{\Gamma_{\mathrm{X}_1^-}}{\Gamma_{\mathrm{X}_1}} \times \frac{\exp\left(\frac{\mathit{\Delta} E}{k_{\mathrm{B}}T}\right)}{\left\{\exp\left(\frac{\mathit{\Delta} E}{k_{\mathrm{B}}T}\right) - 1\right\}\frac{k'}{k_0 n_{\mathrm{e}}} + 1}\ , \tag{5.6}$$

which is origin from the PL intensity ratio $I_{\mathrm{X}_1^-}/I_{\mathrm{X}_1}$ using eq. (5.4) and (5.5). ΔE (≈20 meV) is the trion binding energy obtained from the fitting procedures in Figure 5.5(a), T is the experimental temperature and k' $(= k_{\mathrm{X}_1^-} + \Gamma_{\mathrm{X}_1^-})$ is trion decay rate, with including the non-radiative and radiative decay rate process. Moreover, the temperature dependent radiative decay rate of exciton as $\Gamma_{\mathrm{X}_1} = (1/4T)$ $(\mathrm{ps})^{-1}$ is used [188], and has a constant value at =0.11. The calculated curve using eq. (5.6) are well reproduced the experimental results, as shown in Figure 5.6(b).

Temperature dependence of PL decay of trions monitored at 1.55~1.53 eV from 10 to 200 K with consideration of energy position shift of trion X_1^- (Figure 5.5(a)) was measured in order to infer the temperature independent parameter of k'/k_0n_{e}, as shown in Figure 5.7(a). There are two types of doped carriers, injected carriers by the gate-bias and impurity carriers generated from donor (accepter level). At the experimental condition of bias-voltage of 45 V, the number density of temperature independent injected carriers by the gate-bias voltage is much larger than temperature dependent those from impurity carriers.

The decay profiles show the similar response of instrumental response function (IRF) in the whole temperature range. The decay rates of trions k' are evaluated as larger than 0.1 $(\mathrm{ps})^{-1}$ from the analysis of convolution procedures. Experimentally determined PL decay at 10 K and analysis by convolution of the IRF and a single exponential function with different time constants was shown in Figure 5.7(b). Moreover, we assumed the typical formation rate of trion k_0n_{e} of less than ~1 $(\mathrm{ps})^{-1}$ at low temperature as reported in

Ref. [189]. The derived k'/k_0n_e (=0.11) as a parameter is consistent with the value used in the fitted curve as shown in Figure 5.6 (b). The comparison with the experimental and calculated results of PL intensity ratio derives the value of $\Gamma_{X_1^-}/\Gamma_{X_1}$ (=0.15). To support the fitting result, Figure 5.8 represent the fitted curves with various parameter to show the validity of analysis physically. Figure 5.8(a) shows variable parameter set of k'/k_0n_e with fixing the value of $\Gamma_{X_1^-}/\Gamma_{X_1}$ (=0.15) and Figure 5.8(b) shows variable parameter set of $\Gamma_{X_1^-}/\Gamma_{X_1}$ with fixing the value of k'/k_0n_e (=0.11). From this, fitting result at k'/k_0n_e (=0.11) and $\Gamma_{X_1^-}/\Gamma_{X_1}$ (=0.15) are most suitable value with the experiment result.

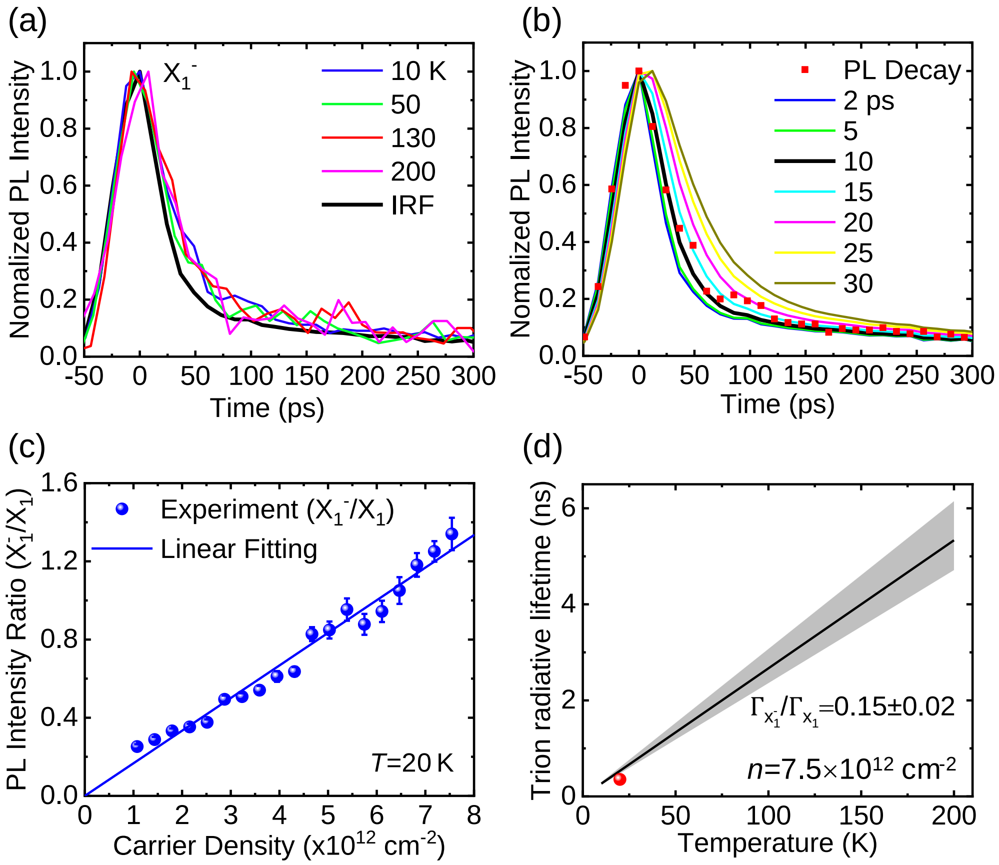

Figure 5.7 (a) PL decay profiles of X^- from 10-200 K. The black curves are the IRFs of the experimental setup. (b) Experimentally determined PL decay at 10 K (red squares), and analysis by convolution of the IRF and a single exponential function with different time constants (2–30 ps). (c) Integrated PL intensity ratio of X_1^- and X_1 peaks as a

function of carrier density. The solid line corresponds to the fitted line obtained by using the least-square fitting procedure. (d) Temperature dependence of derived radiative lifetime of trions. The red circle was experimentally obtained trion radiative lifetime at 20 K from Figure 5.7(c) and eq. 5.7.

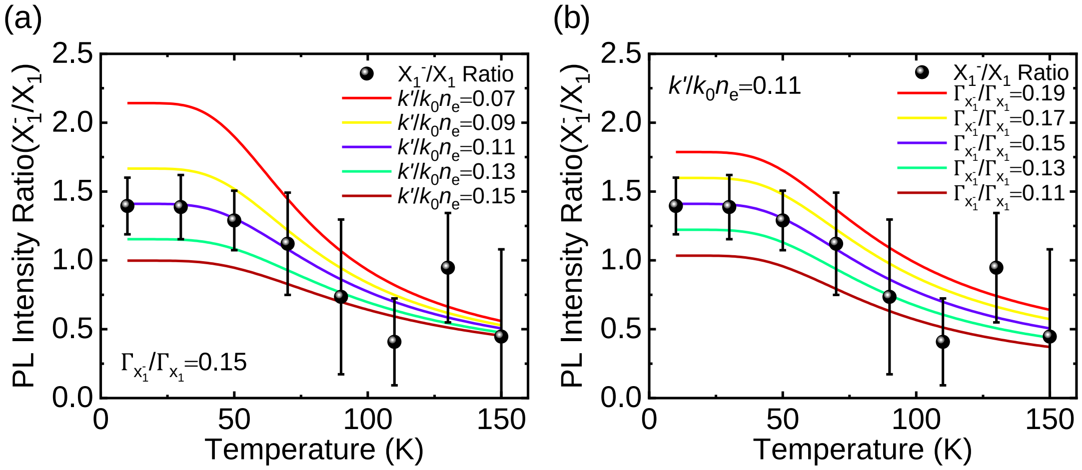

Figure 5.8 Calculated PL intensity ratio of trion and exciton as a function of temperature with various parameters. (a) Variable parameter set of k'/k_0n_e with fixing the value of $\Gamma_{X_1^-}/\Gamma_{X_1}$ (=0.15). (b) Variable parameter set of $\Gamma_{X_1^-}/\Gamma_{X_1}$ with fixing the value of k'/k_0n_e (=0.11).

The PL intensity ratio of exciton and trion as a function of carrier density (back-gate voltage) at 20 K is also analyzed by using eq. 5.6. At low temperature region ($k_BT<<\Delta E$), the eq. 5.6 can be approximately described as:

$$\frac{I_{X_1^-}}{I_{X_1}} = \frac{\Gamma_{X_1^-}}{\Gamma_{X_1}} \times \frac{k_0 n_e}{k'} \ , \tag{5.7}$$

the intensity ratio of trion and exciton $I_{X_1^-}/I_{X_1}$ suggests the linear dependence of doped carrier density from eq. 5.7. With increasing the back-gate voltage from -45 V, the intensity of X_1^- increases, whereas that of X_1 gradually decreases [49], which will be shown in Figure 6.1(b). Then, the back gate-voltage-dependent PL change between X_1^- and X_1 shows the anti-correlated behavior [49], which will be also described in section 6.2, and the linear increase of PL intensity ratio as a function of back-gate voltage, as shown in Figure 5.7(c). Moreover, the calculated PL intensity ratio using eq. 5.7 as a function of doped carrier density well reproduces the experimental result, as shown in Figure 5.7(d) (red sphere), which also suggests the validity of this analysis.

The temperature dependence of radiative lifetime of negative trion in 3L-ReS_2 is derived as shown in Figure 5.7(d). The radiative lifetime of trion linearly increases with increasing the temperature, and reaches to a few nanoseconds at high temperature above 200 K, which are well consistent with the theoretically calculated radiative lifetime of trion in 2D materials [188,190]. With increasing temperature, the negative trions acquire more thermal energy and their distribution spreads to higher energies in the momentum space. The average trion lifetime increases with the temperature, because the trions with large kinetic energies have longer lifetimes [191,192]. Moreover, the value of radiative lifetime (decay rate) of trion is much shorter (large value) than that of optically forbidden state (dark state) [193], suggests that the negative trion (X_1^-) in 3L-ReS_2 is the optically allowed state (bright exciton) with direct optical transition in the momentum space.

5.7. Chapter summary

In this chapter, I have demonstrated experimental observations of a negatively charged exciton (negative trion) in atomically thin anisotropic ReS_2 by tuning the carrier density. Moreover, the temperature dependent exciton and trion dynamics of 3L-ReS_2 revealed by combination of PL spectroscopy and phenomenological rate equation model was discussed. The derived temperature dependence of radiative lifetime of negative trion in 3L-ReS_2 linearly increases with as increasing the temperature, and the radiative lifetime reaches to a few nanoseconds at high temperature above 200 K. These are well consistent with the theoretically predicted radiative lifetime of trion, which suggests that experimentally observed negative trion is the optically allowed states with direct optical transition in the momentum space. The results of excitonic dynamics gave important insights for understanding the optical physics in anisotropic 2D materials.

Chapter 6. Trion binding energy in ReS_2

In the previous chapter 5, the successful observation of negative trion (negatively charged exciton) in a thin layer ReS_2 was described. The detail excitonic properties of trions in ReS_2 including its binding energy and anisotropic properties will be discussed,

6.1. Introduction

The studies regarding the quasi-1D system have been ones of the very hot topics because of emerging material of monolayer black phosphorous (phosphorene), and so on [19,194,195]. However, the phosphorene is well known as unstable material showing fast degradation in ambient condition, which may limit the progress of fundamental research and applications. Indeed, there are not clear and direct observations of trion or accurate evaluation of its binding energy in the anisotropic 2D materials under the stable condition and in a controlled manner [163,196,197]. In contrast, ReS_2 keeps high stability even in ambient condition, which provides a platform in comprehending study of quasi-1D materials. In this chapter, I will continually introduce the details of charged exciton (trion) with large binding energy (~60 meV) in anisotropic ReS_2 by tuning the carrier density in a controlled manner. In addition, polarized emissions from the trions will be discussed.

6.2. Behavior of trion at different gate voltage

Figure 6.1(a) shows the source-drain current with a function of gate voltage sweeping from -45 to +45 V at 300 K. The source-drain current as a function of gate-voltage shows clear linearly increases, which suggests well-dined device performance with Ohmic contact between the channel and electrodes. Figure 6.1 (b) plots the integrated intensity of X_1^- and X_1 as a function of the applied gate voltage from the fitted results in section 5.4 (Figure 5.3(a)). The relationship between excitation power density and PL spectra are shown in Figure 6.1(c) and (d). Both X_1^- and X_1 linearly increases with an increasing in the excitation power density, which suggests that the observed power density region is in the weak and linear regimes. With a change in gate voltage from -45 V, the intensity of X_1^- increases, whereas that of X_1 gradually decreases. Note that the gate-voltage-dependent PL changes between X_1^- and X_1 are strongly anti-correlated.

The electric properties of 3L-ReS_2 with FET structure are investigated at 20 K to provide additional information for the gate-dependent spectral changes. The transfer characteristic in Figure 6.1(e) shows the source-drain current ($I_{\mathrm{D\text{-}S}}$) with log scale monitored at source-drain voltage ($V_{\mathrm{D\text{-}S}}$) of 0.5 V, as a function of gate voltage (V_{G}) at range of -45 V to 45 V. Linear scale of transfer characteristic is also shown in Figure 6.1(b) (black curves). The source-drain current does not flow below -20 V, drastically flows around -10 V and increases with increasing the gate voltage from -10 to 45 V, which suggests that the electrical properties of 3L-ReS_2 at 20 K are intrinsic below -20 V and *n*-type (electron doped) semiconductor above -20 V. The doped carrier density *n* under gate voltage V_{G} is estimated from the relationship of geometric capacitance and back-gate using $n \approx \frac{\varepsilon_{\mathrm{r}}\varepsilon_0}{t_{\mathrm{SiO_2}}}|V_{\mathrm{G}} - V_0|$, where ε_{r} is the dielectric constant, ε_0 is the dielectric constant of vacuum, $t_{\mathrm{SiO_2}}$ is the thickness of SiO_2 [198], and V_0 was defined as an offset voltage when Fermi level is at the middle of band gap (E_{F}=0) [199].

Note that it needs very large gate-voltage to observe of ambipolar characteristics in the back-gate FET, because the atomically thin ReS_2 are relatively heavily *n*-type semiconductor. The atomically thin *intrinsic* $ReSe_2$ with similar band gap to the atomically thin ReS_2 shows clearly ambipolar behavior. The range of off-current voltage in the transfer characteristics of back-gate $ReSe_2$ FET using similar substrate mainly determined by the band gap is ~70 ± 10 V [200]. As a reference, the range of off-current voltage in the transfer characteristics of back-gate ReS_2 FET used in this study is estimated as ~80 ± 10 V with consideration of a difference of band gap between ReS_2 and $ReSe_2$. The zero-gate voltage (V_0) is determined as V_0 is -60 ± 10 V in the 3L-ReS_2 FET device.

The increase electron density controlled by the gate-voltage affects the linewidth. Figure 6.2 (f) shows gate-voltage dependence of homogeneous linewidth corresponding to the Lorentzian linewidth with error bar. The homogeneous linewidth is obtained after the spectral fitting using Voigt function with assuming the inhomogeneous Gaussian linewidth (~11 meV), shows best fitted results. The homogeneous linewidth of X_1 (exciton) linearly increases with increasing electron density by increasing the gate-voltage from -45 to 45 V, while X_1^- shows almost constant behavior. The homogeneous linewidth of X_1 is mainly dominated by dephasing of exciton. The experimentally observed linear dependence of linewidth broadening as a function of doped electron density suggest the homogeneous linewidth is dominated by the shortening of exciton dephasing due to exciton and electron scattering process, which has been reported in monolayer-MoS_2 [186,201,202].

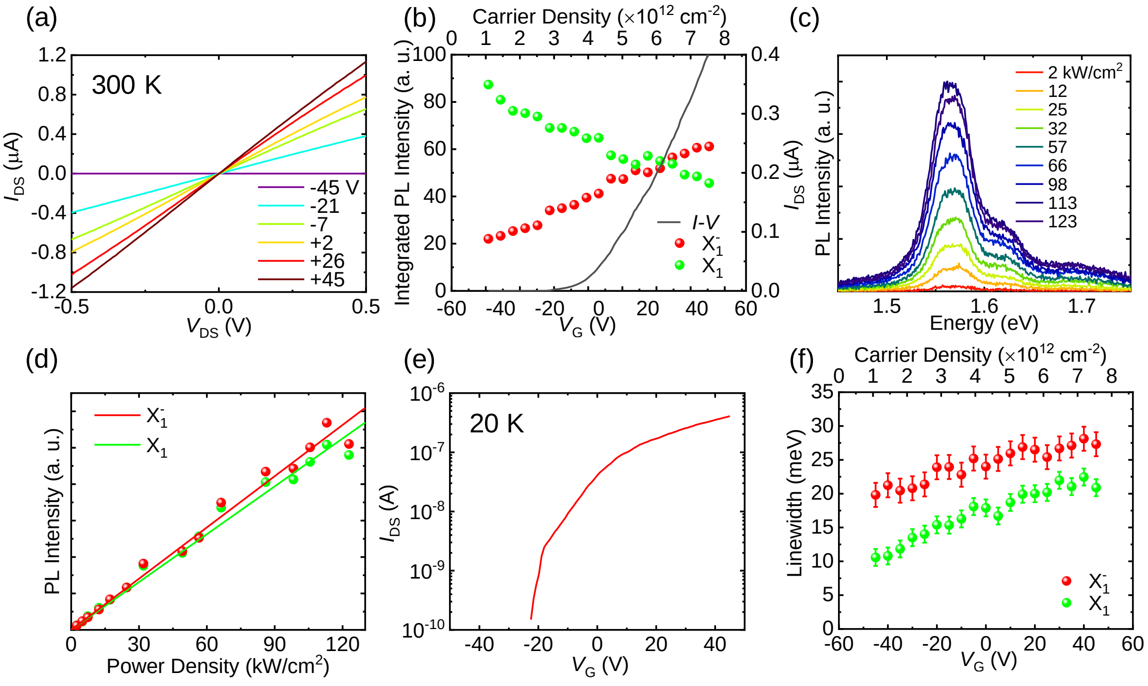

Figure 6.1 (a) Source-Drain current of 3L-ReS$_2$ as a function of gate voltage from -45V to +45V at 300K. (b) Integrated PL intensity of the X$_1^-$ (red) and X$_1$ (green) peaks as a function of the back gate-voltage (left). The transfer characteristics of the source–drain current as a function of the gate-voltage (I_{DS}-V_G) (right) is shown. (c) Excitation power dependence of the PL spectra with an applied gate-voltage of 45 V. (d) Plots of the integrated PL intensity of X$_1$ and X$_1^-$ as a function of the excitation power density. Further, the guides for the linear power dependence are also presented. (e) Source-drain current as a function of the gate voltage (log scale). (f) Gate voltage dependence of the homogeneous linewidth for X$_1^-$ (red) and X$_1$ (green).

6.3. Trion binding energy

The inset of Figure 6.2(a) shows the emission energies of exciton (X$_1$) and negative trions (X$_1^-$) in 3L-ReS$_2$ obtained from the spectral fitting procedures as a function of doped carrier density. The energy difference (ΔE) between X_1 (red) and X_1^- (green) is plotted as a function of doped electron density in Figure 6.2 (a). The energy of X_1 (red) and X_1^- (green) are almost independent on the doped carrier density. The energy difference (ΔE) between X_1 (red) and X_1^- is described as $\Delta E(n) = E_{\mathrm{bin}} + E_{\mathrm{F}}(n)$, where E_{bin} is the binding energy of trion. The linear fitting result keeps a constant value at ~18 meV from low to high electron density region as indicated by black line, related to non-shift of Fermi-energy in the conduction band. The ΔE extrapolated at the zero-electron density ($n \sim 0$) indicates that the binding energy of trion is evaluated as ~18 meV in 3L-ReS_2.

To deeply understand the nature of trions, we investigated the binging energy of ReS_2 with different layer thickness. Figure 6.2(b) shows the PL spectra with various layer thickness (5, 3, 2 and 1L), and the spectral fitted results in each spectra. The gravity of center of energy in the PL spectra shifts at the higher energy side with decreasing the layer thickness which is consistent with the previously reported results [203]. The emission peaks of exciton (X_1) and trion (X_1^-) in each layer are assigned from the gate voltage-dependent PL spectra. We consider that the gate-bias voltage is homogeneously applied in a few layer ReS_2, because the electric potentials are same between interlayers [204]. These indicate that the same number and homogeneous doped carriers at introduced in a few layer ReS_2. The detail PL spectra of 2L and 5L are shown in the Figure 6.3(a) and (b). The energy difference between exciton (X_1) and trion (X_1^-), defined as ΔE significantly increases with decreasing layer thickness of ReS_2.

Figure 6.2(c) shows the evaluated binding energy E_{bin} of trions from ΔE in each layer according to the same procedures, described above. The binding energy E_{bin} of trions clearly increase with decreasing the layer thickness from < 15 ± 1 meV in 5L- to

33 ± 1 meV in 2L-ReS$_2$, and reaches to very large value of 57 ± 6 meV in the monolayer limit of ReS$_2$ (1L-ReS$_2$). The increase of binding energy of trions in the thinner layers of ReS$_2$ is caused by the enhancement of Coulomb interaction due to their strong spatial confinement and reduction of dielectric screening [50,163]. Noted that the value (~50 meV) of the trion binding energy in 1L-ReS$_2$ is much larger than that in other TMDs (MX$_2$, M=Mo, W, X=S, Se, Te) such as ~20 meV for MoS$_2$ [199].

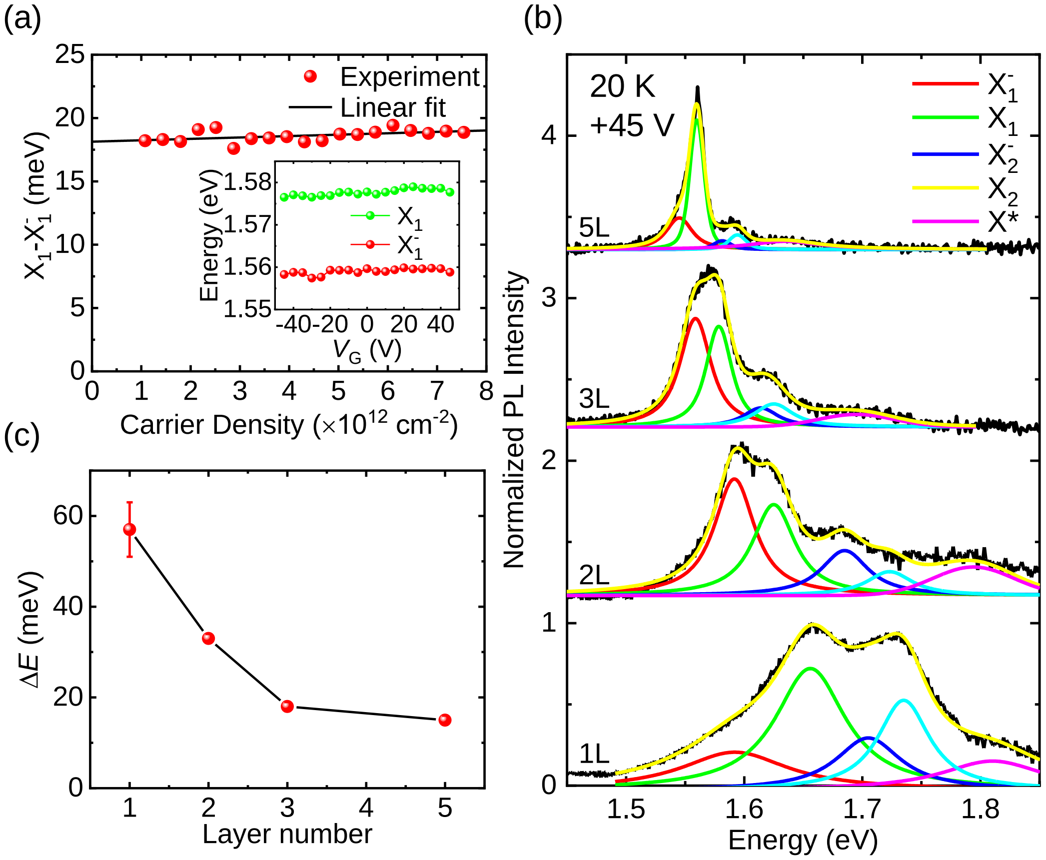

Figure 6.2 (a) Electrostatic doped carrier density dependence of the peak energy difference between X_1^- and X_1. The guide of linear dependence as a function of the doped carrier density is also depicted. The inset shows the gate voltage dependence of the peak energy of X_1^- (red) and X_1 (green) using the Voigt fitting procedure. (b) Layer number dependence of the normalized PL spectra with Voigt function fitting at 20 K with gate voltage of +45 V. The spectrum of 1L-ReS$_2$ was detected using 100× objective lens (NA

= 0.85). The black curve represents the experimental data; further, the red, green, blue, cyan, magenta and yellow curves denote X_1^-, X_1, X_2^-, X_2, higher-series exciton and the total of each component, respectively. (c) Evaluated trion binding energy (ΔE) as a function of the ReS_2 layer number.

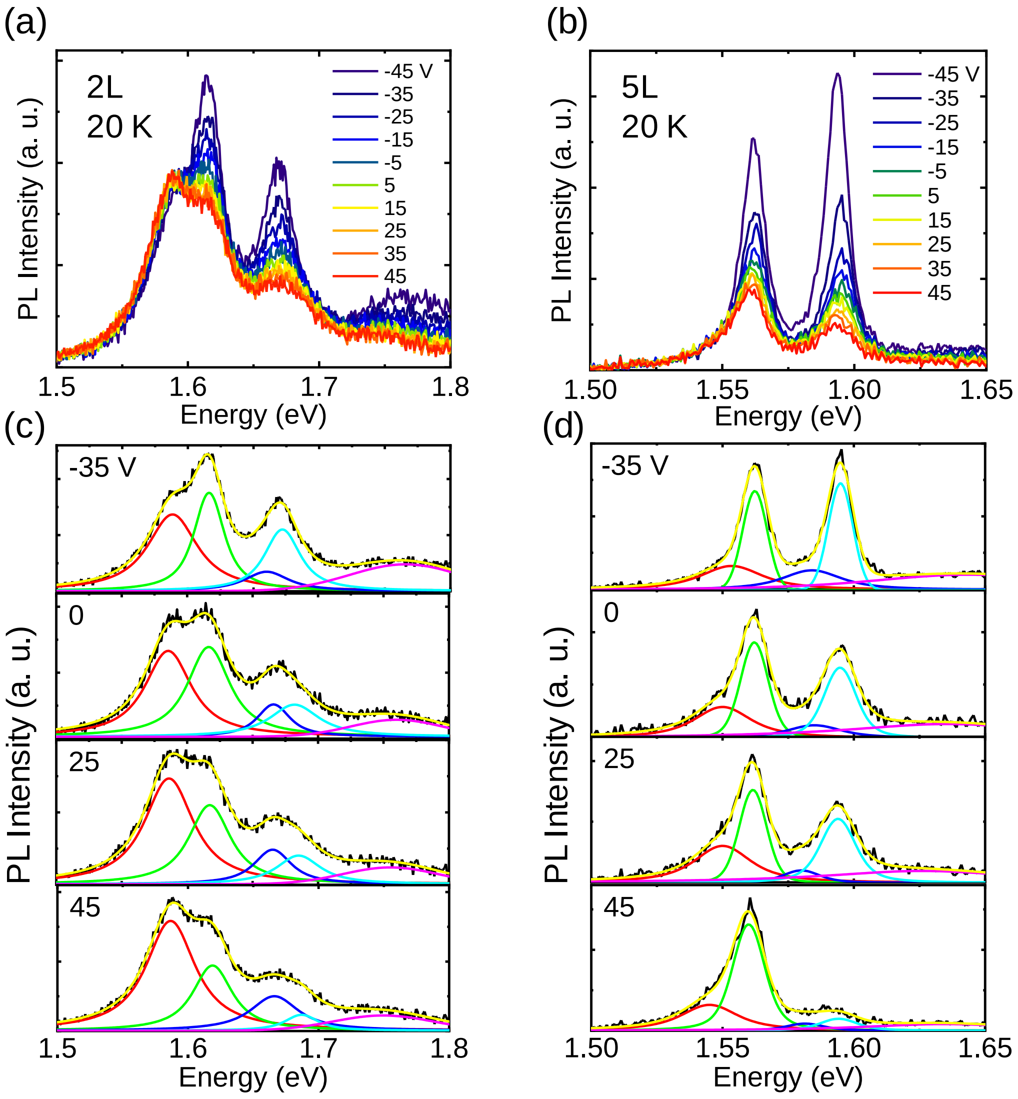

Figure 6.3 (a) and (b) PL spectra of 2L- and 5L-ReS_2 under different back-gate voltages at 20 K. (c) and (d) PL spectra of 2L- and 5L-ReS_2 with an applied gate voltage of -35, 0, +25 and +45 V. The spectral fitted curves obtained by assuming the Voigt functions are

indicated.

6.4. Polarized emission properties of trion

Polarized emission properties of excitons and trions in the anisotropic ReS_2 was also investigated in this study. Figure 6.4(a) shows polarization-resolved PL spectra of 3L-ReS_2 at the gate voltage of +45 V, excited at polarization angle θ of 45° to observe both X_1 ,X_1^-, X_2^- and X_2, where θ is defined the angle between the linear polarization plane of laser and *b*-axis of ReS_2. The PL signal was detected by changing the detected polarization angle. The PL spectra exhibit three peaks including X_1^- (1.56 eV), X_1 (1.58 eV) and X_2^- (1.62 eV, blue), X_2 (1.63 eV, cyan), and the spectral shape significantly changed depending on the detection angle. The X_1^- and X_1 emissions are strong when the detection angle is approximately parallel to the *b*-axis, while the X_2 emissions is strong when the detection angle is almost perpendicular to the *b*-axis. This behavior is clearly shown in a 2D colour plot of PL spectra as a function of detected polarized angle θ in Figure 6.4(b). The result indicates that the emissions from the trions as well as excitons show a distinct polarization characteristic and are linearly polarized.

Figure 6.4(c) shows the polar plot of PL intensity of X_1^-, X_1, X_2^- and X_2 as a function of θ. The polar plots of X_1^-, $X_{1,}$ X_2^- and X_2 integrated intensity show double-lobed features. The emissions of X_1 and X_2 are maximized at different polarization angles: X_1 (green) is almost parallel to the *b*-axis, and X_2 (cyan) is tilted with approximately 60° from the *b*-axis, close to the perpendicular against the *b*-axis. The trion (X_1^-) with the double-lobed feature in the polar plot shows the linearly polarized emissions, but the polarization direction is slightly tilted from *b*-axis with an angle of 30°, which is in between the X_1

and X_2 maximum angle. This tendency might provide a valuable information during the formation dynamics of trion. The X_1 is bound along the crystal direction of the rhenium-rhenium atomic chains (*b*-axis) and X_2 is bound along rhenium-sulfide atomic chains. The 30° angle-dependence of X_1^- suggests the exciton X_1 along the rhenium-rhenium direction do not capture electrons in the same rhenium-rhenium direction, but electrons along the rhenium-sulfide direction to form the negatively charged trion state X_1^-. Same phenomena could also be found at X_2^- side. The trion formation process may increase the effective dimensionality from the pure 1D system, will be discussed in next section.

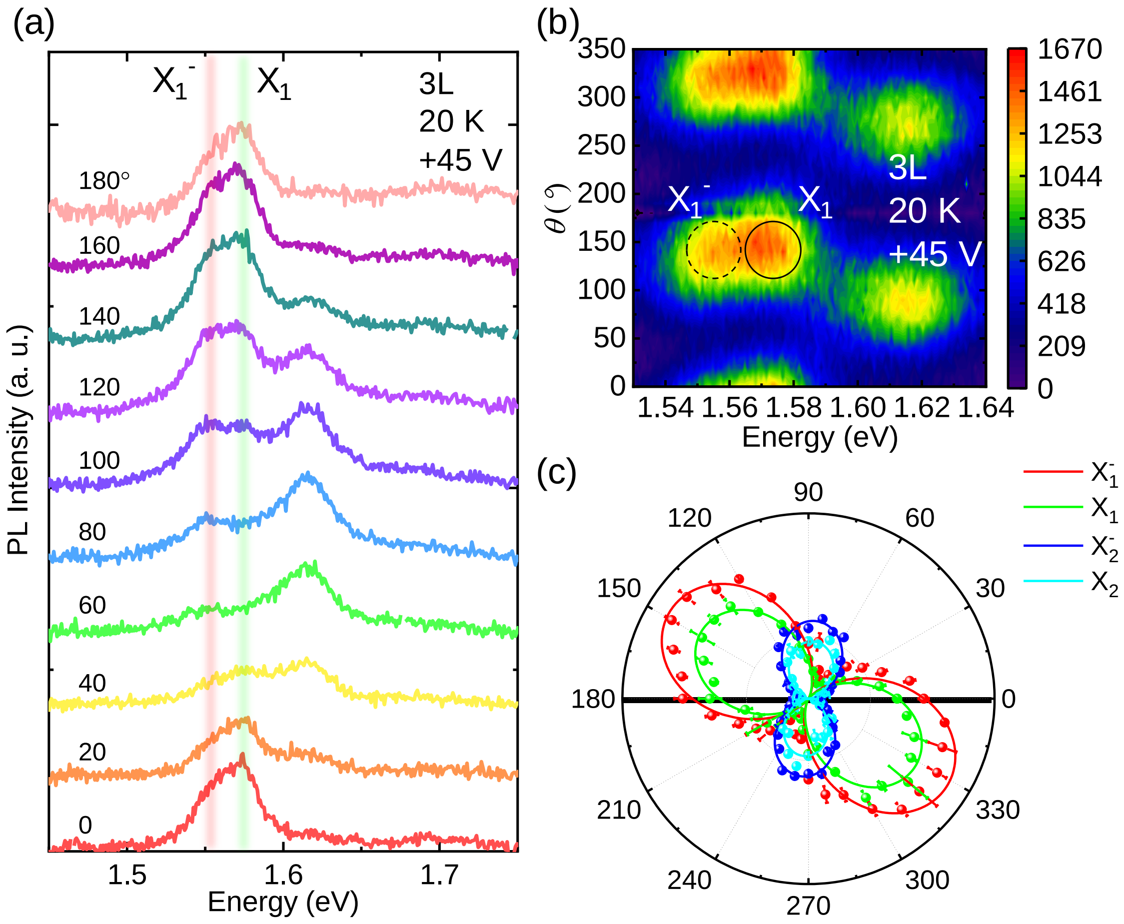

Figure 6.4 (a) Polarization-resolved PL spectra of 3L-ReS_2 with different polarization angles at 20 K at an applied gate voltage of +45 V. The incident angle of the linear

polarization of the laser is fixed at 45°. The detection angle changes from 0° to 180°, where the angle is defined relative to the *b*-axis. The red, green and blue lines denote the peak position of X_1^-, X_1, X_2^- and X_2, respectively. (b) 2D contour plot of the PL spectra as a function of the polarization angle θ. (c) Polar plot of the integrated PL intensity of X_1^-, X_1, X_2^- and X_2. The maroon-filled circle is obtained from the results of the fitting procedures. The solid circle line is fitted by the cos2θ function. The red, green and blue lines denote the peak position of X_1^-, X_1, X_2^- and X_2, respectively. The black line indicates the *b*-axis direction.

6.5. Dimensionality of excitonic states in ReS_2

The studies regarding the quasi-1D system have been conducted as very hot topics because of emerging material of monolayer black phosphorous (phosphorene), and so on. In section 6.3, the strongly bound trion with a binding energy of ~60 meV in 1L-ReS_2 has been described. This large binding energy may come from the strong spatial confinement in monolayer limit, reduction of dielectric screening effect in monolayer material and reduction of dimensionality.

The binding energies of the trions (E_{bin}) in the quasi-1D system by variational quantum Monte Carlo method to analyze the dimensionality can be presented as follows [205]:

$$E_{\mathrm{bin}} = \left(-\frac{4}{(D-1)^2} - c_0 - \sum_{i=1}^{4} c_i\, D^{-i} e^{-D} \right) \times R_y^* \ , \tag{6.1}$$

where D denotes the effective dimension of trions, Ry* denotes the effective Rydberg constant and c_n (n = 0–4) denote the coefficients. The coefficient values for the negative trions are given as $c_0 = -0.765$, $c_1 = 368$, $c_2 = -2390$, $c_3 = 4920$ and $c_4 = -3650$ [206]. The effective Rydberg Ry^* for X_1 of 118 meV was used [207]. Figure 6.5(a) denotes the effective dimension as a function of trion binding at different layer numbers. The effective dimensionality was estimated to be around 1.9 from the trion binding energy of the 1L-ReS_2 and calculated value of bulk ReS_2. The evaluated effective dimensionality of 1L-ReS_2 with less than two also supported the quasi-1D nature of the anisotropic ReS_2. The calculation is coming from variational quantum Monte Carlo method. It is just an estimated value without actual physics meaning due to equ. (6.1) experiential parameters. Therefore, the value has been calculated under 2, which can support the ReS_2 with qusia-1D structure. The reduction in dimensionality caused by the anisotropic wavefunction of the trions in ReS_2 further enhanced the electron−hole Coulomb interaction, which is similar to black phosphorene.

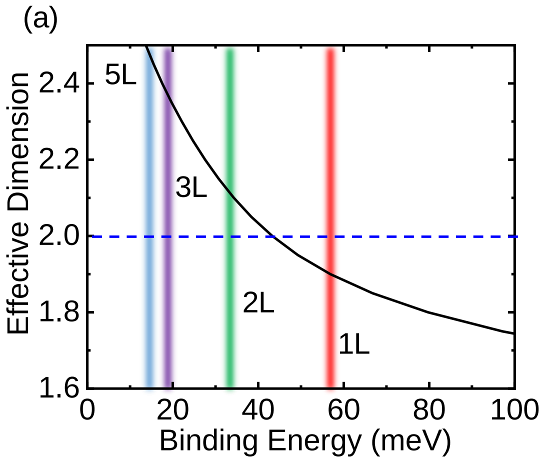

Figure 6.5 (a) Effective dimension *D* as a function of the trion binding energy at different layer numbers calculated using Eq. 6.1

6.6. Chapter summary

In this chapter, we discussed detail of the negative trion states in 1*T* distorted crystal structure of atomically thin ReS_2 FETs by electrostatic carrier doping with applying the gate voltage. It was found that the binding energy of trions strongly depend on the layer thickness and reach to very large value of ~60 meV in monolayer ReS_2 in comparison with that of monolayer MX_2 (M=Mo, W, X=S, Se, Te) due to its anisotropic symmetry structure. The dielectric screening of quasi-1D systems, especially for three-body systems of trion, are raised by this experimental studies of trion with quasi-1D nature in anisotropic 2D materials, which will open new fundamental physical researches in the condensed matter physics. Moreover, the anisotropic and strong polarized emission from the trion in the quasi-1D ReS_2 enable to take the advantage of strong light absorption (large absorption cross-section) in the 2D plane. The stable and anisotropic trion system with large binding energy will provide opportunities and new platform in controllable optical devices at next generation application.

Chapter 7. Summary and future outlook

7.1. Summary

In this thesis, I investigated new members of anisotropic TMDs materials of ReS_2 to show new optical properties and excited state dynamics. The ReS_2 exhibits distinct in-plane anisotropy optical properties. Furthermore, the optical properties and excitonic dynamics in ReS_2 with distorted structures will provide novel insights into studies of atomically thin materials with an additional degree of freedom.

In Chapter 4, I used transient PL and ultrafast pump-probe spectroscopy to study the ultrafast carrier and exciton dynamics of three-layered ReS_2, monitoring the populations of electron-hole pairs and electrons/or holes in the excited states, respectively. We discovered ultrafast direct exciton relaxation (<1 ps) and indirect exciton relaxation (~100 ps) supported using the one-phonon emission process in the indirect-bandgap ReS_2 using two different transient spectroscopies. These new findings provide important information regarding the indirect-bandgap nature of few-layered ReS_2 and the potential of high-frequency dynamical operation of optical devices.

I showed experimental evidence of a negatively charged exciton (negative trion) in atomically thin anisotropic ReS_2 in Chapter 5. The dynamics of optically excited trion were also investigated in a few-layered ReS_2 with a FET structure using the temperature dependence of PL spectroscopy and phenomenological rate equation model. The derived temperature dependence of the radiative lifetime of negative trion in 3L-ReS_2 was found almost linearly increases with an increase in as the temperature, and reaches a few nanoseconds at high temperature above 200 K. These results were consistent with the theoretically predicted radiative lifetime of trion, suggesting that the optically allowed states with direct optical transition in the momentum space are experimentally observed negative trion. The results of excitonic dynamics pave important insights for understanding the optical physics in anisotropic 2D materials.

In Chapter 6, I have investigated new negative trion characteristics originating from the anisotropic quasi-1D nature of the trion wavefunction. The great stability of the trion in monolayer ReS_2, with a high binding energy of 60 meV, was reported experimentally, where its binding energy is more than double that of normal isotropic atomically thin MX_2. This discovery, I believe, will help to advance our understanding of many-body physics in optically stimulated states of such anisotropic atomically thin quasi-1D systems, as well as provide insight into optical devices in a new element of atomically thin-layered ReS_2.

7.2. Future outlook

This thesis has investigated new residents of atomically thin-layered ReS_2 with its novel electronic and optical properties. The obtained insights of excitonic dynamics in ReS_2 would provide new viewpoints in understanding the electronic states of anisotropic atomically thin-layered materials, especially for identifying the semiconductor’s direct or indirect bandgap. Not only ReS_2 but also other 2D materials exhibit weak interlayer coupling and various types of stacking configuration between layers, which might be the main reason the band structure keeps dependent of the layer number. The excitonic dynamics from time-resolved PL and pump-probe spectroscopy mentioned in Chapter 4 also provide information on the detailed band structure of 2D materials. Thus, the studies of excitonic dynamics on ReS_2 would also include significant hints to clarify debatable electronic structures in other 2D materials.

The large binding energy of trion in many-body physics in the anisotropic 2D (quasi-1D) system shows large differences with isotropic 2D materials as a result of reduced dielectric screening effect and dimensionality, which will open new fundamental physical research in condensed matter physics. The trion in ReS_2 is optically initiated, can also be detected electrically in a spatial non-local manner by measuring the current [208], which makes that trion could be used in gate-controlled excitonic device applications such as excitonic (exciton and trion) transistors. Moreover, another application of photodetector with a gate- and light-tunable characteristic by using the advantage of large trion binding energy [209] would be realized in ReS_2.

Moreover, ReS_2 with a stable and anisotropic exciton/trion, shows unique optical behaviors in combination with weak coupling. It could be utilized for a new van der Waals heterostructure building block. Due to the narrow band gap, ReS_2 exhibits strong light absorption (large absorption cross-section in the 2D plane) in visible and NIR light regions [111], therefore it will be expected that the heterostructure occurred in the strong light absorption at the interface of the 2D plane, which will provide an outstanding platform in the studies of combined quasi-1D and 2D heterostructure and practical optoelectronic applications. In addition, the discovery of anisotropic and strongly polarized emission from the trion in the quasi-1D ReS_2 in this study enables us to expect using anisotropic trion responses in advanced functional heterostructure devices with light polarization-sensitive detection.

Bibliography

[1] F. Allhoff, Nanoethics **1**, 185 (2007).

[2] G. A. Mansoori and T. A. F. Soelaiman, J. ASTM Int. **2**, 17 (2005).

[3] S. Bayda, M. Adeel, T. Tuccinardi, M. Cordani, and F. Rizzolio, Molecules **25**, 112 (2020).

[4] P. Dobson, S. King, and H. Jarvie, Https://Www.Britannica.Com/Science/Nanoparticle Web Page (2019).

[5] I. Khan, K. Saeed, and I. Khan, Arab. J. Chem. **12**, 908 (2019).

[6] Unmesha Ray, Https://Www.Azonano.Com/Article.Aspx?ArticleID=4938 Web Page (2018).

[7] P. Bokulich and A. Bokulich, Found. Phys. **35**, 347 (2005).

[8] G. Jaeger, Am. J. Phys. **82**, 896 (2014).

[9] I. Capek, in *Stud. Interface Sci.* (Elsevier, 2006), pp. 1–69.

[10] K. S. Novoselov, A. K. Geim, S. V. Morozov, D. Jiang, Y. Zhang, S. V. Dubonos, I. V. Grigorieva, and A. A. Firsov, Science **306**, 666 (2004).

[11] M. Berger, Https://Www.Nanowerk.Com/What_is_graphene.Php Web Page (2019).

[12] F. Bonaccorso, Z. Sun, T. Hasan, and A. C. Ferrari, Nat. Photonics **4**, 611 (2010).

[13] N. F. Atta, A. Galal, and E. H. El-Ads, in *Biosens. - Micro Nanoscale Appl.* (InTech, 2015), pp. 37–84.

[14] R. Singh and S. Kumar, in *Compr. Anal. Chem.* (Elsevier B.V., 2020), pp. 201–233.

[15] A. K. Geim and I. V. Grigorieva, Nature **499**, 419 (2013).

[16] M. Berger, in *Nanoengineering* (Royal Society of Chemistry, 2019), pp. 61–85.

[17] K. F. Mak, C. Lee, J. Hone, J. Shan, and T. F. Heinz, Phys. Rev. Lett. **105**, 136805 (2010).

[18] Q. H. Wang, K. Kalantar-Zadeh, A. Kis, J. N. Coleman, and M. S. Strano, Nat. Nanotechnol. **7**, 699 (2012).

[19] L. Li, Y. Yu, G. J. Ye, Q. Ge, X. Ou, H. Wu, D. Feng, X. H. Chen, and Y. Zhang, Nat. Nanotechnol. **9**, 372 (2014).

[20] L. Song, L. Ci, H. Lu, P. B. Sorokin, C. Jin, J. Ni, A. G. Kvashnin, D. G. Kvashnin, J. Lou, B. I. Yakobson, and P. M. Ajayan, Nano Lett. **10**, 3209 (2010).

[21] K. S. Novoselov, D. Jiang, F. Schedin, T. J. Booth, V. V. Khotkevich, S. V. Morozov, and A. K. Geim, Proc. Natl. Acad. Sci. U. S. A. **102**, 10451 (2005).

[22] Y. H. Lee, X. Q. Zhang, W. Zhang, M. T. Chang, C. Te Lin, K. Di Chang, Y. C. Yu, J. T. W. Wang, C. S. Chang, L. J. Li, and T. W. Lin, Adv. Mater. **24**, 2320 (2012).

[23] B. Radisavljevic, A. Radenovic, J. Brivio, V. Giacometti, and A. Kis, Nat. Nanotechnol. **6**, 147 (2011).

[24] A. Splendiani, L. Sun, Y. Zhang, T. Li, J. Kim, C. Y. Chim, G. Galli, and F. Wang, Nano Lett. **10**, 1271 (2010).

[25] Y. Li, S. Tongay, Q. Yue, J. Kang, J. Wu, and J. Li, J. Appl. Phys. **114**, 174307 (2013).

[26] N. E. Staley, J. Wu, P. Eklund, Y. Liu, L. Li, and Z. Xu, Phys. Rev. B **80**, 184505 (2009).

[27] M. Y. Li, C. H. Chen, Y. Shi, and L. J. Li, Mater. Today **19**, 322 (2016).

[28] A. K. Geim and I. V. Grigorieva, Nature **499**, 419 (2013).

[29] S. Tongay, H. Sahin, C. Ko, A. Luce, W. Fan, K. Liu, J. Zhou, Y. S. Huang, C. H. Ho, J. Yan, D. F. Ogletree, S. Aloni, J. Ji, S. Li, J. Li, F. M. Peeters, and J. Wu, Nat. Commun. **5**, 3252 (2014).

[30] D. Ovchinnikov, F. Gargiulo, A. Allain, D. J. Pasquier, D. Dumcenco, C. H. Ho, O. V. Yazyev, and A. Kis, Nat. Commun. **7**, 12391 (2016).

[31] H. Jang, C. R. Ryder, J. D. Wood, M. C. Hersam, and D. G. Cahill, Adv. Mater. **29**, 1700650 (2017).

[32] S. Horzum, D. ÇakIr, J. Suh, S. Tongay, Y. S. Huang, C. H. Ho, J. Wu, H. Sahin, and F. M. Peeters, Phys. Rev. B **89**, 155433 (2014).

[33] O. B. Aslan, D. A. Chenet, A. M. Van Der Zande, J. C. Hone, and T. F. Heinz, ACS Photonics **3**, 96 (2016).

[34] E. Liu, Y. Fu, Y. Wang, Y. Feng, H. Liu, X. Wan, W. Zhou, B. Wang, L. Shao, C. H. Ho, Y. S. Huang, Z. Cao, L. Wang, A. Li, J. Zeng, F. Song, X. Wang, Y. Shi, H. Yuan, H. Y. Hwang, Y. Cui, F. Miao, and D. Xing, Nat. Commun. **6**, 6991 (2015).

[35] H. Yang, H. Jussila, A. Autere, H. P. Komsa, G. Ye, X. Chen, T. Hasan, and Z. Sun, ACS Photonics **4**, 3023 (2017).

[36] K. Thakar, B. Mukherjee, S. Grover, N. Kaushik, M. Deshmukh, and S. Lodha, ACS Appl. Mater. Interfaces **10**, 36512 (2018).

[37] Y. Shao, J. Wang, H. Wu, J. Liu, I. A. Aksay, and Y. Lin, Electroanalysis **22**, 1027 (2010).

[38] Z. Liu, S. P. Lau, and F. Yan, Chem. Soc. Rev. **44**, 5638 (2015).

[39] A. Ambrosi, C. K. Chua, N. M. Latiff, A. H. Loo, C. H. A. Wong, A. Y. S. Eng, A. Bonanni, and M. Pumera, Chem. Soc. Rev. **45**, 2458 (2016).

[40] F. Bonaccorso, Z. Sun, T. Hasan, and A. C. Ferrari, Nat. Photonics **4**, 611 (2010).

[41] R. Murray, Https://Www.Advancedsciencenews.Com/beyond-Graphene-New-2d-Materials-with-Graphene-like-Properties/ Web Page (2019).

[42] K. S. Novoselov, A. K. Geim, S. V. Morozov, D. Jiang, M. I. Katsnelson, I. V. Grigorieva, S. V. Dubonos, and A. A. Firsov, Nature **438**, 197 (2005).

[43] A. Chaves, J. G. Azadani, H. Alsalman, D. R. da Costa, R. Frisenda, A. J. Chaves, S. H. Song, Y. D. Kim, D. He, J. Zhou, A. Castellanos-Gomez, F. M. Peeters, Z. Liu, C. L. Hinkle, S. H. Oh, P. D. Ye, S. J. Koester, Y. H. Lee, P. Avouris, X. Wang, and T. Low, Npj 2D Mater. Appl. **4**, 29 (2020).

[44] G. R. Bhimanapati, Z. Lin, V. Meunier, Y. Jung, J. Cha, S. Das, D. Xiao, Y. Son, M. S. Strano, V. R. Cooper, L. Liang, S. G. Louie, E. Ringe, W. Zhou, S. S. Kim, R. R. Naik, B. G. Sumpter, H. Terrones, F. Xia, Y. Wang, J. Zhu, D. Akinwande,

N. Alem, J. A. Schuller, R. E. Schaak, M. Terrones, and J. A. Robinson, ACS Nano **9**, 11509 (2015).

[45] E. Gao, S. Z. Lin, Z. Qin, M. J. Buehler, X. Q. Feng, and Z. Xu, J. Mech. Phys. Solids **115**, 248 (2018).

[46] K. S. Novoselov and A. H. Castro Neto, Phys. Scr. **146**, 6 (2012).

[47] A. POLIMENI’S, Https://Antoniopolimeni-Physics.Weebly.Com/Two-Dimensional-Materials.Html Web Page (2017).

[48] P. Tonndorf, R. Schmidt, P. Böttger, X. Zhang, J. Börner, A. Liebig, M. Albrecht, C. Kloc, O. Gordan, D. R. T. Zahn, S. Michaelis de Vasconcellos, and R. Bratschitsch, Opt. Express **21**, 4908 (2013).

[49] X. Wang, K. Shinokita, Y. Miyauchi, N. T. Cuong, S. Okada, and K. Matsuda, Adv. Funct. Mater. **29**, 1905961 (2019).

[50] A. Sharma, H. Yan, L. Zhang, X. Sun, B. Liu, and Y. Lu, Acc. Chem. Res. **51**, 1164 (2018).

[51] M. Gehlmann, I. Aguilera, G. Bihlmayer, S. Nemšák, P. Nagler, P. Gospodarič, G. Zamborlini, M. Eschbach, V. Feyer, F. Kronast, E. Młyńczak, T. Korn, L. Plucinski, C. Schüller, S. Blügel, and C. M. Schneider, Nano Lett. **17**, 5187 (2017).

[52] B. Van Zeghbroeck, Https://Www.Coursehero.Com/File/6629082/03-RevSemicon/ Web Page (2011).

[53] The Editors of Encyclopaedia, Https://Www.Britannica.Com/Science/Semiconductor Web Page (2021).

[54] Nick Connor, Https://Www.Coursehero.Com/File/6629082/03-RevSemicon/ Web Page (2019).

[55] Hitachi, Https://Www.Hitachi-Hightech.Com/Global/Products/Device/Semiconductor/Properties.Html Web Page (2020).

[56] M. Fox, in *Opt. Prop. Solids Second Ed.* (2010), pp. 49–107.

[57] Kara Manke, Https://Researchblog.Duke.Edu/2018/01/16/Farewell-Electrons-Future-Electronics-May-Ride-on-New-Three-in-One-Particle/ Web Page (2018).

[58] B. B. M. Nur, Kyoto University: Study on Photoluminescence Quantum Yields of Atomically Thin-Layered Two-Dimensional Semiconductors Transition Metal Dichalcogenides, 2018.

[59] H. Nan, Z. Wang, W. Wang, Z. Liang, Y. Lu, Q. Chen, D. He, P. Tan, F. Miao, X. Wang, J. Wang, and Z. Ni, ACS Nano **8**, 5738 (2014).

[60] D. Kozawa, Kyoto University: Behavior of Photocarrier in Atomically Thin Two-Dimensional Semiconducting Materials for Optoelectronics, 2015.

[61] C. Dekker, Phys. Today **52**, 22 (1999).

[62] X. Wu, Y. Shao, H. Liu, Z. Feng, Y. L. Wang, J. T. Sun, C. Liu, J. O. Wang, Z. L. Liu, S. Y. Zhu, Y. Q. Wang, S. X. Du, Y. G. Shi, K. Ibrahim, and H. J. Gao, Adv. Mater. **29**, 1605407 (2017).

[63] D. J. Late, Y. K. Huang, B. Liu, J. Acharya, S. N. Shirodkar, J. Luo, A. Yan, D. Charles, U. V. Waghmare, V. P. Dravid, and C. N. R. Rao, ACS Nano **7**, 4879 (2013).

[64] W. Zhu, M. N. Yogeesh, S. Yang, S. H. Aldave, J. S. Kim, S. Sonde, L. Tao, N. Lu, and D. Akinwande, Nano Lett. **15**, 1883 (2015).

[65] J. Hassoun, F. Bonaccorso, M. Agostini, M. Angelucci, M. G. Betti, R. Cingolani, M. Gemmi, C. Mariani, S. Panero, V. Pellegrini, and B. Scrosati, Nano Lett. **14**, 4901 (2014).

[66] M. Bernardi, M. Palummo, and J. C. Grossman, Nano Lett. **13**, 3664 (2013).

[67] N. Rohaizad, C. C. Mayorga-Martinez, M. Fojtů, N. M. Latiff, and M. Pumera, Chem. Soc. Rev. **50**, 619 (2021).

[68] H. Chen, Z. Li, X. Liu, J. Zhong, T. Lin, L. Guo, and F. Fu, Spectrochim. Acta - Part A Mol. Biomol. Spectrosc. **185**, 271 (2017).

[69] Y. Wang and Y. Ni, Anal. Chem. **86**, 7463 (2014).

[70] X. Hun, S. Wang, S. Wang, J. Zhao, and X. Luo, Sensors Actuators, B Chem. **249**, 83 (2017).

[71] M. Rong, L. Lin, X. Song, Y. Wang, Y. Zhong, J. Yan, Y. Feng, X. Zeng, and X. Chen, Biosens. Bioelectron. **68**, 210 (2015).

[72] X. Liu, J. Zhang, J. Di, Y. Long, W. Li, and Y. Tu, J. Colloid Interface Sci. **505**, 964 (2017).

[73] R. J. Toh, C. C. Mayorga-Martinez, J. Han, Z. Sofer, and M. Pumera, Anal. Chem. **89**, 4978 (2017).

[74] M. Sadhukhan and S. Barman, J. Mater. Chem. A **1**, 2752 (2013).

[75] L. A. Cipriano, G. Di Liberto, S. Tosoni, and G. Pacchioni, Nanoscale **12**, 17494 (2020).

[76] G. Ramalingam, P. Kathirgamanathan, G. Ravi, T. Elangovan, B. Arjun kumar, N. Manivannan, and K. Kasinathan, in *Quantum Dots - Fundam. Appl.* (IntechOpen, 2020).

[77] T. Radsar, H. Khalesi, and V. Ghods, Opt. Quantum Electron. **53**, 178 (2021).

[78] J. Pu, L. Tang, C. Li, T. Li, L. Ling, K. Zhang, Q. Li, and Y. Yao, RSC Adv. **5**, 44142 (2015).

[79] A. Varykhalov, D. Marchenko, J. Sánchez-Barriga, M. R. Scholz, B. Verberck, B. Trauzettel, T. O. Wehling, C. Carbone, and O. Rader, Phys. Rev. X **2**, 041017 (2012).

[80] K. A. Madurani, S. Suprapto, N. I. Machrita, S. L. Bahar, W. Illiya, and F. Kurniawan, ECS J. Solid State Sci. Technol. **9**, 093013 (2020).

[81] Ossila, Https://Www.Ossila.Com/Products/Hexagonal-Boron-Nitride Web Page (2017).

[82] K. Zhang, Y. Feng, F. Wang, Z. Yang, and J. Wang, J. Mater. Chem. C **5**, 11992 (2017).

[83] L. H. Li and Y. Chen, Adv. Funct. Mater. **26**, 2594 (2016).

[84] Q. Weng, X. Wang, X. Wang, Y. Bando, and D. Golberg, Chem. Soc. Rev. **45**, 3989 (2016).

[85] Ossila, Https://Www.Ossila.Com/Products/Black-Phosphorus Web Page (2017).

[86] V. Wang, Y. Kawazoe, and W. T. Geng, Phys. Rev. B **91**, 045433 (2015).

[87] I. Kriegel, N. Borys, K. Zhang, A. Jansons, B. Crockett, K. Koskela, E. Barnard, E. Penzo, J. Hutchison, J. Robinson, and L. Manna, Mesoscale Nanoscale Phys. **arXiv**, 1810.05385 (2018).

[88] K. Matsuda, J. Phys. Soc. Japan **84**, 121009 (2015).

[89] W. O. Winer, Wear **10**, 422 (1967).

[90] A. Splendiani, L. Sun, Y. Zhang, T. Li, J. Kim, C. Y. Chim, G. Galli, and F. Wang, Nano Lett. **10**, 1271 (2010).

[91] K. F. Mak, C. Lee, J. Hone, J. Shan, and T. F. Heinz, Phys. Rev. Lett. **105**, 136805 (2010).

[92] Ossila, Https://Www.Ossila.Com/Pages/Molybdenum-Disulfide-MoS_2 Web Page (2017).

[93] S. Mouri, Y. Miyauchi, and K. Matsuda, Nano Lett. **13**, 5944 (2013).

[94] K. F. Mak, K. He, J. Shan, and T. F. Heinz, Nat. Nanotechnol. **7**, 494 (2012).

[95] S. Barraza-Lopez, F. Xia, W. Zhu, and H. Wang, J. Appl. Phys. **128**, 140401 (2020).

[96] Z. Chi, X. Chen, F. Yen, F. Peng, Y. Zhou, J. Zhu, Y. Zhang, X. Liu, C. Lin, S. Chu, Y. Li, J. Zhao, T. Kagayama, Y. Ma, and Z. Yang, Phys. Rev. Lett. **120**, 037002 (2018).

[97] Z. Fei, W. Zhao, T. A. Palomaki, B. Sun, M. K. Miller, Z. Zhao, J. Yan, X. Xu, and D. H. Cobden, Nature **560**, 336 (2018).

[98] A. Favron, E. Gaufrès, F. Fossard, A. L. Phaneuf-Laheureux, N. Y. W. Tang, P. L. Lévesque, A. Loiseau, R. Leonelli, S. Francoeur, and R. Martel, Nat. Mater. **14**, 826 (2015).

[99] J. O. Island, G. A. Steele, H. S. J. Van Der Zant, and A. Castellanos-Gomez, 2D Mater. **2**, 011002 (2015).

[100] A. Ziletti, A. Carvalho, D. K. Campbell, D. F. Coker, and A. H. Castro Neto, Phys. Rev. Lett. **114**, 046801 (2015).

[101] D. Wolverson, S. Crampin, A. S. Kazemi, A. Ilie, and S. J. Bending, ACS Nano **8**, 11154 (2014).

[102] S. Tongay, H. Sahin, C. Ko, A. Luce, W. Fan, K. Liu, J. Zhou, Y. S. Huang, C. H. Ho, J. Yan, D. F. Ogletree, S. Aloni, J. Ji, S. Li, J. Li, F. M. Peeters, and J. Wu, Nat. Commun. **5**, 3252 (2014).

[103] Y. C. Lin, H. P. Komsa, C. H. Yeh, T. Björkman, Z. Y. Liang, C. H. Ho, Y. S. Huang, P. W. Chiu, A. V. Krasheninnikov, and K. Suenaga, ACS Nano **9**, 11249 (2015).

[104] D. A. Chenet, O. B. Aslan, P. Y. Huang, C. Fan, A. M. Van Der Zande, T. F. Heinz, and J. C. Hone, Nano Lett. **15**, 5667 (2015).

[105] F. Liu, S. Zheng, X. He, A. Chaturvedi, J. He, W. L. Chow, T. R. Mion, X. Wang, J. Zhou, Q. Fu, H. J. Fan, B. K. Tay, L. Song, R. H. He, C. Kloc, P. M. Ajayan, and Z. Liu, Adv. Funct. Mater. **26**, 1169 (2016).

[106] A. J. Cho, S. D. Namgung, H. Kim, and J. Y. Kwon, APL Mater. **5**, 76101 (2017).

[107] D. Ovchinnikov, F. Gargiulo, A. Allain, D. J. Pasquier, D. Dumcenco, C. H. Ho, O. V. Yazyev, and A. Kis, Nat. Commun. **7**, 12391 (2016).

[108] H. Zhao, J. Wu, H. Zhong, Q. Guo, X. Wang, F. Xia, L. Yang, P. Tan, and H. Wang, Nano Res. **8**, 3651 (2015).

[109] R. He, J. A. Yan, Z. Yin, Z. Ye, G. Ye, J. Cheng, J. Li, and C. H. Lui, Nano Lett. **16**, 1404 (2016).

[110] E. Lorchat, G. Froehlicher, and S. Berciaud, ACS Nano **10**, 2752 (2016).

[111] Q. Zhang and L. Fu, Chem **5**, 505 (2019).

[112] Y. C. Lin, H. P. Komsa, C. H. Yeh, T. Björkman, Z. Y. Liang, C. H. Ho, Y. S. Huang, P. W. Chiu, A. V. Krasheninnikov, and K. Suenaga, ACS Nano **9**, 11249 (2015).

[113] S. Shen, Y. Chao, Z. Dong, G. Wang, X. Yi, G. Song, K. Yang, Z. Liu, and L. Cheng, Adv. Funct. Mater. **27**, 1700250 (2017).

[114] J. Shim, A. Oh, D. H. Kang, S. Oh, S. K. Jang, J. Jeon, M. H. Jeon, M. Kim, C. Choi, J. Lee, S. Lee, G. Y. Yeom, Y. J. Song, and J. H. Park, Adv. Mater. **28**, 6985 (2016).

[115] Q. Huang, S. Wang, J. Zhou, X. Zhong, and Y. Huang, RSC Adv. **8**, 4624 (2018).

[116] Z. H. Miao, L. X. Lv, K. Li, P. Y. Liu, Z. Li, H. Yang, Q. Zhao, M. Chang, L. Zhen, and C. Y. Xu, Small **14**, 1703789 (2018).

[117] M. Rahman, K. Davey, and S. Z. Qiao, Adv. Funct. Mater. **27**, 1606129 (2017).

[118] NanoPhoton, Https://Www.Nanophoton.Net/Products/Ramantouch Web Page (2016).

[119] D. Beaglehole and R. G. Buckley, Appl. Opt. Vol. 16, Issue 9, Pp. 2495-2499 **16**, 2495 (1977).

[120] K. F. Mak, M. Y. Sfeir, Y. Wu, C. H. Lui, J. A. Misewich, and T. F. Heinz, Phys. Rev. Lett. **101**, 196405 (2008).

[121] J. D. E. McIntyre and D. E. Aspnes, Surf. Sci. **24**, 417 (1971).

[122] T. Yamaoka, H. E. Lim, S. Koirala, X. Wang, K. Shinokita, M. Maruyama, S. Okada, Y. Miyauchi, and K. Matsuda, Adv. Funct. Mater. **28**, 1801021 (2018).

[123] Y. Ryu, W. Kim, S. Koo, H. Kang, K. Watanabe, T. Taniguchi, and S. Ryu, Nano Lett. **17**, 7267 (2017).

[124] P. Ajayan, P. Kim, and K. Banerjee, Phys. Today **69**, 38 (2016).

[125] Q. H. Wang, K. Kalantar-Zadeh, A. Kis, J. N. Coleman, and M. S. Strano, Nat. Nanotechnol. **7**, 699 (2012).

[126] K. F. Mak, C. Lee, J. Hone, J. Shan, and T. F. Heinz, Phys. Rev. Lett. **105**, 136805 (2010).

[127] K. S. Novoselov, D. Jiang, F. Schedin, T. J. Booth, V. V. Khotkevich, S. V. Morozov, and A. K. Geim, Proc. Natl. Acad. Sci. U. S. A. **102**, 10451 (2005).

[128] K. S. Novoselov, A. K. Geim, S. V. Morozov, D. Jiang, Y. Zhang, S. V. Dubonos, I. V. Grigorieva, and A. A. Firsov, Science **306**, 666 (2004).

[129] A. Arora, J. Noky, M. Drüppel, B. Jariwala, T. Deilmann, R. Schneider, R. Schmidt, O. Del Pozo-Zamudio, T. Stiehm, A. Bhattacharya, P. Krüger, S. Michaelis de Vasconcellos, M. Rohlfing, and R. Bratschitsch, Nano Lett. **17**, 3202 (2017).

[130] S. Sim, D. Lee, A. V. Trifonov, T. Kim, S. Cha, J. H. Sung, S. Cho, W. Shim, M. H. Jo, and H. Choi, Nat. Commun. **9**, 351 (2018).

[131] H. H. Murray, S. P. Kelly, R. R. Chianelli, and C. S. Day, Inorg. Chem. **33**, 4418 (1994).

[132] Y. Feng, W. Zhou, Y. Wang, J. Zhou, E. Liu, Y. Fu, Z. Ni, X. Wu, H. Yuan, F. Miao, B. Wang, X. Wan, and D. Xing, Phys. Rev. B **92**, 054110 (2015).

[133] M. Z. Bellus, M. Li, S. D. Lane, F. Ceballos, Q. Cui, X. C. Zeng, and H. Zhao, Nanoscale Horizons **2**, 31 (2017).

[134] S. P. Kelty, A. F. Ruppert, R. R. Chianelli, J. Ren, and M. H. Whangbo, J. Am. Chem. Soc. **116**, 7857 (1994).

[135] H. X. Zhong, S. Gao, J. J. Shi, and L. Yang, Phys. Rev. B **92**, 115438 (2015).

[136] E. Liu, Y. Fu, Y. Wang, Y. Feng, H. Liu, X. Wan, W. Zhou, B. Wang, L. Shao, C. H. Ho, Y. S. Huang, Z. Cao, L. Wang, A. Li, J. Zeng, F. Song, X. Wang, Y.

Shi, H. Yuan, H. Y. Hwang, Y. Cui, F. Miao, and D. Xing, Nat. Commun. **6**, 6991 (2015).

[137] C. H. Liang, Y. H. Chan, K. K. Tiong, Y. S. Huang, Y. M. Chen, D. O. Dumcenco, and C. H. Ho, J. Alloys Compd. **480**, 94 (2009).

[138] D. A. Chenet, O. B. Aslan, P. Y. Huang, C. Fan, A. M. Van Der Zande, T. F. Heinz, and J. C. Hone, Nano Lett. **15**, 5667 (2015).

[139] Y. C. Lin, H. P. Komsa, C. H. Yeh, T. Björkman, Z. Y. Liang, C. H. Ho, Y. S. Huang, P. W. Chiu, A. V. Krasheninnikov, and K. Suenaga, ACS Nano **9**, 11249 (2015).

[140] C. M. Corbet, C. McClellan, A. Rai, S. S. Sonde, E. Tutuc, and S. K. Banerjee, ACS Nano **9**, 363 (2015).

[141] E. Zhang, Y. Jin, X. Yuan, W. Wang, C. Zhang, L. Tang, S. Liu, P. Zhou, W. Hu, and F. Xiu, Adv. Funct. Mater. **25**, 4076 (2015).

[142] S. Konabe and S. Okada, Phys. Rev. B **90**, 155304 (2014).

[143] V. I. Klimov, A. A. Mikhailovsky, S. Xu, A. Malko, J. A. Hollingsworth, C. A. Leatherdale, H. J. Eisler, and M. G. Bawendi, Science **290**, 314 (2000).

[144] Y. Z. Ma, L. Valkunas, S. L. Dexheimer, S. M. Bachilo, and G. R. Fleming, Phys. Rev. Lett. **94**, 157402 (2005).

[145] S. Mouri, Y. Miyauchi, M. Toh, W. Zhao, G. Eda, and K. Matsuda, Phys. Rev. B **90**, 155449 (2014).

[146] D. Tan, H. E. Lim, F. Wang, N. B. Mohamed, S. Mouri, W. Zhang, Y. Miyauchi, M. Ohfuchi, and K. Matsuda, Nano Res. **10**, 546 (2017).

[147] Z. Tian, C. Guo, M. Zhao, R. Li, and J. Xue, ACS Nano **11**, 2219 (2017).

[148] S. Yang, C. Hu, M. Wu, W. Shen, S. Tongay, K. Wu, B. Wei, Z. Sun, C. Jiang, L. Huang, and Z. Wang, ACS Nano **12**, 8798 (2018).

[149] J. Qiao, X. Kong, Z. X. Hu, F. Yang, and W. Ji, Nat. Commun. **5**, 4475 (2014).

[150] C. Chen, X. Chen, Y. Shao, B. Deng, Q. Guo, C. Ma, and F. Xia, ACS Photonics **5**, 3814 (2018).

[151] X. Lv, W. Wei, Q. Sun, F. Li, B. Huang, and Y. Dai, Appl. Catal. B Environ. **217**, 275 (2017).

[152] Y. Hu, S. Zhang, S. Sun, M. Xie, B. Cai, and H. Zeng, Appl. Phys. Lett. **107**, 122107 (2015).

[153] D. Tan, X. Wang, W. Zhang, H. E. Lim, K. Shinokita, Y. Miyauchi, M. Maruyama, S. Okada, and K. Matsuda, Small **14**, 1704559 (2018).

[154] D. Tan, W. Zhang, X. Wang, S. Koirala, Y. Miyauchi, and K. Matsuda, Nanoscale **9**, 12425 (2017).

[155] D. J. Xue, J. Tan, J. S. Hu, W. Hu, Y. G. Guo, and L. J. Wan, Adv. Mater. **24**, 4528 (2012).

[156] X. Wang, K. Shinokita, H. E. Lim, N. B. Mohamed, Y. Miyauchi, N. T. Cuong, S. Okada, and K. Matsuda, Adv. Funct. Mater. **29**, 1806169 (2019).

[157] D. A. Chenet, O. B. Aslan, P. Y. Huang, C. Fan, A. M. Van Der Zande, T. F. Heinz, and J. C. Hone, Nano Lett. **15**, 5667 (2015).

[158] O. B. Aslan, D. A. Chenet, A. M. Van Der Zande, J. C. Hone, and T. F. Heinz, ACS Photonics **3**, 96 (2016).

[159] J. Shim, A. Oh, D. H. Kang, S. Oh, S. K. Jang, J. Jeon, M. H. Jeon, M. Kim, C. Choi, J. Lee, S. Lee, G. Y. Yeom, Y. J. Song, and J. H. Park, Adv. Mater. **28**, 6985 (2016).

[160] J. Xu, L. Chen, Y. W. Dai, Q. Cao, Q. Q. Sun, S. J. Ding, H. Zhu, and D. W. Zhang, Sci. Adv. **3**, e1602246 (2017).

[161] E. Zhang, Y. Jin, X. Yuan, W. Wang, C. Zhang, L. Tang, S. Liu, P. Zhou, W. Hu, and F. Xiu, Adv. Funct. Mater. **25**, 4076 (2015).

[162] E. Liu, M. Long, J. Zeng, W. Luo, Y. Wang, Y. Pan, W. Zhou, B. Wang, W. Hu, Z. Ni, Y. You, X. Zhang, S. Qin, Y. Shi, K. Watanabe, T. Taniguchi, H. Yuan, H. Y. Hwang, Y. Cui, F. Miao, and D. Xing, Adv. Funct. Mater. **26**, 1938 (2016).

[163] R. Matsunaga, K. Matsuda, and Y. Kanemitsu, Phys. Rev. Lett. **106**, 037404 (2011).

[164] M. Palummo, M. Bernardi, and J. C. Grossman, Nano Lett. **15**, 2794 (2015).

[165] K. He, N. Kumar, L. Zhao, Z. Wang, K. F. Mak, H. Zhao, and J. Shan, Phys. Rev. Lett. **113**, 026803 (2014).

[166] A. Chernikov, T. C. Berkelbach, H. M. Hill, A. Rigosi, Y. Li, O. B. Aslan, D. R. Reichman, M. S. Hybertsen, and T. F. Heinz, Phys. Rev. Lett. **113**, 076802 (2014).

[167] Z. Li, T. Wang, Z. Lu, C. Jin, Y. Chen, Y. Meng, Z. Lian, T. Taniguchi, K. Watanabe, S. Zhang, D. Smirnov, and S. F. Shi, Nat. Commun. **9**, 3719 (2018).

[168] K. Wang, K. De Greve, L. A. Jauregui, A. Sushko, A. High, Y. Zhou, G. Scuri, T. Taniguchi, K. Watanabe, M. D. Lukin, H. Park, and P. Kim, Nat. Nanotechnol. **13**, 128 (2018).

[169] B. Zhu, X. Chen, and X. Cui, Sci. Rep. **5**, 9218 (2015).

[170] A. Singh, G. Moody, S. Wu, Y. Wu, N. J. Ghimire, J. Yan, D. G. Mandrus, X. Xu, and X. Li, Phys. Rev. Lett. **112**, 216804 (2014).

[171] A. Srivastava, M. Sidler, A. V. Allain, D. S. Lembke, A. Kis, and A. Imamoğlu, Nat. Phys. **11**, 141 (2015).

[172] M. Szyniszewski, E. Mostaani, N. D. Drummond, and V. I. Fal'Ko, Phys. Rev. B **95**, 081301 (2017).

[173] C. Zhang, H. Wang, W. Chan, C. Manolatou, and F. Rana, Phys. Rev. B **89**, 205436 (2014).

[174] A. M. Jones, H. Yu, N. J. Ghimire, S. Wu, G. Aivazian, J. S. Ross, B. Zhao, J. Yan, D. G. Mandrus, D. Xiao, W. Yao, and X. Xu, Nat. Nanotechnol. **8**, 634 (2013).

[175] J. S. Ross, S. Wu, H. Yu, N. J. Ghimire, A. M. Jones, G. Aivazian, J. Yan, D. G. Mandrus, D. Xiao, W. Yao, and X. Xu, Nat. Commun. **4**, 1474 (2013).

[176] K. F. Mak, K. He, C. Lee, G. H. Lee, J. Hone, T. F. Heinz, and J. Shan, Nat. Mater. **12**, 207 (2013).

[177] X. F. Qiao, J. Bin Wu, L. Zhou, J. Qiao, W. Shi, T. Chen, X. Zhang, J. Zhang, W. Ji, and P. H. Tan, Nanoscale **8**, 8324 (2016).

[178] C. H. Ho and Z. Z. Liu, Nano Energy **56**, 641 (2019).

[179] J. Huang, T. B. Hoang, and M. H. Mikkelsen, Sci. Rep. **6**, 22414 (2016).

[180] T. Yan, X. Qiao, X. Liu, P. Tan, and X. Zhang, Appl. Phys. Lett. **105**, 101901 (2014).

[181] S. Koirala, S. Mouri, Y. Miyauchi, and K. Matsuda, Phys. Rev. B **93**, 075411 (2016).

[182] N. M. Ravindra and V. K. Srivastava, J. Phys. Chem. Solids **40**, 791 (1979).

[183] S.-H. Chang, S. K. Gray, and G. C. Schatz, Opt. Express **13**, 3150 (2005).

[184] S. Xu, Z. Wu, H. Lu, Y. Han, G. Long, X. Chen, T. Han, W. Ye, Y. Wu, J. Lin, J. Shen, Y. Cai, Y. He, F. Zhang, R. Lortz, C. Cheng, and N. Wang, 2D Mater. **3**, 021007 (2016).

[185] M. Selig, G. Berghäuser, A. Raja, P. Nagler, C. Schüller, T. F. Heinz, T. Korn, A. Chernikov, E. Malic, and A. Knorr, Nat. Commun. **7**, 13279 (2016).

[186] G. Moody, C. Kavir Dass, K. Hao, C. H. Chen, L. J. Li, A. Singh, K. Tran, G. Clark, X. Xu, G. Berghäuser, E. Malic, A. Knorr, and X. Li, Nat. Commun. **6**, 8315 (2015).

[187] S. Sim, H. S. Shin, D. Lee, J. Lee, M. Cha, K. Lee, and H. Choi, Phys. Rev. B **103**, 014309 (2021).

[188] H. Wang, C. Zhang, W. Chan, C. Manolatou, S. Tiwari, and F. Rana, Phys. Rev. B **93**, 045407 (2016).

[189] A. Singh, G. Moody, K. Tran, M. E. Scott, V. Overbeck, G. Berghäuser, J. Schaibley, E. J. Seifert, D. Pleskot, N. M. Gabor, J. Yan, D. G. Mandrus, M. Richter, E. Malic, X. Xu, and X. Li, Phys. Rev. B **93**, 041401 (2016).

[190] C. Robert, D. Lagarde, F. Cadiz, G. Wang, B. Lassagne, T. Amand, A. Balocchi, P. Renucci, S. Tongay, B. Urbaszek, and X. Marie, Phys. Rev. B **93**, 205423 (2016).

[191] D. Van Tuan, A. M. Jones, M. Yang, X. Xu, and H. Dery, Phys. Rev. Lett. **122**, 217401 (2019).

[192] J. W. Christopher, B. B. Goldberg, and A. K. Swan, Sci. Rep. **7**, 140662 (2017).

[193] F. Volmer, S. Pissinger, M. Ersfeld, S. Kuhlen, C. Stampfer, and B. Beschoten, Phys. Rev. B **95**, 235408 (2017).

[194] L. C. Gomes, A. Carvalho, and A. H. Castro Neto, Phys. Rev. B **92**, 214103 (2015).

[195] L. Makinistian and E. A. Albanesi, Phys. Rev. B **74**, 045206 (2006).

[196] T. Deilmann and K. S. Thygesen, Nano Lett. **18**, 1460 (2018).

[197] T. Nishihara, Y. Yamada, M. Okano, and Y. Kanemitsu, Appl. Phys. Lett. **103**, 23101 (2013).

[198] H. Zhong, Z. Zhang, H. Xu, C. Qiu, and L. M. Peng, AIP Adv. **5**, 57136 (2015).

[199] K. F. Mak, K. He, C. Lee, G. H. Lee, J. Hone, T. F. Heinz, and J. Shan, Nat. Mater. **12**, 207 (2013).

[200] N. R. Pradhan, C. Garcia, B. Isenberg, D. Rhodes, S. Feng, S. Memaran, Y. Xin, A. McCreary, A. R. H. Walker, A. Raeliarijaona, H. Terrones, M. Terrones, S. McGill, and L. Balicas, Sci. Rep. **8**, 12745 (2018).

[201] G. D. Shepard, J. V. Ardelean, O. A. Ajayi, D. Rhodes, X. Zhu, J. C. Hone, and S. Strauf, ACS Nano **11**, 11550 (2017).

[202] P. Dey, J. Paul, Z. Wang, C. E. Stevens, C. Liu, A. H. Romero, J. Shan, D. J. Hilton, and D. Karaiskaj, Phys. Rev. Lett. **116**, 127402 (2016).

[203] N. B. Mohamed, K. Shinokita, X. Wang, H. E. Lim, D. Tan, Y. Miyauchi, and K. Matsuda, Appl. Phys. Lett. **113**, 121112 (2018).

[204] J. Pei, J. Yang, R. Xu, Y.-H. Zeng, Y. W. Myint, S. Zhang, J.-C. Zheng, Q. Qin, X. Wang, W. Jiang, and Y. Lu, Small **11**, 6384 (2015).

[205] R. Xu, S. Zhang, F. Wang, J. Yang, Z. Wang, J. Pei, Y. W. Myint, B. Xing, Z. Yu, L. Fu, Q. Qin, and Y. Lu, ACS Nano **10**, 2046 (2016).

[206] T. F. Rønnow, T. G. Pedersen, B. Partoens, and K. K. Berthelsen, Phys. Rev. B **84**, 035316 (2011).

[207] J. Jadczak, J. Kutrowska-Girzycka, T. Smoleński, P. Kossacki, Y. S. Huang, and L. Bryja, Sci. Rep. **9**, 1578 (2019).

[208] S. Kallatt, S. Das, S. Chatterjee, and K. Majumdar, Npj 2D Mater. Appl. **3**, 15 (2019).

[209] S. Das, S. Kallatt, N. Abraham, and K. Majumdar, Phys. Rev. B **101**, 081413 (2020).

Scientific Contributions

The name of the author is bold and underlined.

Peer-Reviewed Articles

1. **Xiaofan Wang**, Keisuke Shinokita, and Kazunari Matsuda, "Radiative lifetime and dynamics of trions in few-layered ReS_2", *Applied Physics Letters*, **2021**, 119, 113103.
2. **Xiaofan Wang,** Keisuke Shinokita, Yuhei Miyauchi, Nguyen Thanh Cuong, Susumu Okada, and Kazunari Matsuda, "Experimental evidence of anisotropic and stable charged excitons (trions) in atomically thin 2D ReS_2", *Advanced Functional Materials* **2019**, 29, 1905961.
3. **Xiaofan Wang**, Keisuke Shinokita, Hong En Lim, Nur Baizura Mohamed, Yuhei Miyauchi, Nguyen Thanh Cuong, Susumu Okada, and Kazunari Matsuda, "Direct and indirect exciton dynamics in few-layered ReS_2 revealed by photoluminescence and pump-probe spectroscopy", *Advanced Functional Materials* **2019**, 29, 1806169.
4. Keisuke Shinokita, **Xiaofan Wang**, Yuhei Miyauchi, Kenji Watanabe, Takashi Taniguchi, and Kazunari Matsuda, "Continuous control and enhancement of excitonic valley polarization in monolayer WSe_2 by electrostatic doping", *Advanced Functional Materials* **2019**, 29, 1900260.
5. Keisuke Shinokita, **Xiaofan Wang**, Yuhei Miyauchi, Kenji Watanabe, Takashi Taniguchi, Satoru Konabe, and Kazunari Matsuda, "Phonon-mediated intervalley relaxation of positive trions in monolayer WSe_2", *Physical Review B* **2019**, 100, 161304(R).

6. Keisuke Shinokita, **Xiaofan Wang**, Yuhei Miyauchi, Kenji Watanabe, Takashi Taniguchi, Satoru Konabe, and Kazunari Matsuda, "Ultrafast dynamics of bright and dark positive trions for valley polarization in monolayer WSe_2", *Physical Review B* **2019**, 99, 245307.
7. Fengjiu Yang, Jiewei Liu, **Xiaofan Wang**, Kenya Tanaka, Keisuke Shinokita, Yuhei Miyauchi, Atsushi Wakamiya, and Kazunari Matsuda, "Planar perovskite solar cells with high efficiency and fill factor obtained using two-step growth process", *ACS Applied Materials & Interfaces* **2019**, 11, 15680.
8. Dezhi Tan, **Xiaofan Wang**, Wenjin Zhang, Hong En Lim, Keisuke Shinokita, Yuhei Miyauchi, Mina Maruyama, Susumu Okada, and Kazunari Matsuda, "Carrier transport and photoresponse in GeSe/MoS_2 heterojunction p–n diodes", *Small* **2018**, 14, 1704559.
9. Nur Baizura Mohamed, Keisuke Shinokita, **Xiaofan Wang**, Hong En Lim, Dezhi Tan, Yuhei Miyauchi, and Kazunari Matsuda, "Photoluminescence quantum yields for atomically thin-layered ReS_2: Identification of indirect-bandgap semiconductors", *Applied Physics Letters* **2018**, 113, 121112
10. Takao Yamaoka, Hong En Lim, Sandhaya Koirala, **Xiaofan Wang**, Keisuke Shinokita, Mina Maruyama, Susumu Okada, Yuhei Miyauchi, and Kazunari Matsuda, "Efficient photocarrier transfer and effective photoluminescence enhancement in Type I monolayer $MoTe_2$/WSe_2 heterostructure", *Advanced Functional Materials* **2018**, 28, 1801021.
11. Dezhi Tan, Wenjin Zhang, **Xiaofan Wang**, Sandhaya Koirala, Yuhei Miyauchi, and Kazunari Matsuda, "Polarization-sensitive and broadband germanium sulfide

photodetectors with excellent high-temperature performance”, *Nanoscale*, **2017**, 9, 12425

Conference Presentations

International Conferences

1. **Xiaofan Wang**, Keisuke Shinokita, Hong En Lim, Nur Baizura Mohamed, Yuhei Miyauchi, and Kazunari Matsuda, "Intra-band and inter-band carrier dynamics in a few layer ReS_2", *19th International Conference on the Science and Application of Nanotubes and Low-dimensional Materials (NT18)*, PC065, Peking University, Beijing, China, 15th – 20th July 2018 (Poster).
2. **Xiaofan Wang**, "Optical properties and carrier dynamics on ReS_2", *The 4th talent recruitment & project matchmaking event for innovation and development*, Henan University, Kaifeng, China, 26th – 27th June 2021 (Oral).

Domestic Conferences

1. **Xiaofan Wang**, Keisuke Shinokita, Yuhei Miyauchi, and Kazunari Matsuda, "Charged exciton (trion) in anisotropic atomically thin 2D material ReS_2", *The 56th Fullerences-Nanotubes-Graphene General Symposium (FNTG)*, 2P-6, University of Tokyo, Ito International Research Center, Tokyo, Japan, 2nd – 4th March 2019 (Poster).
2. **Xiaofan Wang**, Keisuke Shinokita, Hong En Lim, Nur Baizura Mohamed, Yuhei Miyauchi, and Kazunari Matsuda, "Carrier dynamics in ReS_2 3-layer studied by ultrafast spectroscopy", *The 54th Fullerences-Nanotubes-Graphene General*

Symposium (FNTG), University of Tokyo, Ito International Research Center, Tokyo, Japan, 10th – 12th March 2018 (Oral).

3. **Xiaofan Wang**, Wenjin Zhang, Nur Baizura Mohamed, Dezhi Tan, Hong En Lim, Yuhei Miyauchi, and Kazunari Matsuda, "2D materials FETs fabrication by dry-transfer process".*14th optical matter science discussion group,* Biwako Club, Otsu, Shiga, Japan, 16th – 17th July 2017 (Oral).
4. **Xiaofan Wang**, Wenjin Zhang, Nur Baizura Mohamed, Dezhi Tan, Hong En Lim, Yuhei Miyauchi, and Kazunari Matsuda, "Photoluminescence and photocurrent properties of monolayer WSe_2 FETs fabricated by dry-transfer process", *The 52th Fullerences-Nanotubes-Graphene General Symposium (FNTG)*, 2P-33, University of Tokyo, Ito International Research Center, Tokyo, Japan, 1st – 3rd March 2017 (Poster).
5. **Xiaofan Wang**, Wenjin Zhang, Yuhei Miyauchi, and Kazunari Matsuda "Photoluminescence properties of monolayer MoS_2 FETs fabricated by dry-transfer process", *The 51th Fullerences-Nanotubes-Graphene General Symposium (FNTG),* 2P-31, Hokkaido citizens actives center kaderu 2·7, Sapporo, Hokkaido, Japan, 7th – 9th September 2016 (Poster).

Appendix

DFT Calculation of band structure

In order to support the experimentally result of band structure and carrier dynamics, DFT calculation of 3L-ReS$_2$ was conducted. The calculated band structures of 3L-ReS$_2$ include three types of stacking configuration, ABC stacking (Figure S.1(a)), AB stacking (I) (Figure S.1(b)) and AB stacking (II) (Figure S.1(c)). The lowest optical transitions associated with the direct and indirect band gap, are denoted by the red dashed and black dashed lines, respectively. Figure S.1(d) is relative total energy of 3L-ReS$_2$ by DFT calculation. The relative energy is plotted as the energy difference from the ABC stacking. In the AB (I) and (II) stacking, the band structure indicates the indirect gap band structure. In ABC stacking, the calculated results show direct gap band structure. The lower total energy in AB (I) and (II) stacking than that in ABC stacking suggests that the most stable crystal structure in 3L-ReS$_2$, which is also confirmed by Raman scattering spectrum.

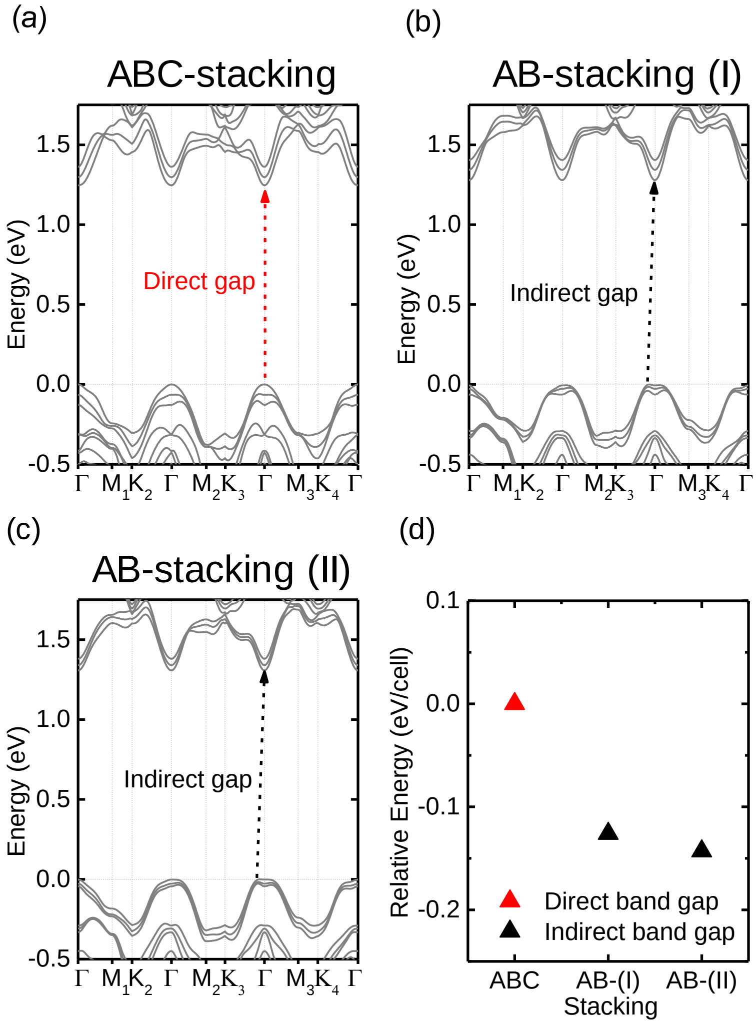

Figure S.1 Calculated band structures of 3L-ReS_2 for (a) ABC stacking, (b) AB stacking (I) and (c) AB stacking (II). The lowest optical transitions associated with the direct and indirect band gap are denoted by the red dashed and black dashed lines, respectively. (d) Relative total energy of 3L-ReS_2 by DFT calculation. The relative energy is plotted as the energy difference from the ABC stacking.

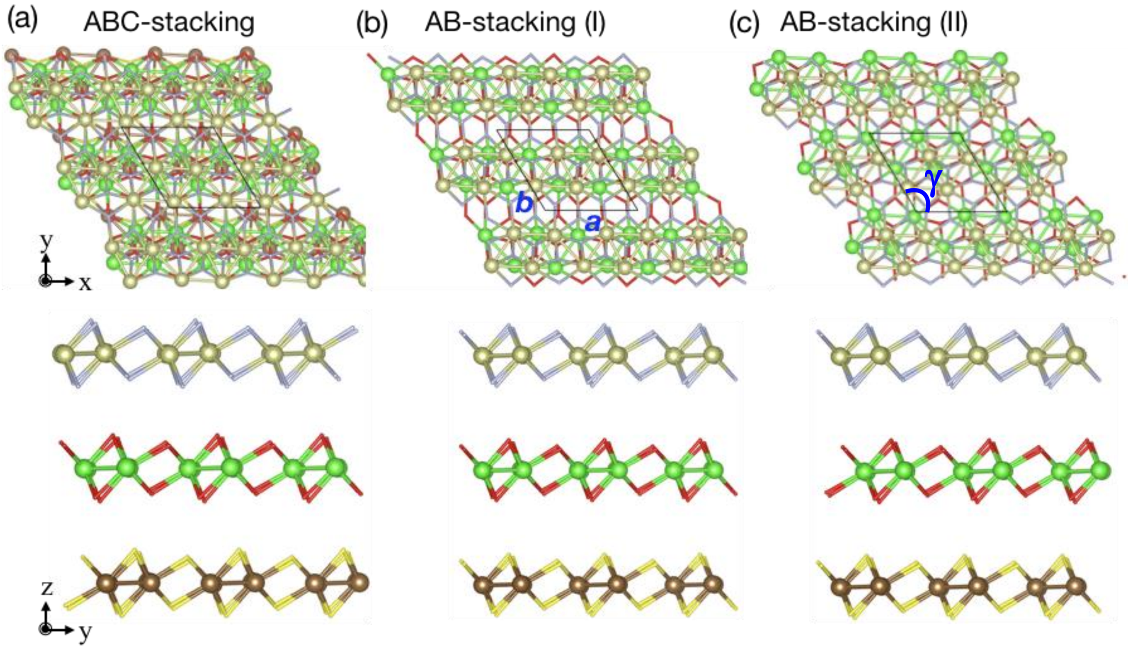

Figure S.2 Top and side views of optimized structures of trilayer (3L) ReS_2 with the experimental lattice parameters a=6.417 Å, b=6.51 Å and γ=121.10° with (a) ABC-stacking, (b) AB-stacking (I), and (c) AB-stacking (II) interlayer arrangements.

The detail of DFT calculation are as follows. All calculations were based as implemented in Quantum ESPRESSO code. The van der Waals corrected (vdw-df2-b86r) density function was used to describe the exchange correlation energy to accurately describe the weak binding between the ReS_2 layers. Projector augmented wave pseudopotentials were used to describe the electron-ion interaction. The valence wave functions and augmented charge density were expanded by a plane-wave basis set with cutoff energies of 70 and 560 Ry, respectively. Brillouin-zone integration was performed under a 16×16×1 uniform *k*-point grid. A repeating sheet model consisting of a 1×1 lateral periodicity of a distorted 1*T* 3L-ReS_2 was used, which was separated by 1.0 nm from its periodic images. The geometric structure of 3L-ReS_2 was optimized under the experimental lattice constants (*a*=6.417 Å, *b*=6.51 Å and γ=121.1°) until the remaining force acting on the atoms was less than 0.0001 Ry/Bohr.